Electromagnetic Simulation of INO-ICAL Magnet and its Sensitivity to Sterile Neutrino Mixing

By

SHIBA PRASAD BEHERA

Enrolment Number: PHYS01201104005

Bhabha Atomic Research Centre, Mumbai

A thesis submitted to the

Board of Studies in Physical Sciences

In partial fulfillment of requirements

For the Degree of

DOCTOR OF PHILOSOPHY

of

HOMI BHABHA NATIONAL INSTITUTE

August, 2016

Homi Bhabha National Institute

Recommendations of the Viva Voce Board

As members of the Viva Voce Board, we certify that we have read the dissertation prepared by **Shiba Prasad Behera** entitled **"Electromagnetic simulation of INO-ICAL magnet and its sensitivity to sterile neutrino mixing"** and recommend that it may be accepted as fulfilling the dissertation requirement for the Degree of Doctor of Philosophy.

________________________ Date: 18/8/2016

Chair - Prof. S. Basu

________________________ Date: 18/8/2016

Guide/Convener - Prof. V. M. Datar

________________________ Date: 18/8/2016

Member 1 - Prof. G. Ravikumar

Gobinda Majumder ________________________ Date: 18/8/2016

Member 2 - Prof. G. Majumdar

Srubabati Goswami ________________________ Date: 18/8/2016

Examiner - Prof. Srubabati Goswami

Final approval and acceptance of this dissertation is contingent upon the candidate's submission of the final copies of the dissertation to HBNI.

I hereby certify that I have read this dissertation prepared under my direction and recommend that it may be accepted as fulfilling the dissertation requirement.

Date: 18/8/2016

Place: Mumbai

Guide: Prof. V. M. Datar

STATEMENT BY AUTHOR

This dissertation has been submitted in partial fulfillment of requirements for an advanced degree at Homi Bhabha National Institute (HBNI) and is deposited in the Library to be made available to borrowers under rules of the HBNI.

Brief quotations from this dissertation are allowable without special permission, provided that accurate acknowledgment of source is made. Requests for permission for extended quotation from or reproduction of this manuscript in whole or in part may be granted by the Competent Authority of HBNI when in his or her judgment the proposed use of the material is in the interests of scholarship. In all other instances, however, permission must be obtained from the author.

Shiba Prasad Behera

DECLARATION

I, hereby declare that the investigation presented in the thesis has been carried out by me. The work is original and has not been submitted earlier as a whole or in part for a degree / diploma at this or any other Institution / University.

Shiba Prasad Behera

Dedicated to my Beloved Mother…

ACKNOWLEDGMENTS

First and foremost, I would like to express my sincere appreciation and gratitude to my guide Prof. V. M. Datar for his guidance during my Ph.D study and research. His constant encouragement and constructive suggestions have been precious for the development of this thesis content. He has provided me a freedom in research and extended his helping hand whenever it is necessary. I am really very proud to get an opportunity to work with him.

Besides my advisor, I would like thank to members of my doctoral committee: Prof. M. S. Bhatia, Prof. G. Ravikumar, Prof. Gobinda Majumdar, Prof. S. Basu, for their support, valuable comments and suggestions during this period. I am extremely grateful to Prof. A. K. Mohanty for the invaluable advices, encouragement and help on doing this work.

My special thanks to Dipak K. Mishra for useful discussion and his support during this period. My sincere thanks also go to Anushree Ghsosh, Sandhya Choubey, Renju Thomas, Pawan K. Netrakanti, B. K. Nayak, S. Uma Sankar, P. C. Rout and S. V. L. S. Rao. The thesis would not have come to a successful completion, without the support I received from them. It is my pleasure to thank E. T. Mirgule for always encouraging me to write the thesis in proper time.

I would like to thank Vibhuti Duggale for her support while running the numerical code at the BARC super-computing facility. She has been very kind and patient and always willing to support me whenever I approached her.

I am also thankful to the INO collaboration.

I would also like to acknowledge Prof. Subhasis Chattopadhyay, S. K. Thakur and Prof. Y. P. Viyogi for their support while carrying out the magnetic measurements at VECC, Kolkata.

This thesis could not be possible without the love and support from my parents. I would like to express my sincere gratitude to them. They are my the greatest source of inspiration and have given me the motivation and encouragement to do my PhD. I thank them from my deep heart. I am thankful to my wife, Sagarika Priyadarshini, for her love, care, support and encouragement. Her patience and sacrifice will remain my inspiration throughout my life. Finally, to my little angel, Dibyanshi for all her love and giving me happiness in each day.

Publications:

Refereed Journals :

1. Simulation Studies for Electromagnetic Design of INO ICAL Magnet and its Response to Muons, **S. P. Behera**, M. S. Bhatia, V. M. Datar and A. K. Mohanty, IEEE Trans. Magn., **51**, 1 (2015).

Communicated :

1. Physics Potential of the ICAL detector at the India-based Neutrino Observatory (INO), The ICAL Collaboration: Shakeel Ahmed, M. Sajjad Athar, Rashid Hasan, Mohammad Salim, S. K. Singh, S. S. R. Inbanathan, Venktesh Singh, V. S. Subrahmanyam, **S. P. Behera** et al., arXiv:1505.07380 (submitted to PRAMANA).

2. Searching for sterile neutrino mixing with the ICAL detector at INO, **S. P. Behera**, Anushree Ghosh, Sandhya Choubey, V. M. Datar, D. K. Mishra, and A. K. Mohanty, arXiv:1605.08607 (submitted to European Physical Journal C).

Conference Proceedings:

1. Search for sterile neutrino mixing using ICAL detector at INO, **S. P. Behera**, A. K. Mohanty, Anushree Ghosh, D. K. Mishra, S. Uma Sankar, and V. M. Datar, Proc. of the Symp. on Nucl. Phys. **59**, 794 (2014).

2. Energy resolution and charge identification efficiency of muons in INO ICAL detector, **S. P. Behera**, A. K. Mohanty, Meghna K. K. and V. M. Datar, Proc. of the Symp. on Nucl. Phys. **58**, 944 (2013).

3. Improvements on the Iron Calorimeter Magnet design for INO, **S. P. Behera**, A. Thirunavukarasu, V. M. Datar, M. S. Bhatia and Y. P. Viyogi; Proc. of the Symp. on Nucl. Phys. **56**, 1048 (2011).

4. On the simulation of the Iron Calorimeter Magnet for INO, **S. P. Behera**, N. Dash, M. S. Bhatia, V. M. Datar and P. Verma, Proc. of the Symp. on Nucl. Phys. **55**, 776 (2010).

List of other publications not related to this thesis

1. Simulation of detector response for antineutrino induced events with a proto-type plastic detector array, **S. P. Behera**, V. Jha, V. K. S. Kashyap, D. K. Mishra, A. Mitra, P. K. Netrakanti and L. M. Pant, Proc. of the DAE-BRNS Symp. on Nucl. Phys. **60**, 1032 (2015).

2. Time distribution measurements of prompt-delay events at the Dhruva reactor for detection of antineutrinos, V. K. S. Kashyap, **S. P. Behera**, A. Bhattacharya, V. Jha, D. K. Mishra, A. Mitra, P. K. Netrakanti, L. M. Pant and A. Saxena, Proc. of the DAE-BRNS Symp. on Nucl. Phys. **60**, 924 (2015).

3. Background measurements at the DHRUVA reactor site for feasibility studies towards antineutrino detection from reactors, V. K. S. Kashyap, **S. P. Behera**, A. Mitra, Abhijit Bhattacharyya, R. G. Thomas, L. M. Pant, P. C. Rout, Suresh Kumar, A. K. Mohanty, and V. M. Datar, Proc. of the Symp. on Nucl. Phys. **59**, 978 (2014).

4. Simulation of detector response for anti-neutrinos and reconstructing their energy spectrum with plastic detector array, **S. P. Behera**, R. G. Thomas, Suresh Kumar, A. Mitra, A. Bhattacharyya, and V. M. Datar, Proc. of the Symp. on Nucl. Phys. **59**, 990 (2014).

5. Measurement of the Damping of the Nuclear Shell Effect in the Doubly Magic ^{208}Pb Region, P. C. Rout, D. R. Chakrabarty, V. M. Datar, Suresh Kumar, E. T. Mirgule, A. Mitra, V. Nanal, **S. P. Behera** and V. Singh, Phys. Rev. Lett. **110**, 062501 (2013).

6. Electromagnetic transition from the 4^+ to 2^+ resonance in ^{8}Be measured via the radiative capture in ^{4}He+^{4}He, V. M. Datar, D. R. Chakrabarty, Suresh Kumar, V. Nanal, S. Pastore, R. B. Wiringa, **S. P. Behera**, A. Chatterjee, D. Jenkins, C. J. Lister, E. T. Mirgule, A. Mitra, R. G. Pillay, K. Ramachandran, O. J. Roberts, P. C. Rout, A. Shrivastava, and P. Sugathan, Phys. Rev. Lett **111**, 062502 (2013).

SYNOPSIS

Neutrinos are the second most abundant particles in the universe. The study of neutrinos has advanced our understanding of fundamental particles and their interactions. It has also made an impact in other fields such as cosmology, astrophysics, nuclear physics and geophysics. In the standard model of particle physics, there are three flavors of neutrinos ν_e, ν_μ, ν_τ and they are massless. The phenomenon of neutrino oscillations has been established experimentally and implies that at least two mass eigenstates have non-zero masses. The extraction of the neutrino mixing parameters has been possible through various experiments carried out using neutrinos from different sources viz: atmospheric, solar, reactor and accelerator. Results from these experiments led to the current three-neutrino mixing paradigm, in which the three active neutrinos ν_e, ν_μ, ν_τ, with definite flavour, are superpositions of three neutrinos ν_1, ν_2, ν_3, with definite masses, m_1, m_2, m_3, respectively. The necessary and sufficient conditions for the existence of neutrino oscillations is that neutrinos have non-zero mixing of at least 2 mass eigenstates and that at least 2 masses are non-zero. This phenomenon cannot be understood within the standard model (SM) of particle physics and is a hint of physics beyond the SM.

In three flavor neutrino oscillation, the oscillation parameters are the three mixing angles, θ_{12}, θ_{23} and θ_{13}, charge parity violating phase, δ_{CP}, and two independent squared mass differences, Δm^2_{21} and Δm^2_{31}. The amplitude of neutrino oscillation probability is decided by the mixing angle while the position of maxima or minima depends on the squared mass difference. The mixing parameters θ_{12} and Δm^2_{21} are precisely determined by the solar neutrino experiments. The KamLAND reactor neutrino experiment while confirming neutrino oscillation provided the most precise value of Δm^2_{21} and improved the precision of θ_{12} in combination with solar neutrino data. The mixing angle θ_{23} has been measured by the Super-Kamiokande collaboration using atmospheric neutrinos and by the long-baseline accelerator experiments such as MINOS and T2K. The latter have also measured $\sin^2\theta_{23}$ with good accuracy. The non-zero value of θ_{13}, hinted by the results of T2K and MINOS, has been accurately measured by the short baseline reactor neutrino experiments DayaBay, RENO and DoubleChooz. As of now the sign of Δm^2_{31} and value of δ_{CP} are unknown. The sign of Δm^2_{31} will help determine the hierarchy of neutrino masses. If CP-violation is observed in the neutrino sector, leptogenesis is a possible means of explaining the observed asymmetry between matter and antimatter.

The anomalies observed, albeit at not very large significance, in several experiments *viz.* LSND, MiniBooNE, SAGE, GALLEX are not explained by 3-ν oscillation theory. The observed appearance probability $\bar{\nu}_\mu \to \bar{\nu}_e$ oscillations in LSND showed an excess of electron anti-neutrino events above the expected background with a 3.8σ significance. The smallness of $\Delta m^2_{sol} \simeq 7.5 \times 10^{-5}$ eV^2 and $\Delta m^2_{atm} \simeq 2.4 \times 10^{-3}$ eV^2 coupled with the large Δm^2 required by LSND, for example, requires a fourth neutrino. The MiniBooNE experiment was motivated by the LSND results and studied $\nu_\mu \to \nu_e$ and $\bar{\nu}_\mu \to \bar{\nu}_e$ oscillations. In the $\nu_\mu \to \nu_e$ study, MiniBooNE found no evidence for an excess of ν_e candidate events above 475 MeV; however, a 3 σ excess of electron like events was observed below 475 MeV. The LSND data is consistent with ν_μ to ν_e oscillations in the $\Delta m^2 \sim 0.1$ to 1.0 eV^2. The experimental results from the LSND, MiniBooNE and $\bar{\nu}_e$ disappearance revealed by the reactor anomaly indicates the necessity of possible short-baseline neutrino experiments. Also radioactive source calibration of the Gallium solar neutrino experiments SAGE and GALLEX showed an event rate which is somewhat lower than expected. This effect can be explained by the hypothesis of ν_e disappearance due to oscillations with $\Delta m^2 \geq 1$ eV^2 ("Gallium anomaly"). Their results cannot be explained within the standard three active neutrino oscillation formalism and suggest the existence of additional neutrinos with masses at the eV scale. Such neutrinos may not participate in the weak interaction due to the constraint on the invisible width of the Z boson and are therefore called "sterile" neutrinos.The existence of sterile neutrinos which have been thermalized in the early Universe is compatible with Big-Bang Nucleosynthesis data. The combined analysis of data from CMB+lensing+BAO(baryon acoustic oscillation) experiments provide a robust frequentist upper limit $\sum m_\nu \leq 0.26$ eV with 95 % CL. There is no preferred theoretical model or framework that has emerged so far from the above mentioned experimental results. There have been several attempts to interpret these anomalies in terms of 3 + N neutrino oscillation models involving 3 active neutrinos and N additional sterile neutrinos. The possible existence of sterile neutrinos is very interesting because they are new particles which could give us valuable information on the physics beyond the standard model. The down-going atmospheric ν_μ and $\bar{\nu}_\mu$ fluxes can be significantly altered due to the presence of eV^2-scale active-sterile oscillations. A large magnetized iron detector like the proposed iron calorimeter (ICAL) at the India-based Neutrino Observatory (INO) may be used to study these oscillations.

Roughly one half of work reported here is on the design of the ICAL magnet, its response to muons for various strengths of magnetic field and its sensitivity to sterile neutrino mixing. The proposed ICAL detector will measure precisely the oscillation parameters using atmospheric neutrinos. In particular, it aims at identifying the neutrino mass hierarchy, normal or inverted. To reduce the cosmic rays background, the detector will be placed under the mountain with an all round rock cover of at least 1 km. The rectangular shaped 51 kton magnetized ICAL detector, will also provide the target nuclei of iron for neutrino interactions to facilitate their detection via the charged particles produced in these interactions. The ICAL detector consists of three modules each weighing $\sim$ 17 kton with dimensions of 16 m $\times$ 16 m $\times$ 14.5 m and 151 layers of low carbon steel. The layers are alternated with gaps of 40 mm in which will be placed placed active gas detectors, of the Resistive Plate Chambers (RPC) type, to measure the charged particles produced due to charged current (CC) and neutral current interaction of ν_μ and $\bar{\nu}_\mu$ respectively with the nucleons of iron. The RPC detectors give the position and time information. The mutually perpendicular readout strips in each RPC provide X, Y-position information and the layer number gives Z-position information. The main advantage of the magnetized ICAL detector is to identify, separately, ν_μ and $\bar{\nu}_\mu$ induced events. The calorimeter will be magnetized with a piecewise uniform magnetic field (B = 1-1.5 T) to distinguish the μ^- and μ^+ events from the opposite curvature of their tracks in the presence of a magnetic field.

In order to measure the oscillation parameters more precisely, it is important that the energy and incoming direction of the detected neutrino have to be determined with very good accuracy. In case of atmospheric neutrinos, the source to detector distance is estimated using their incoming zenith angle. The neutrinos (anti-neutrinos) interact with nucleons of iron in the detector through quasi-elastic, resonance and deep inelastic scattering processes. In a CC muon neutrino interaction, a muon is produced along with hadrons. The muon gives a clear track inside the detector. On the other hand, a strongly interacting hadron produces a hadronic shower in the detector. The hit multiplicity of charged particles distinct from the muon track are used to estimate the total energy of hadrons in an event. The muon momentum can be measured either from the track length of stopped muons in the detector or from the curvature of the track due to the magnetic field. The magnetic field helps not only in the momentum measurement of muons that do not stop in ICAL but also increases the fiducial volume of the detector. In a magnetized detector, the muon momentum resolution, at the highest energy, depends upon the strength and uniformity of magnetic field.

The electromagnetic simulation of the ICAL magnet was done for various configurations to optimize the design of ICAL detector. These simulations were carried out using a finite element method based 3-D commercial software. In the simulation, we have defined the geometry and assigned the magnetic properties (B-H-properties, where B is the magnetic induction and H is the magnetic field) of the iron plates. The B-H profile of the soft iron was obtained from the measurement of toroidal samples using a BH-loop tracer. The motivation of the simulation was to find the optimal slot configuration (through which pass the copper coils, for energizing ICAL), tiling of plates and to study the magnetic field strength, and its uniformity for the baseline design and the effect of various kinds of departure from this design. The computation time to simulate the ICAL magnet having 151 layers of iron plate is very large, therefore most of the studies were carried out considering a single layer of iron plate. This result matches, within 4 %, that for the configuration which consists of three iron layers at the bottom, middle and top, respectively, carrying four coils, each having height of 15 m.

It may be observed that the configuration with continuous slots for accommodating the coils, gives a superior B-field uniformity compared with those with two or four pairs of discrete slots. It was found that, the fractional area for which $|B| \geq 1$ T is $\sim$ 75 % at 20 kA turns and increased to $\sim$ 90 % at 60 kA-turns. The study shows that for the case of the plates with continuous slots, the B-field distribution can be optimized by choosing proper slots dimension and their position. The iron plate with larger slot length than the standard baseline design gives marginally better B-field distribution. The B-field distribution in iron increases with increase of plate thickness and gets saturated beyond the plate thickness $\sim$4 cm justifying the choice of 5.6 cm. It was also found that the B-field distribution depends on the soft magnetic properties of the material in which carbon content is crucial.

Practically, however, building the ICAL detector using 16 m $\times$ 16 m $\times$ 0.056 m size plate is not feasible due to difficulties in manufacturing and handling. Therefore, the 16 m $\times$ 16 m area will be tiled with plates of size 2 m $\times$ 4 m. Due to mechanical tolerances, there are air gaps among tiles. The magnetic lines of forces fringe out at air gaps, which lead to the reduction of flux linkage amongst them. The electromagnetic simulation was carried out considering tile gaps of 2 mm, 4 mm and 6 mm. It shows that the B-field in iron reduces with increase of air gaps among tiles. A study of 4 possible different tile configurations was also carried out, with a nominal 2 mm gap between plates, to get the maximum B-field at minimum ampere-turns. Two configurations, C2 and C3, appear to give better results at lowest power dissipation in coils. As expected, it was found that an increase of air gap between adjacent tiles leads to a reduction of B-field for a given excitation current. Although the smallest gap is desirable, a gap of 2 mm may be a practical compromise. There are magneto-static forces among tiles which try to reduce the air gaps. The estimated magneto-static force among tiles is $\sim$ 100 kN which needs to be taken into account while designing the mechanical structure and for assessing the stability of the ICAL magnet.

The measurement of neutrino oscillation parameters using a magnetized ICAL detector depends on the reconstructed muon energy and angular resolution. It is also important to identify the neutrinos by discriminating the corresponding produced leptons. For this purpose, a Monte Carlo (MC) simulation using the object oriented simulation toolkit GEANT4 at various strength of B-fields was done to estimate these parameters. The magnetic field map in a grid size of 5 cm $\times$ 5 cm of the iron plate obtained from the electromagnetic simulation of ICAL magnet was interpolated for the 16 m $\times$ 16 m area and used for muon tracking. A sample of 10^4 muons (μ^-) with fixed energies 1-20 GeV, originate in the central region of the detector where the B-field is nearly uniform, in all azimuthal directions and at fixed zenith angles (θ_z) such that cos θ_z takes on values between 0.1 to 1.0 in bins of Δcos θ_z = 0.1. The strengths of magnetic field chosen for this study are 1.1 T, 1.5 T and 1.8 T. At a given magnetic field strength, the energy resolution improves with increasing muon energy. The lowest energy resolution obtained is $\sim$ 10 % for 5 GeV muons incident at cos θ_z = 0.95 for a magnetic field strength of 1.5 T. It is observed that, the charge identification efficiency is more than 90 % for all energies for a magnetic field greater than 1.5 T. A similar behaviour has been observed for the energy resolution and charge identification efficiency for a range of values of cos θ_z between 0.85 and 0.15. It is concluded that the energy resolution as well as charge identification efficiency of muons improve with increase of the magnetic field strength, but a choice of 1.5 T B-field appears to give satisfactory results and there was not much gain by increasing the field to 1.8 T. The angular resolution of ICAL detector is less than 1° for energy greater than about 4 GeV. The study shows that the behavior of angular resolution with magnetic field is almost independent of its strength. The response of ICAL to muons is used to study its sterile neutrino mixing sensitivity.

The second part of the thesis is based on a study of the sensitivity of ICAL to sterile neutrino mixing. From among the various models that could be used for studying the sterile neutrino sensitivity, the present analysis used the “3 + 1” model where ‘3’ and ‘1’ stand for active and sterile neutrinos, respectively. The MC simulation code used was developed for the physics analysis of ICAL at INO. The code NUANCE, duly modified for INO, has been developed by the collaboration, and used as a MC generator for generating atmospheric neutrino events and HONDA atmospheric neutrino flux is given as input to the generator. In order to reduce the MC fluctuations in the event sample, events were generated corresponding to 50 $\times$ 1000 kton-years exposure. Since, it takes a fairly long time to run the Nuance code to generate such a large event sample, running it over and over again for each set of oscillation parameters is practically impossible. Therefore events are first generated without imposing the neutrino oscillation. Thereafter, the reweighting algorithm is imposed to generate the event sample for any set of oscillation parameters. Finally the events are folded with detector efficiencies and resolution, calculated by the INO collaboration, to get the reconstructed muon events in ICAL. The events are finally normalized to a realistic number of years for running the ICAL. The ICAL physics simulations are performed not in terms of the neutrino energy and angle, but using muon and hadron information of an event. Then, χ^2 was calculated considering the no-sterile and sterile oscillated events taking into account both statistical and systematic errors. The variable bins used took into consideration the detector resolution in the energy range 1-20 GeV and zenith angles for downward-going as well as upward-going neutrinos such that the bin content should be $\geq$1.

The analysis was carried out separately considering neutrino events which reach the detector (a) only in the downward-going (zenith angle θ_z: $0° \leq \theta_z \leq 90°$) direction and (b) coming from all directions ($0° \leq \theta_z \leq 180°$). The details of the neutrino induced events used for the analysis are muon energy, its zenith angle and the hadron energy. In one part of the study, the sterile neutrino sensitivity is carried out considering the reconstructed energy and zenith angle of the muon. In another case, the muon energy and zenith angle combined with hadron energy are considered. It was concluded, that the downward-going atmospheric neutrinos will show the signatures of eV^2- scale oscillation due to their variable energy and path length. The upper limit for $\sin^2 2\theta_{\mu\mu}$ is $\sim$ 0.16 considering combined muon and hadron information from neutrino induced events at an exposure of 1 Mt.yr. The sensitivity to the sterile neutrino mixing angle further improves by considering neutrinos coming from all directions and reaching the detector. There was about 35 % enhancement in sensitivity over all Δm^2_{41}. A comparative study was carried out between the results from SciBooNE/ MiniBooNE with ICAL at INO using neutrino and muon events. It was found that, at lower values of Δm^2_{41}, the ICAL detector has better sensitivity compared to the short baseline experiments like SciBooNE and MiniBooNE. Further, exclusion plots have been generated for various mixing angle combinations considering only muon energies and zenith angles. To estimate the χ^2 with the simulated data, the best fit values for $\theta_{14} = \theta_{24} = \theta_{34} = 10°$ and at $\Delta m^2_{41} = 1$ eV^2 were considered. While generating the exclusion plots for two mixing angles, the third mixing angle and Δm^2_{41} have been marginalized and also the corresponding priors were added. It showed that the upper limit for the mixing angles θ_{14}, θ_{24} and θ_{34} were about 20° - 30° at 90 % confidence level. As a final remark it may be mentioned that, the confirmation of the existence of sterile neutrinos is a great challenge for upcoming neutrino physics experiments.

Contents

List of Figures

List of Tables

Chapter 1

Introduction

One of the aims of particle physics is to explore the smallest building blocks of matter and the fundamental forces between them. The matter around us is made out of elementary spin-half particles called quarks and leptons. There are six quarks and six leptons with each having their corresponding antiparticles. According to the standard model (SM) of particle physics, they interact with each other through three fundamental interactions: strong, electromagnetic and weak. The fourth fundamental interaction, gravitational, is not part of the SM. Efforts to unify all four interactions include string theory. The list of standard model particles and the mediator exchanged in their interaction is shown in Fig. 1.1. The particles are characterized by their mass, spin which decides nature of the particles, fermions (half-integral spin) or bosons (integral spin), and charges which determines their interactions. In the SM, these particles are grouped into three generations depending upon their masses and stability: the lightest and most stable particles make up the first generation, whereas the heavier and less stable particles belong to the second and third generations. In addition, quarks also come in three different "colours" *viz.* red color, green color, blue color and they combine so as to form colourless objects. The six leptons are similarly classified in three generations:

$$\begin{pmatrix} e \\ \nu_e \end{pmatrix}, \begin{pmatrix} \mu \\ \nu_\mu \end{pmatrix}, \begin{pmatrix} \tau \\ \nu_\tau \end{pmatrix}.$$

The leptons e, μ and τ all have an electric charge and also a sizable mass. On the other hand, the elusive spin 1/2 neutrinos are massless and chargeless entities in the SM of particle physics. In contrast to the usual way of discovering new particles through experiments, the concept of neutrino first came from the theory. In 1930, Wolfgang Pauli proposed the existence of a neutral particle that is emitted along with the electron in beta decay in order to conserve energy, momentum, angular momentum and spin-statistics. In 1933, Enrico Fermi introduced the name neutrino which is the Italian equivalent of “little neutral one”. The energy spectrum of β particles from the radioactive nuclei had been known to be continuous and was explained by Enrico Fermi. The electrically neutral neutrino interacts weakly with matter through the exchange of a $W^{\pm}$ and Z^{0} boson in charged current (CC) and neutral current (NC) interactions, respectively. In the more likely CC quasi-elastic

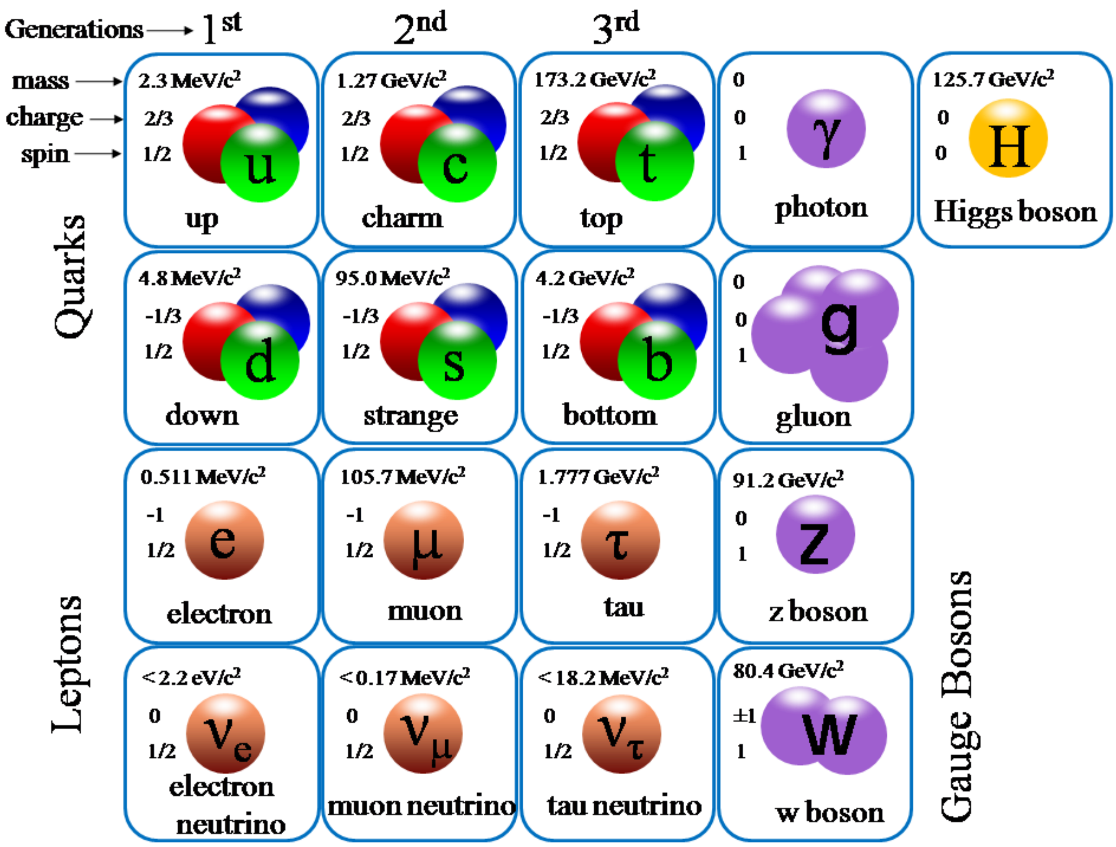

Figure 1.1: Periodic table of the Standard Model particles.

(CCQE)[1] neutrino interaction (as compared to the NC interaction) a (anti-) neutrino interacts with a (proton) neutron and produces the corresponding charged (anti-) lepton and a (neutron) proton:

$$\begin{aligned} \nu_l + n &\rightarrow l^- + p \; (W^+) \\ \bar{\nu}_l + p &\rightarrow l^+ + n \; (W^-) \, . \end{aligned} \tag{1.1}$$

[1]It is a process characterized by the energy transfers to the target particles being small compared to the incident energy of the scattered particles.

In 1934, Hans Bethe and Rudolf Peierls first estimated the neutrino interaction cross-section to be less than 10^{-44} cm^2 [1] which made it "impossible" to detect. The interaction is so small that the earth is transparent to neutrinos. It requires an intense source and/or a very massive sensitive detector for detecting neutrinos. A neutrino can not be detected directly unless it is absorbed by a nucleon and produces a charged lepton or scatters off an electron or hadron. In both cases, the reaction products may be observed through their electromagnetic interaction. The idea of direct neutrino detection based on the radiochemical method was first given by B. Pontecorvo. In 1956 Reines and Cowan reported the first detection of (electron anti-) neutrinos [2] produced in a nuclear reactor. In 1962, muon neutrinos were discovered by L. Lederman, M. Schwartz, J. Steinberger and colleagues at Brookhaven National Laboratory (BNL) and confirmed that they were different from electron neutrinos [3]. In 2001, the DONUT (Direct Observation of NU Tau) [4] experiment at the Fermi National Accelerator Laboratory (FNAL) observed the third neutrino flavour ν_τ. In addition to the neutrino discoveries, there were various experiments which measured the neutrino properties *viz.* helicity, absolute mass, charge, magnetic moment. The measurement of the neutrino (ν_e) helicity was carried out by Goldhaber *et al.* [5] and found to be left handed. An absolute mass measurement of ν_e was carried out using the β-decay radioactive source tritium (^{3}H) by the Troitsk collaboration [6] and independently by the Mainz group [7]. They put an upper limits on the effective ν_e mass by measuring the end-point of the electron energy spectrum which is $m_{\nu_e}^{eff.} < 2.05$ eV/c^2 [6] at 95 % confidence level (CL). In addition, an upper limit on the effective ν_e mass was obtained from neutrinoless double beta decay experiments which lies between 140 - 380 meV/c^2[2] at 90 % CL [8]. The upper limit on ν_μ was obtained from the accurate measurements of muon momentum from the decay of charged pion and it is $m_{\nu_\mu}^{eff.} < 0.17$ MeV/c^2 at 90 % CL [9]. Also the effective mass of $m_{\nu_\tau}^{eff.} < 18.2$ MeV/c^2 [10] was obtained from the reconstruction of hadrons from the tau decays at 95 % CL. It is known that the neutrino is a neutral particle. Nevertheless a stringent upper limit on neutrino charge, $q_\nu < 2 \times 10^{-15}$e was obtained from observations of neutrinos from the supernova SN1987A [11]. The neutrino magnetic moment (μ_ν) was measured by the GEMMA experiment from the study of $\bar{\nu}_e$ cross sections at a nuclear reactor, and is $\mu_\nu < 3.2 \times 10^{-11} \mu_B$ at 90 % CL [12] (μ_B is the Bohr magneton).

The evidence on the existence of 3 active neutrinos comes from the measurements of the decay width of the Z^0 boson at the Large Electron-Positron collider (LEP) experiment.

[2] The neutrinoless double beta decay mass limits are only true under the assumption that neutrinos are their own antiparticle (*i.e.* Majorana particles).

The Z^0 decays to visible hadrons (combination of q and $\bar{q}$, with $q \neq t$, a top quark), leptons, and also to (the invisible) neutrino-antineutrino pairs which go undetected in the detectors. The invisible partial decay width, Γ_{inv}, was estimated from the measured visible partial widths, corresponding to the Z^0 decays into quarks and charged leptons which were subtracted from the total Z^0 width. Four experiments, the ALEPH, the DELPHI, the L3 and the OPAL, all measured the cross section for, $e^+ + e^- \rightarrow hadrons$, as a function of the center of mass energy [13]. A combined analysis of all the LEP data measured 2.920 ± 0.05 [14] light neutrino families, which is an excellent agreement for existence of 3 active light neutrino as shown in Fig. 1.2. Beyond this, there are several studies on neutrino are going on using neutrinos from the various sources.

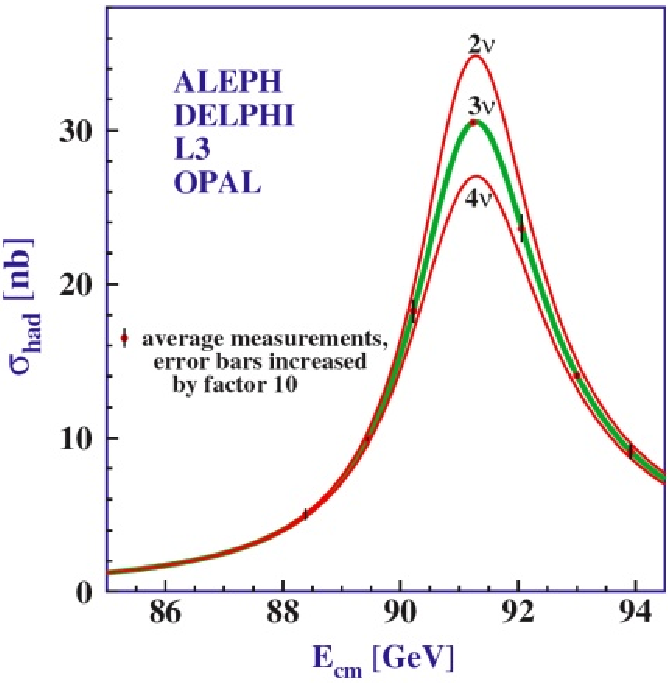

Figure 1.2: The hadron production cross-section due to e^+ - e^- collision around the Z^0 resonance as a function of centre of mass energy [13]. Curves show the predicted cross-section for two, three, and four neutrino species.

1 Sources of Neutrinos

Neutrinos are produced by several natural and artificial sources. The neutrino flux due to natural sources, with the exception of the sun, *viz.* atmospheric, supernova, from the earth interior (geoneutrinos) is fairly weak over the entire Earth's surface. We cannot control the energy and intensity of these naturally produced neutrinos. However, the accelerator - , radioactive - and reactor - based sources produce a well controlled and/or intense flux. A desirable source for the experiment would be to have as many of the neutrinos as possible passing through the detector and should stay over a long distance from the source. Depending upon the source, the energy ranges from meV to TeV. The production mechanism of neutrinos for some of these sources are described below.

1.1 Solar Neutrinos

The Sun produces energy along with an intense flux of neutrinos due to thermonuclear fusion reactions in which the hydrogen is transformed to helium. The Sun is a pure electron-neutrino[3] source. It does not produce electron antineutrinos and, in particular, no other neutrino flavours (ν_μ, ν_τ). In the Sun, the dominant process due to which energy is produced is the so-called pp chain reaction. In the pp chain, neutrinos are produced in the following reactions,

$$
\begin{aligned}
p + p &\rightarrow d + e^+ + \nu_e \text{ , (pp)} \\
p + e^- + p &\rightarrow d + \nu_e \text{ , (pep)} \\
d + p &\rightarrow {}^3He + \gamma \\
{}^3He + p &\rightarrow \alpha + e^+ + \nu_e \text{ , (hep)} \\
{}^3He + {}^3He &\rightarrow \alpha + p + p \\
{}^3He + \alpha &\rightarrow {}^7Be + \gamma \\
{}^7Be + e^- &\rightarrow {}^7Li + \nu_e \text{ , (}^7\text{Be)} \\
{}^7Li + p &\rightarrow \alpha + \alpha \\
{}^8B &\rightarrow {}^8Be^* + e^+ + \nu_e \text{ , (}^8\text{B)} \\
{}^8Be^* &\rightarrow \alpha + \alpha
\end{aligned}
$$

Reactions and decays that produce neutrinos are pp, pep, hep, ^{7}Be and ^{8}B. In each reaction, neutrinos have a characteristic energy spectrum, as shown in Fig. 1.3. The major contribution comes from the initial pp chain reaction. About 86 % of solar neutrinos are produced in this reaction chain giving neutrinos of a relatively low energy ($E_{\nu_e}^{max} \sim 0.423$

[3]In nuclear fusion processes, the proton transforms into a neutron through the weak interaction, implying an up-quark changes to down quark. Thus, each time a neutron is formed, an electron neutrino is produced, p + p → d + e$^+$ + ν_e. Due to three body kinematics, neutrino has a continuous energy spectrum where the maximal energy depends on the reaction. However, in inverse β decay, the two body final state leads to a discrete energy spectrum.

MeV) for which most of detectors are insensitive. There are two nuclear transitions that occur when ^{7}Be captures an electron, producing neutrinos with two different characteristic energies as shown in Fig. 1.3. The neutrino energy corresponding to the transition from the ground-state of ^{7}Be to the ground-state of ^{7}Li is about 0.862 MeV (90 %) and the energy corresponding to the transition to the first excited state of ^{7}Li is about 0.385 MeV (10 %). At high energy ($E_{\nu_e}^{max} \sim 15$ MeV), the flux of solar neutrinos is dominated by the ^{8}B decay but the contribution is only at the level of 0.02 % and most experiments are sensitive to these neutrinos.

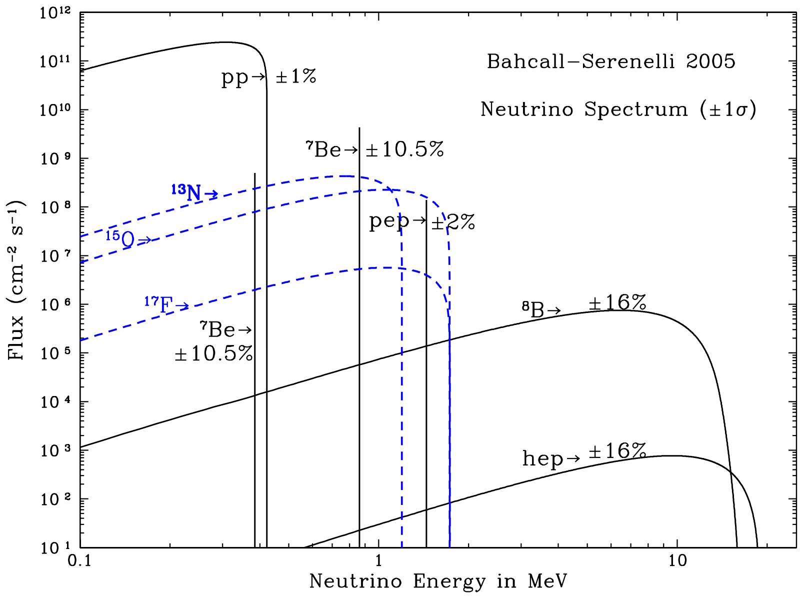

Figure 1.3: The energy spectrum of solar neutrino from the BS05(OP) standard solar model [16]. The neutrino fluxes from continuum sources are given in cm^{-2} s^{-1} MeV^{-1} at one astronomical unit, and the line fluxes are given in cm^{-2} s^{-1}.

These neutrinos produced in the core of the Sun take only two seconds to reach its surface and another eight minutes or so to reach the Earth. As a result, neutrinos provide information of what happened in the center of the Sun eight minutes ago. The study of solar neutrinos gives fundamental information not only about stellar structure and its evolution but also about properties of neutrinos, due to the wide range of matter densities that they encounter in the Sun and the large distance that they travel before arriving at the Earth. Clearly, to study neutrino properties, one needs to know their flux and the energy spectrum at the source. The number of neutrinos produced by the Sun is about 1.8×10^{39} [15] per second. The neutrino flux at the Earth's surface is about 6×10^{10} cm^{-2} s^{-1} in the energy range of E $\leq$ 0.42 MeV and about 5×10^6 cm^{-2} s^{-1} in the energy range 0.8 MeV $\lesssim$ E $\leq$ 15 MeV [15, 17]. About 60 billion solar neutrinos pass through an average fingernail (1 cm^2) every second and the human body captures a neutrino about once in a lifetime. The first solar neutrino events were observed using a radiochemical method by Ray Davis and colleagues in 1968 at the Homestake Mine in North Dakota [18]. There are several other experiments designed to measure solar neutrinos [19–29]. The measurements of solar neutrinos open a path for neutrino astrophysics.

1.2 Atmospheric Neutrinos

Atmospheric neutrinos are produced due to the interaction of primary cosmic rays with nuclei, mostly in the upper layer of the atmosphere at an average height of about 15 km. Primary cosmic rays are composed mostly of protons (~ 90 %), alpha particles (~ 9 %) and a small amount of heavier nuclei (~ 1 %). In collisions of high energy p(He) with nuclei of air, hadrons are produced, as in the equation below,

$$p(He) + A_{air} \rightarrow X + \pi, K, \; etc. \tag{1.2}$$

where A_{air} is nuclei in the air (N, O *etc.*) and X stands for some hadrons. Then, neutrinos are produced in the decay of mesons, as follows

$$\pi^{\pm} \rightarrow \mu^{\pm}\nu_{\mu}(\bar{\nu}_{\mu}) \tag{1.3}$$

$$K^{\pm} \rightarrow \mu^{\pm}\nu_{\mu}(\bar{\nu}_{\mu}). \tag{1.4}$$

Further, depending upon their energy, some of these muons decay to produce neutrinos,

$$\mu^{\pm} \rightarrow e^{\pm}\bar{\nu}_{\mu}\nu_{e}(\nu_{\mu}\bar{\nu}_{e}) \tag{1.5}$$

The resulting atmospheric neutrinos therefore are expected to follow the ratio $N_{\nu_\mu} : N_{\nu_e} = 2 : 1$ at low energy (E $\leq$ 1 GeV), where N_{ν_μ} and N_{ν_e} are total number of muon- and electron-type neutrinos. For higher energy (E > 1 GeV) neutrinos, this flavour ratio becomes greater than two, since the flight distance for pions and muons becomes longer resulting in a reduction in probability of decay which decreases the number of electron neutrinos. There is also zenith angle dependent symmetric (up/down) flux distribution. However, at low energy (E$_\nu$ ~ several GeV) up/down symmetry is affected by the rigidity cutoff of the primary cosmic rays due to the geomagnetic field [30].

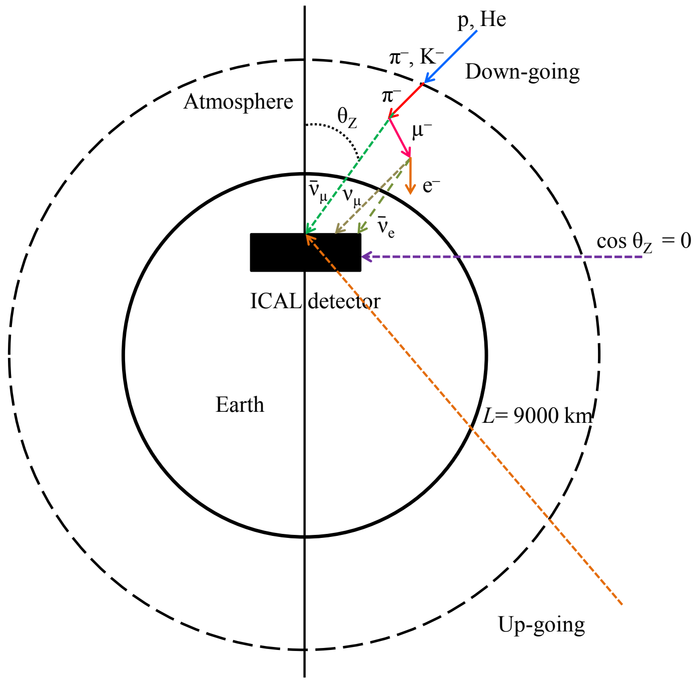

Figure 1.4: Schematic of atmospheric neutrino experiment at the INO. 'L' is the source to detector distance and θ_z is the zenith angle.

The main advantage of atmospheric neutrinos is that they cover a wide range of energy starting from few MeV to hundreds of GeV as well as path lengths from $\sim$ 15 km to $\sim$ 13,000 km. The typical flux of atmospheric neutrinos arriving at a detector on the surface of the Earth is $\sim 10^{-1}$ cm^{-2}s^{-1}. Neutrinos with energies in the range of $\sim$ 100 MeV to $\sim$ 100 GeV may be detected in underground laboratories through their scattering on nuclei. Atmospheric neutrinos were, however, first detected using large area liquid scintillation detector as neutrino-induced muons in an iron calorimeter in a deep mine at the Kolar Gold Fields of India [31] and in a mine in South Africa [32]. The idea of putting a detector in underground is to reduce the secondary cosmic rays background. Figure 1.4 shows the schematic of the proposed underground iron calorimeter (ICAL) detector at the India-based Neutrino Observatory (INO) which will measure neutrino oscillation parameters using atmospheric neutrinos as a source. In addition there are several other experiments which measure atmospheric neutrinos [33–35].

1.3 Geoneutrinos

The Earth contains a certain amount of natural radioactive nuclei, and the decay of these elements contribute about 19 TW to geothermal heat. These same decays also produce neutrinos known as geoneutrinos and are predominantly electron (anti-) neutrinos. They are produced due to the β-decay and electron capture of ^{238}U, ^{232}Th and ^{40}K. The list of properties of these isotopes and of the (anti-) neutrinos produced from their decay (chains) is given in Table 1.1. The flux of neutrinos coming from this natural radioactivity is about 6×10^{6} cm^{-2} s^{-1}. As neutrinos are produced in the Earth interior with their extremely

Table 1.1: Properties of radioactive isotopes ^{238}U, ^{232}Th, ^{40}K and maximum energy of neutrino produced by them [36].

Decay	Natural isotopic Abundance	$T_{1/2}$ (10^9) yr	E^{ν}_{max} (MeV)
$^{238}\text{U} \rightarrow {}^{206}\text{Pb} + 8\,{}^{4}\text{He} + 6\text{e} + 6\,\bar{\nu}_e$	0.9927	4.47	3.26
$^{232}\text{Th} \rightarrow {}^{208}\text{Pb} + 6\,{}^{4}\text{He} + 4\text{e} + 4\,\bar{\nu}_e$	1.0000	14.0	2.25
$^{40}\text{K} \rightarrow {}^{40}\text{Ca} + \text{e} + \bar{\nu}_e$ (89 %)	1.17×10^{-4}	1.28	1.311
$^{40}\text{K} \rightarrow {}^{40}\text{Ar} + \nu_e$ (11 %)	1.17×10^{-4}	1.28	0.044

small interaction cross-section, they carry information to the Earth's surface from the entire planet. It is possible to reveal the distribution of long-lived radioactive nuclei in the Earth by measuring the geoneutrino energy dependent flux. It will also help in assessing the radiogenic contribution to the total heat balance of the Earth. This information can be used to understand the generation of the Earth's magnetic field. These neutrinos are detected by inverse beta decay (IBD) process with threshold of about 1.8 MeV and hence neutrinos from ^{238}U and ^{232}Th are detectable (see Table 1.1). The first experimental investigation of geo-neutrinos from ^{238}U and ^{232}Th was performed by the KamLAND Collaboration [37], followed by an observation with a high statistical significance of 99.997 % CL by Borexino experiment [38].

1.4 Supernova Neutrinos

When a supergiant star has exhausted its nuclear fuel, its life ends with a huge explosion called the 'Supernova'. In this process, an enormous amount of energy is released in the form of light and neutrinos. Neutrinos carry about 99 % of the released gravitational binding energy from the supernova and have an energy of several tens of MeV. About 6×10^{58} neutrinos of all three active flavours are emitted in a period of $\sim$ 10 s. Due to their small interaction cross-section, neutrinos carry information from the heart of the explosion and, offer the only direct probe of the dynamics and thermodynamics at the center of a supernova. Supernova SN1987A which appeared in the Large Magellanic

Cloud (LMC) is the only one which was detected also through its neutrino burst by the two water Cerenkov detectors, Kamiokande II [39] and IMB [40] using the IBD reactions.

1.5 Reactor Neutrinos

Nuclear reactors are copious sources of electron anti-neutrinos. In a nuclear reactor, thermal power comes from the energy produced in the fission of heavy elements (i.e. ^{236}U, ^{240}Pu and ^{242}Pu) into neutron rich fission fragments. These fission products undergo β-decay and produce anti-neutrinos with a mean energy of $\sim$ 3 MeV. Typical modern commercial light-water reactors have thermal powers in the order of 1 GW. Since, on an average, each fission process produces $\sim$ 200 MeV and $\sim$ 6 $\bar{\nu}_e$, as a result the typical yield is $\sim 2 \times 10^{20}$ $\bar{\nu}_e$ s^{-1} at 1 GWth power. Although the interaction cross section between matter and neutrinos is very small ($\sim$10^{-43} cm^2), the huge emitted flux allows us to detect them with a relatively small mass detector (*e. g.* 1 ton) placed at a few meters from the core of the reactor. Antineutrinos from the reactor interact with protons in the detector via the IBD reaction,

$$\bar{\nu}_e + p \rightarrow n + e^+ \tag{1.6}$$

The positron which carries almost all of the energy, rapidly loses its energy in the detector and gets annihilated producing two gamma rays. The energy loss of the positron constitutes the 'prompt' signal along with the Compton scattered annihilation gamma rays. Hence,

$$E_{prompt} = E_{\bar{\nu}_e} + Q + 2m_e c^2, \tag{1.7}$$

where Q $\sim$ -1.8 MeV and $E_{\bar{\nu}_e}$ is the energy of antineutrino. This prompt pulse is followed by a delayed signal induced by the radiative capture of the thermal neutron by a proton with the emission of gamma of total energy $\sim$ 2.2 MeV. The correlation between the prompt and the delayed signal uniquely identifies the IBD event. The threshold of $\sim$ 1.8 MeV implies that only about 25 % [41] of the total antineutrinos produced in a reactor can be detected. Based on the IBD detection method, in 1956, the reactor anti-neutrino was first measured by Reines and Cowan [2]. There are several other experiments which measured reactor antineutrinos [42–47]. The reactor neutrino does not have sufficient energy to produce a muon (or a tau) and hence the $\bar{\nu}_e$s are detected using the disappearance channel for studying neutrino oscillations. Neutrinos from the reactor are not only used for studying the neutrino oscillation phenomena but also for monitoring and safeguarding the nuclear reactor. The antineutrino spectra is affected by relative yields of fissioning isotopes which depend on the isotopic composition of the core. Hence, measurements of antineutrino spectra may therefore provide an alternative means for verifying the power history and fissile inventory of a reactor.

1.6 Accelerator Based Neutrinos

1.6.1 Neutrino beams from pion decay

A high intensity neutrino beam called a ‘super beam’ is produced from the decay of mostly secondary pions. In an accelerator, a proton beam hits a thick nuclear target producing secondaries such as pions and kaons. The pion and the kaon are allowed to decay in flight while passing through a tunnel of length $\sim$ 100 m. The beam is composed of ν_μ’s or $\bar{\nu_\mu}$’s, depending on the polarity of the horn which focalizes pions and kaons of a given charge (+/−). In consequence a pure ν_μ beam is produced by π^+ , $K^+ \to \mu^+ + \nu_\mu$, with about 1 % contamination of ν_e due to the decay of muon. The typical energy of neutrinos is $\sim$ few GeV, but can be much larger, depending on the energy of the proton beam. The first accelerator based neutrinos were produced by L. M. Lederman, N. Mistry, M. Schwartz, and J. Steinberger in 1962. However, K2K is the first accelerator based experiment to measure neutrino oscillation. Presently there are several experiments all over the world which use accelerator-based neutrinos to measure the oscillation parameters [48–53].

1.6.2 Neutrino Factories

Muon decays are also excellent sources of neutrinos. The energy spectrum of such a beam is known to a high degree of precision as the physics and kinematics of muon decay are well understood. In the proposed neutrino factory, neutrinos having a well defined energy are produced due to decay of stored muons. In order to produce muons, an intense proton beam of power few MW at moderate energy (beams of 2 - 50 GeV) hits a production target, typically a high-Z material, and produces secondary pion beams. The pion quickly decays (mean life time, $\tau \sim 26$ ns) into a longer-lived ($\tau \sim 2.2$ μs) muon and neutrino. In order to create high energy neutrinos, the muons are “cooled” and accelerated to the desired final energy of a few tens of GeV, and stored in a decay ring. The muons decay via $\mu^- \to e^- + \bar{\nu}_e + \nu_\mu$, $\mu^+ \to e^+ + \nu_e + \bar{\nu}_\mu$, with the neutrinos having a range of energies up to the energy of accelerated muons. Thus this tertiary neutrino beam consists of a pure mix of 50 % ν_μ ($\bar{\nu}_\mu$) and 50 % ν_e ($\bar{\nu}_e$).

1.6.3 Beta Beam

The novel concept of producing a flavour pure electron neutrino beam in the beta decay of unstable mother nuclei was first proposed by P. Zucchelli in 2002 [54]. In this case, accelerated protons of few GeV hit a target producing the beta-unstable radioactive nuclides. These are then extracted and put through an ion source after which these ions are accelerated to a high energy and stored in a decay ring (analogous to muons in a Neutrino Factory). A very pure beam of ν_e or $\bar{\nu}_e$ is produced depending upon the the radioactive isotope whether it is a β^+ or a β^- emitter. The energy distribution of neutrinos can be predicted to a very high accuracy due to the well understood kinematics of beta decay. The advantage here is the complete absence of a intrinsic beam contamination of neutrinos of different flavours compared to the conventional neutrino beam produced due to the decay of pions.

2 Motivation of Thesis

The phenomenon of neutrino oscillation was already established by several experiments using the neutrino from various sources. The precise measurements of oscillation parameters are going to be carried out using several next generation upgraded detectors or new proposed detectors. The precise measurements of oscillation parameters, $\sin^2 2\theta_{23}$, Δm^2_{31} and the ordering of neutrino masses *i.e.* $\Delta m^2_{32} > 0$ or $\Delta m^2_{32} < 0$, are going to be carried out using the proposed massive magnetized ICAL detector at the INO using atmospheric neutrinos. There are also experimental indications of the presence of sterile neutrinos. The atmospheric ν_μ and $\bar{\nu}_\mu$ fluxes can be significantly altered due to the presence of eV^2-scale active-sterile oscillation. The ICAL detector at the INO can also be used to study its sensitivity to the active-sterile neutrino mixing. The magnet is the heart of the ICAL detector which acts as a target for atmospheric neutrinos and helps to measure the momentum and identify the charged particles, in particular, the neutrino induced muons. In this thesis, a study has been carried out on the design aspect, in particular, the electromagnetic simulation of the ICAL magnet. The optimization has been done on various parameters of the magnet considering several configurations in order to get a uniform field at the least possible power loss in the current carrying coils. The energy resolution and efficiency of muon reconstruction strongly depends on the strength of the magnetic field. So, the simulated magnetic field was used for studying the muon response using the GEANT4 simulation, for optimizing its strength. The study has been also carried out on active-sterile neutrino mixing sensitivity at an exposure of 1 Mton-yr and found a limit of mixing parameters for which the ICAL is sensitive.

The thesis is organized in various chapters. In Chapter 2, a discussion is carried out on neutrino oscillations for various generations and the current status of the oscillation parameters is presented. The description of the electromagnetic simulation of the ICAL magnet is presented in Chapter 3. The optimization of magnetic field strength with respect to the muon response is discussed in Chapter 4. Studies on the active-sterile neutrino mixing sensitivity of the magnetized ICAL detector at the INO are described in Chapter 5. The conclusions and summary based on our study are presented in Chapter 6.

Chapter 2

Neutrino Oscillation

In this chapter the basis of the phenomenon of neutrino flavour oscillations is discussed. The chapter starts with the formalism for neutrino oscillation and discussion on 2-ν and 3-ν flavour mixing in vacuum. In the following sections the experimental evidence for neutrino oscillation is described. Then, the present status of the 3 generation neutrino mixing parameters are highlighted. Finally the possibility of the existence of sterile neutrinos and the importance of their experimental searches is discussed in detail.

1 Neutrino mixing in Vacuum

In the SM, neutrinos are massless and hence do not oscillate from one flavour to another flavour. The quantum mechanical phenomena of neutrino oscillation was first proposed by B. Pontecorvo. He had considered the possibility of neutrino-antineutrino oscillation, which is similar to the oscillation in the neutral kaon system [55]. After the discovery of ν_μ, in 1962, Maki, Nakagawa, and Sakata expanded on Pontecorvo's idea, introducing the theory of neutrino flavour oscillation [56]. On the other hand, the first phenomenological model was given by Pontecorvo [57] for $\nu_e \leftrightarrow \nu_\mu$ mixing and oscillation which was further improved by Gribov and Pontecorvo [58].

The neutrino oscillations are a periodical process in time (or space) which describe a complete or partial transformation of one flavour into another after traveling certain distance in space. In this process, neutrinos are created and detected as weak, or flavour eigenstates, but propagate as a superposition of mass eigenstates which are solutions of the time-dependent Schroedinger equation. The difference in masses between the mass eigenstates causes an oscillation between the flavours. The flavour oscillation accounts for the possible conversion between electron, muon and tau neutrinos. However, the neutrino oscillation from one flavour to another violates the conservation of lepton number and thus goes beyond the SM of particle physics. Neutrino oscillations take place when physical mass eigenstates ν_i differ from flavour eigenstates ν_α, where ν_α is defined to the neutrino state which connects to a charged lepton α via charged current (CC) interaction. Neutrinos produced due to a CC interaction are in pure flavour states at time $t = 0$ and the initial flavour eigenstate ν_α can be expressed as a linear combination of the mass eigenstates ν_k,

$$|\nu_\alpha(t=0)\rangle = \sum_k U^*_{\alpha k} |\nu_k(t=0)\rangle , \tag{2.1}$$

where U is a unitary Pontecorvo-Maki-Nakagawa-Sakata (PMNS) [56] mixing matrix and 'k' is summed over the mass eigenstates. The neutrino of flavour α after a time interval of 't' is given by

$$|\nu_{\alpha(t)}\rangle = \sum_k U^*_{\alpha k} |\nu_k(t)\rangle , \tag{2.2}$$

where $|\nu_k(t)\rangle$ the mass eigenstate after a time interval 't' which is the solution of time-dependent Schroedinger equation with no potential, given by

$$i\frac{d\,|\nu_k(t)\rangle}{dt} = E\,|\nu_k(t)\rangle , \tag{2.3}$$

which implies

$$|\nu_k(t)\rangle = e^{-iE_k t} |\nu_k(0)\rangle . \tag{2.4}$$

Here we assume natural units *viz.* $\hbar = \mathrm{c} = 1$. By using Eq. 2.4 in Eq. 2.2, the time propagation equation of flavour eigenstate of the neutrino can be written as,

$$|\nu_\alpha(t)\rangle = \sum_k \sum_\gamma U^*_{\alpha k} e^{-iE_k t} U_{\gamma k} |\nu_\gamma(0)\rangle . \tag{2.5}$$

In case of a transition from $\nu_\alpha(0)$ to $\nu_\beta(t)$, the corresponding amplitude is given as

$$\begin{aligned} A(\nu_\alpha(0) \to \nu_\beta(t)) &= \langle \nu_\beta(t)|\nu_\alpha(0)\rangle \\ &= \sum_k \sum_\gamma U_{\beta k} e^{iE_k t} U^*_{\gamma k} \langle \nu_\gamma(0)|\nu_\alpha(0)\rangle \\ &= \sum_k U_{\beta k} e^{iE_k t} U^*_{\alpha k} . \end{aligned} \tag{2.6}$$

The flavour transition probability $\nu_\alpha \to \nu_\beta$ after a time interval t is given as

$$\begin{aligned} P(\nu_\alpha \to \nu_\beta) &= |\sum_k U_{\beta k} e^{iE_k t} U^*_{\alpha k}|^2 \\ &= \sum_k \sum_j U_{\beta k} U^*_{\alpha k} U^*_{\beta j} U_{\alpha j} e^{-i(E_j - E_k)t} . \end{aligned} \tag{2.7}$$

After applying the properties of unitary matrix, *i.e.* $UU^\dagger = I$, where I is a unit matrix, then Eq. 2.7 may be expressed as,

$$P(\nu_\alpha \to \nu_\beta) = \sum_k U_{\beta k} U^*_{\alpha k} \sum_j U_{\beta j} U^*_{\alpha j} + \sum_k \sum_j U_{\beta k} U^*_{\alpha k} U^*_{\beta j} U_{\alpha j} (e^{-i(E_j - E_k)t} - 1) , \tag{2.8}$$

which can be further simplified as

$$P(\nu_\alpha \to \nu_\beta) = \delta_{\alpha\beta} + 2 \sum_{j>k} Re \left[U_{\beta k} U^*_{\alpha k} U^*_{\beta j} U_{\alpha j} (e^{-i(E_j - E_k)t} - 1) \right] . \tag{2.9}$$

For the extremely relativistic case, $E \gg m_k$ (also $E \approx p$), E_k is expanded as $E_k = \sqrt{p^2 + m_k^2} \simeq p + m_k^2/2p \simeq p + m_k^2/2E$ (assuming neutrinos have the same momentum but slightly different energies due to the different masses), the survival probability for the neutrino with energy, E, after traveling a distance, L ($t \equiv L$), from the origin is given by

$$P(\nu_\alpha \to \nu_\beta) = \delta_{\alpha\beta} + 2 \sum_{j>k} Re \left[U_{\beta k} U^*_{\alpha k} U^*_{\beta j} U_{\alpha j} (e^{-i(\frac{\Delta m^2_{jk} L}{2E})} - 1) \right] , \tag{2.10}$$

where $\Delta m^2_{jk} = m_j^2 - m_k^2$ at $j > k$. The probability of oscillation can be further simplified by considering the following,

$$e^{-i\zeta} = cos(\zeta) - i sin(\zeta) , \tag{2.11}$$

and expressing $cos(\zeta) = 1 - 2\ sin^2(\frac{\zeta}{2})$, we have

$$\begin{aligned} P(\nu_\alpha \to \nu_\beta) = \delta_{\alpha\beta} &- 4 \sum_{j>k} Re \left[U_{\beta k} U^*_{\alpha k} U^*_{\beta j} U_{\alpha j} \right] sin^2(\frac{\Delta m^2_{jk} L}{4E}) \\ &+ 2 \sum_{j>k} Im \left[U_{\beta k} U^*_{\alpha k} U^*_{\beta j} U_{\alpha j} \right] sin(\frac{\Delta m^2_{jk} L}{2E}) . \end{aligned} \tag{2.12}$$

It may be noted here that to obtain the oscillation probabilities for anti-neutrinos, we have to replace the matrix U by its complex conjugate (U^*) in Eq. 2.12.

1.1 Two flavour Oscillation Formalism

To simplify the discussion, let us first consider oscillation only between two neutrino flavours, ν_α and ν_β. They are linear superpositions of the two massive states ν_1 and ν_2 with coefficients of the elements of the two-neutrino effective unitary mixing matrix, U, given by

$$\begin{pmatrix} \nu_\alpha \\ \nu_\beta \end{pmatrix} = \begin{pmatrix} cos\theta & sin\theta \\ -sin\theta & cos\theta \end{pmatrix} \begin{pmatrix} \nu_1 \\ \nu_2 \end{pmatrix}. \tag{2.13}$$

where the angle, θ, is a measure of the mixing between flavour and mass eigenstates, takes any value in the interval $0 \le \theta \le \pi/2$. It may be observed that the mixing matrix U is analogous to the rotation between the mass eigenstates and the flavour states. The oscillation probability for 2-ν formalism can be obtained from Eq. 2.12 for which the imaginary part is zero since the mixing matrix, U, in Eq. 2.13 is real. Hence the probability of appearance ν_β from the original ν_α is expressed as

$$P(\nu_\alpha \to \nu_\beta) = sin^2 2\theta \; sin^2\left(\frac{1.27\,\Delta m^2_{21} L}{E}\right), \tag{2.14}$$

where $\Delta m^2_{21} \equiv m^2_2 - m^2_1$. Here L is measured in km, Δm^2 is measured in (eV/c^2)^2, and E is measured in GeV. Similarly the survival (or disappearance) probability for the flavour ν_α is expressed as

$$P(\nu_\alpha \to \nu_\alpha) = 1 - sin^2 2\theta \; sin^2\left(\frac{1.27\,\Delta m^2_{21} L}{E}\right). \tag{2.15}$$

There are two possible ways to detect neutrino flavour oscillations. The first technique is based on the "appearance" channel of the neutrino oscillation as given in Eq. 2.14 in which ν_β is detected from a known neutrino flux ν_α. However, the observation of ν_β by measuring the charged lepton which was produced in the CC interaction requires sufficient energy. In the second technique which is based on the "disappearance" channel of neutrino oscillation as given in Eq. 2.15 where the detected neutrino flux of ν_α is smaller than the expected flux compared to that in the absence of oscillations. The probability of oscillation for an energy, E = 1 GeV, at $\sin^2\theta = 0.437$ and $\Delta m^2 = 2.4 \times 10^{-3}$ eV^2 is shown in Fig. 2.1. The black and red lines show the probabilities for the appearance and disappearance channels of oscillation, respectively. It is observed that at some point along the path between source and detector almost all of the ν_α will oscillate to ν_β. The amplitude

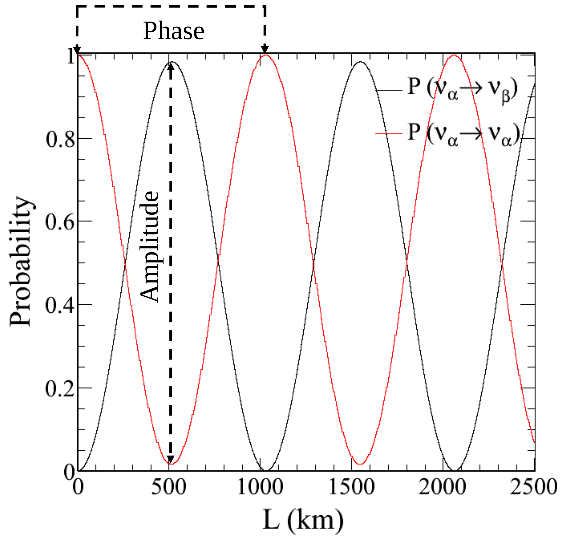

Figure 2.1: The survival $P(\nu_\alpha \to \nu_\beta)$ (black line) and oscillation $P(\nu_\alpha \to \nu_\alpha)$ (green line) probability for $\sin^2\theta = 0.437$, $\Delta m^2 = 2.4 \times 10^{-3}$ eV^2 and E = 1 GeV as a function of L(km).

of oscillation is decided by the factor $sin^2 2\theta$. For a given L and E, the mass squared difference, Δm^2, controls the oscillation phase and determines the position of maximum or minimum of the oscillation probability. It is clear that for neutrino oscillations to occur, at least one of the mass states must be non-zero and also masses of the mass eigenstates must be different, $\Delta m^2 \neq 0$. If there is no mixing ($\theta = 0$) and/or ($\Delta m^2 L/E$) << 1, the oscillation probability becomes zero or small. It may be noted that neutrino oscillation experiments give us information on the difference between the squared masses, but cannot tell us what are the absolute masses. The neutrino oscillation in vacuum cannot provide information about the ordering of masses *i.e.* whether m_1 is greater than m_2. If $\Delta m^2 \to -\Delta m^2$, the oscillation probability will still be the same. To have an appreciable transition probability, not only should the neutrino mixing be sizable but the propagation distance should also be a reasonable fraction of the oscillation length, $L_{osc} \sim 2.48\ E/\Delta m^2$. At a given Δm^2, the probability of oscillation will change depending upon L/E. To set up an experiment having maximal sensitivity to the oscillation probability we have

$$\frac{1.27 \times \Delta m^2 \times L}{E} = \frac{\pi}{2}$$
$$\Rightarrow \frac{L}{E} = \frac{\pi}{2.54 \times \Delta m^2} .$$

In addition, to measure Δm^2 more precisely, it is important to measure the source to detector distance as well as energy with very good accuracy. Otherwise the averaging over the different phases lead to a washing out of the oscillation probabilities and one gets an average value 1/2, losing the sensitivity to Δm^2.

1.2 Three flavour Oscillation

In a system with three flavours of neutrino, the mixing becomes more complicated. A general unitary n × n mixing matrix for Dirac particles can be parametrized by n(n − 1)/2 rotation angles and n(n + 1)/2 complex phase factors, of which 2n − 1 can be absorbed into a redefinition of the particle fields. Hence, for a 3 × 3 unitary matrix, there are three independent mixing angles θ_{12}, θ_{23}, θ_{13}, and one complex phase δ_{CP}, which is responsible for CP violation in the neutrino sector. These values are used to parametrize the mixing matrix, U. In case of 3-ν flavours oscillation, there are two independent squared mass differences, Δm^2_{21}, Δm^2_{32}, where $\Delta m^2_{ji} = m^2_j - m^2_i$ with i, $j = 1, 2, 3$ and $j > i$. The unitary 3 × 3 PMNS matrix which describes the mixing between 3-flavour eigenstates to 3-mass eigenstates is given as

$$\begin{pmatrix} \nu_e \\ \nu_\mu \\ \nu_\tau \end{pmatrix} = \begin{pmatrix} U_{e1} & U_{e2} & U_{e3} \\ U_{\mu 1} & U_{\mu 2} & U_{\mu 3} \\ U_{\tau 1} & U_{\tau 2} & U_{\tau 3} \end{pmatrix} \begin{pmatrix} \nu_1 \\ \nu_2 \\ \nu_3 \end{pmatrix}, \tag{2.16}$$

where U_{e1} measures the amount of ν_e flavour in the mass eigenstate $|\nu_1\rangle$, $U_{\mu 2}$ measures the amount of ν_μ flavour in the mass eigenstate $|\nu_2\rangle$ and similarly $U_{\tau 3}$ measures the amount of ν_τ flavour in the mass eigenstate $|\nu_3\rangle$. The usual convention for the mixing matrix is in terms of product of the three rotation matrices,

$$U = R(\theta_{23}, 0)R(\theta_{13}, \delta)R(\theta_{12}, 0), \tag{2.17}$$

where R_{ij} represents the rotation between i^{th} and j^{th} mass eigenstate and δ is the Dirac CP violating phase. The Eq. 2.16 can be further expressed as

$$U = \begin{pmatrix} 1 & 0 & 0 \\ 0 & c_{23} & s_{23} \\ 0 & -s_{23} & c_{23} \end{pmatrix} \times \begin{pmatrix} c_{13} & 0 & s_{13}e^{-i\delta} \\ 0 & 1 & 0 \\ -s_{13}e^{i\delta} & 0 & c_{13} \end{pmatrix} \times \begin{pmatrix} c_{12} & s_{12} & 0 \\ -s_{12} & c_{12} & 0 \\ 0 & 0 & 1 \end{pmatrix}, \tag{2.18}$$

where $c_{ij} \equiv \cos\theta_{ij}$, $s_{ij} \equiv \sin\theta_{ij}$. If neutrinos are Majorana particles then there are two additional phase factors that appear in diagonal elements of one more matrix and not measurable in neutrino oscillation experiments.

The magnitudes of the rotation angles turn out to be such that the experimental data may be analyzed in terms of oscillations between just the two neutrino states. The first rotation, $R(\theta_{12}, 0)$, measures the mixing angle θ_{12} using data from solar (and reactor) neutrino experiments. The second rotation, $R(\theta_{13}, \delta)$ gives θ_{13} which was recently measured from several experiments using the reactor neutrinos as a source. The third rotation, $R(\theta_{23}, 0)$ depends on the angle θ_{23}, which was obtained from atmospheric and accelerator-based neutrino experiments. The above Eq. 2.18 can be further written as

$$U = \begin{pmatrix} c_{12}c_{13} & s_{12}c_{13} & s_{13}e^{-i\delta} \\ -s_{12}c_{23} - c_{12}s_{23}s_{13}e^{i\delta} & c_{12}c_{23} - s_{12}s_{23}s_{13}e^{i\delta} & s_{23}c_{13} \\ s_{12}s_{23} - c_{12}c_{23}s_{13}e^{i\delta} & -c_{12}s_{23} - s_{12}c_{23}s_{13}e^{i\delta} & c_{23}c_{13} \end{pmatrix}. \tag{2.19}$$

From Eq. 2.19, mixing angles θ_{12}, θ_{23} and θ_{13} which parametrize the mixing matrix U can be defined in the following ways,

$$\frac{|U_{e2}|^2}{|U_{e1}|^2} \equiv tan^2\theta_{12}; \quad \frac{|U_{\mu 3}|^2}{|U_{\tau 3}|^2} \equiv tan^2\theta_{23}; \quad |U_{e3}|^2 \equiv sin^2\theta_{13}\,. \tag{2.20}$$

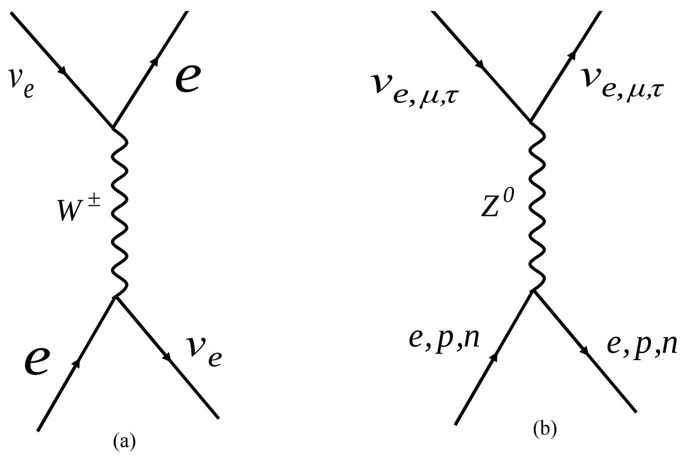

Figure 2.2: Feynman diagrams showing neutrino scattering within matter (a) the CC interaction and (b) the NC interaction

2 Matter Effect in Neutrino Oscillation

The formalism for neutrino flavour oscillations described above holds when the neutrinos are propagating in vacuum. The propagation of neutrino through matter modifies the mixing of neutrinos. It arises due to the scattering of neutrinos with electrons and nucleons in matter which was first discovered by Wolfenstein [59]. In 1985 S.P. Mikheev and A.Yu. Smirnov [60] discovered the possibility of resonant flavour transitions while neutrinos propagate in a medium with varying density.

Ordinary matter is composed of electrons, protons and neutrons, and the effective potential receives contributions from all these target particles. Hence, the NC interaction potentials of ν_e with electrons, protons and neutrons due to the exchange of the Z^0 boson are given as

$$\begin{aligned} V_{NC}^{\nu_e e} &= -\frac{\sqrt{2}}{2} G_F N_e \,, \\ V_{NC}^{\nu_e p} &= +\frac{\sqrt{2}}{2} G_F N_p \,, \\ V_{NC}^{\nu_e e} &= -\frac{\sqrt{2}}{2} G_F N_n \,, \end{aligned} \tag{2.21}$$

where G_F is the Fermi coupling constant, N_e, N_p and N_n are the number density of electrons, protons and neutrons, respectively in the medium. The number densities, N_e[1] and N_n are given by $N_e = \rho N_A Y_e$ and $N_n = \rho N_A(1 - Y_e)$, where ρ is the matter density in g/cm^3, $Y_e = Z/A$, is the electron number fraction and N_A is the Avogadro number. The interaction of electron type neutrino with matter is shown in Fig. 2.2. It may be observed that the contributions due to electron and proton are equal in magnitude and opposite in sign. Therefore, their contribution to the NC matter potential cancels due to neutrality of ordinary matter. Hence the remaining contribution to the NC interaction potential comes from the neutron which is flavour independent. Only the ν_e can interact with matter electrons coherently via a CC interaction with $W^{\pm}$ boson exchange (as ordinary matter contains electron not muons or taus). In case of CC scattering of the ν_e with the electron, the corresponding interaction potential is given as

$$V_{CC} = \sqrt{2} G_F N_e \,. \tag{2.22}$$

It may be noted here that the interaction potential changes sign from '+' to '−' while considering antineutrino instead of neutrino. At the two neutrino approximation (assuming system of ν_e/ν_μ), the time evolution of flavour eigenstates in matter is given by the Schroedinger equation which is as follows,

[1] $N_p = N_e$ due to neutrality of matter

$$\frac{d}{dt}\begin{pmatrix}\nu_\alpha\\ \nu_\beta\end{pmatrix} = \frac{1}{2E}\left[U\begin{pmatrix}m_1^2 & 0\\ 0 & m_2^2\end{pmatrix}U^\dagger + \begin{pmatrix}V_{CC}+V_{NC} & 0\\ 0 & V_{NC}\end{pmatrix}\right]\begin{pmatrix}\nu_\alpha\\ \nu_\beta\end{pmatrix}, \tag{2.23}$$

where U is the mixing matrix given in Eq. 2.13. Further, Eq. 2.23 can be further simplified as

$$\frac{d}{dt}\begin{pmatrix}\nu_\alpha\\ \nu_\beta\end{pmatrix} = H_f\begin{pmatrix}\nu_\alpha\\ \nu_\beta\end{pmatrix}, \tag{2.24}$$

where H_f[2] is effective Hamiltonian and expressed as,

$$\frac{1}{4E}\begin{pmatrix}-\Delta m^2 cos2\theta + 2A & \Delta m^2 sin2\theta\\ \Delta m^2 sin2\theta & \Delta m^2 cos2\theta\end{pmatrix}, \tag{2.25}$$

with $\Delta m^2 = m_2^2 - m_1^2$ and $A \equiv 2EV_{CC}$. The mass matrix in Eq. 2.24 is no longer diagonal due to the added potential. At constant matter density the above Eq. 2.24 is equivalent to a stationary one. So after diagonalizing the Hamiltonian H_f, the oscillation probability can be expressed as a function of the matter mass eigenstates and with a matter modified mixing angle. The modified 2-flavour oscillation probability is given as,

$$P(\nu_\alpha \to \nu_\beta) = sin^2 2\theta_M \; sin^2\left(\frac{1.27\,\Delta m_M^2 L}{E}\right), \tag{2.26}$$

where,

$$\Delta m_M^2 = \sqrt{(\Delta m^2 cos\,2\theta - A)^2 + (\Delta m^2 sin^2 2\theta)^2}, \tag{2.27}$$

$$sin^2 2\theta_M = \frac{sin^2 2\theta\,\Delta m^2}{\Delta m_M^2}. \tag{2.28}$$

It may be noted that at $A = \Delta m^2\cos2\theta$, the probability of oscillation is significantly enhanced, irrespective of the value of vacuum mixing θ and leads to a mixing in matter which is maximal *i.e.* $\theta_M = \pi/4$. This is known as the MSW resonance. Oscillation probabilities for neutrino and antineutrinos can be different due to matter effects (because of the $\pm$ sign in front of V_{CC}). The resonant condition occurs if $V_{CC} > 0$, which in turns depends on the sign of Δm^2. This dependence on the sign of Δm^2 can be used to determine the neutrino mass hierarchy.

[2]As the mixing angle does not change when same quantities are subtracted from all the diagonal elements

3 Experimental Evidence for Neutrino Oscillation

3.1 Solar Neutrino Problem

The measurement of solar neutrinos first indicated the possibility of neutrino oscillation. The Homestake radiochemical experiment measured neutrinos produced in the Sun, mainly due to the decay of ^{8}B, using the IBD reaction:

$$\nu_e + {}^{37}Cl \to {}^{37}Ar + e^- . \tag{2.29}$$

It was observed that the measured solar neutrino induced ^{37}Ar event rate is (2.56 ± 0.16 (stat.) ± 0.16 (syst.)) $\times\ 10^{-36}$ s^{-1} per ^{37}Cl atom [61], which is about 30% of the theoretically predicted rate. This came to be known as the solar neutrino problem. When this problem was identified, it was expected that it would be solved by measuring flux of solar neutrinos from the dominant pp-chain. Subsequently, there were several other radio chemical experiments, SAGE (Soviet–American Gallium Experiment) [19], GALLEX (GALLium EXperiment) [20] and later on GNO [21] that measured the solar neutrino flux using gallium as the target. All three experiments measured the event rate based on the following reaction,

$$\nu_e + {}^{71}Ga \to {}^{71}Ge + e^- . \tag{2.30}$$

The data from all 3 experiments provided a measured event rate of 66.1 ± 3.1 SNU (solar neutrino unit, corresponds to one reaction per 10^{36} target atoms per second), with statistical and systematic errors combined in quadrature [62]. This is about 50 % of the standard solar model (SSM) prediction [63].

In 1989, the Kamioka Nucleon Decay Experiment (Kamiokande) [22], reported their first results on the measurements of solar neutrino flux from ^{8}B. They used the water Cherenkov detector, measuring the neutrinos through their elastic scattering against electrons, which is sensitive for all types of neutrinos as follows,

$$\nu_\alpha + e^- \to \nu_\alpha + e^-, \tag{2.31}$$

where α can be e, μ or τ. The ratio of the average flux measured by Kamiokande to the SSM flux was 0.46 ± 0.13 (stat.) ± 0.08 (syst.). This is in agreement with the results of the gallium experiments. Results from the upgraded detector, Kamiokande III combined with flux from Kamiokande I, II gave a flux of 2.80 ± 0.19 (stat.) ± 0.33 (syst.) × 10^6 cm^{-2} s^{-1} which is 49% to 64% of the SSM flux [64]. The most precise results were given by the next generation Super-Kamiokande (SK) detector.

It may be noted here that all measurements consistently pointed to a deficit in solar neutrinos but do not, in a model independent manner, show the existence of neutrino oscillations. The radiochemical experiments are sensitive to the neutrino induced CC events and not able to measure the possibly converted muon or the tau neutrinos. Due to the smaller NC cross section, the SK can only measure the total flux, by combining the CC and NC data, with a poorer precision. To get conclusive evidence, it is necessary to measure all flavours of neutrino. Such a measurement was subsequently carried out by the SNO solar neutrino experiment. The heavy water based SNO detector measured ^{8}B solar neutrinos through,

$$\nu_e + {}^2H \to e^- + p + p \text{ (CC)}, \tag{2.32}$$

$$\nu_\alpha + {}^2H \to \nu_\alpha + p + n \text{ (NC)}, \tag{2.33}$$

$$\nu_\alpha + e^- \to \nu_\alpha + e^- \text{ (ES)}, \tag{2.34}$$

where ES stands for elastic scattering of neutrinos. The event rate due to CC interaction is sensitive to ν_e and measures only the flux of ν_e ($\phi(\nu_e)$). The ES reaction can be used to measure the flux of all active neutrino flavours. The dominant contribution comes from the ν_e as its interaction cross section with electrons is about 6 times that of the ν_μ or the ν_τ, since only ν_e type neutrinos are produced in the sun and the measurement of the ν_μ or the ν_τ provides a strong evidence for neutrino oscillation. So the SNO [28] experiment measured a flux of non-electron neutrino flavours by detecting them based on reactions Eq. 2.32 and Eq. 2.33, given as

$$\frac{\phi(\nu_e)}{\phi(\nu_e) + \phi(\nu_\mu) + \phi(\nu_\tau)} = 0.340 \pm 0.023\ (stat.)\ ^{+0.029}_{-0.031}\ (syst.), \tag{2.35}$$

where $\phi(\nu_\mu)$ and $\phi(\nu_\tau)$ are fluxes of ν_μ and ν_τ respectively. It may be observed from Eq. 2.35 that this clearly shows that the ν_e, produced in the sun is converted to other flavours ν_μ or ν_τ while traveling to the detector. The NC interaction process, sensitive to all three active neutrino flavours, allows a measurement of the total neutrino flux, *viz.* $\phi(\nu_e) + \phi(\nu_\mu) + \phi(\nu_\tau)$. So, the total active neutrino flux was measured to be 5.25 ± 0.16 (stat.) $^{+0.11}_{-0.13}$ (syst.) × 10^6 cm^{-2} s^{-1} [29], in very good agreement with the theoretically predicted 5.94 (1 ± 0.11) [SSM BPS08] or 5.58 (1 ± 0.14) [SSM SHP11] [65].

The evidence for neutrino oscillation from the SNO experiment was confirmed by the KamLAND reactor neutrino experiment. The liquid scintillator based detector detects $\bar{\nu}_e$ through the IBD process. The measurement showed a clear evidence for disappearance of $\bar{\nu}_e$ and consistent with solar neutrino results, assuming conservation of charge, parity and time reversal (CPT) symmetry. A combined analysis of the KamLAND and solar neutrino results gave the neutrino oscillation parameters Δm^2_{21} and the mixing angle θ_{12}.

3.2 Atmospheric Neutrino Anomaly

At low energies ($\leq$ 1 GeV), the flux of atmospheric neutrinos is due to the decay of mostly pions and muons. It may be noted from Eq. 2.2.2 and Eq. 2.2.4 that the ratio of neutrino flux (fluxes of neutrino and antineutrinos of a specific flavour), $\nu_\mu : \nu_e$ is about 2 : 1. The oscillation of atmospheric neutrinos can be observed in two ways: (1) by measuring the ratio of ν_μ to ν_e flux, (2) by measuring the zenith angle distribution of neutrinos. To study the $\nu_\mu : \nu_e$ flux ratio, most experiments calculate the double-ratio [3] on event rates which is defined as,

$$R = (N_\mu/N_e)_{obs}/(N_\mu/N_e)_{pred}\,, \tag{2.36}$$

where N_μ and N_e are number of ν_μ and ν_e events which interacted in the detector. In Eq. 2.36, the numerator represents the ratio of N_μ/N_e for observed data whereas the denominator represents the theoretically predicted data obtained from simulation. If there is no oscillation then the observed flavour composition agrees with the prediction which leads $R = 1$. However, experimental results were reported by the IMB and the Kamiokande which did not match with the theoretically predicted value. The ratio of observed data to theoretical prediction rate, was given by the IMB collaboration as R $\sim$ 0.54 $\pm$ 0.05 (stat.) $\pm$ 0.11 (syst.) [66] while the measurement by the SK collaboration gave, R $\sim$ 0.60 $^{+0.07}_{-0.06}$ (stat.) $\pm$ 0.05 (syst.) [67]. So $R < 1$ is known as the "Atmospheric Neutrino Anomaly". This deficit was unclear and various mechanisms were proposed to interpret the results. Further, the SK collaboration measured the angular distributions of atmospheric muon- and electron-like neutrino events. Atmospheric neutrinos reaching the detector are symmetric with respect to zenith angle so the the number of measured upward-going and the downward-going neutrinos should be equal. On the other hand, the SK collaboration compared their results with the Monte Carlo prediction and observed that the muon-like events due to the downward-going neutrino are more compared to the upward-going neutrinos whereas the electron-like events are the same for both the

[3] double ratios on event rates are considered to reduce the systematic uncertainties

upward-going and the downward-going neutrinos [33]. This was interpreted as strong evidence for neutrino oscillations.

3.3 Status of 3 Generation Neutrino Oscillation Parameters

In the last two decades, several measurements were carried out to try to measure accurately on the neutrino oscillation parameters. It was established that the neutrino has non-zero mass. In the 3 generation picture, there are in total six parameters which describe neutrino oscillations. However, at present we have measured values of the five oscillation parameters: two mass squared difference, Δm^2_{21}, $|\Delta m^2_{32}|$ and, three mixing angles, θ_{12}, θ_{13}, θ_{23}. The precision on measurements depends upon the specific class of experiments. The mixing angle θ_{12} and Δm^2_{21} (also known as Δm^2_{sol}, where, 'sol' stands for solar, first measured using solar neutrinos) are measured from combined analysis of data from the long-base line (LBL) reactor (KamLAND Collaboration) and solar neutrino (SNO Collaboration) based experiments. The value of θ_{23} was obtained from atmospheric neutrino data mainly from the Super-Kamiokande (SK) experiments, the magnitude of Δm^2_{32} (also known as Δm^2_{atm}, where 'atm' stands for atmospheric, first measured using atmospheric neutrinos) was determined by the LBL experiments, MINOS and T2K. Preliminary mea-

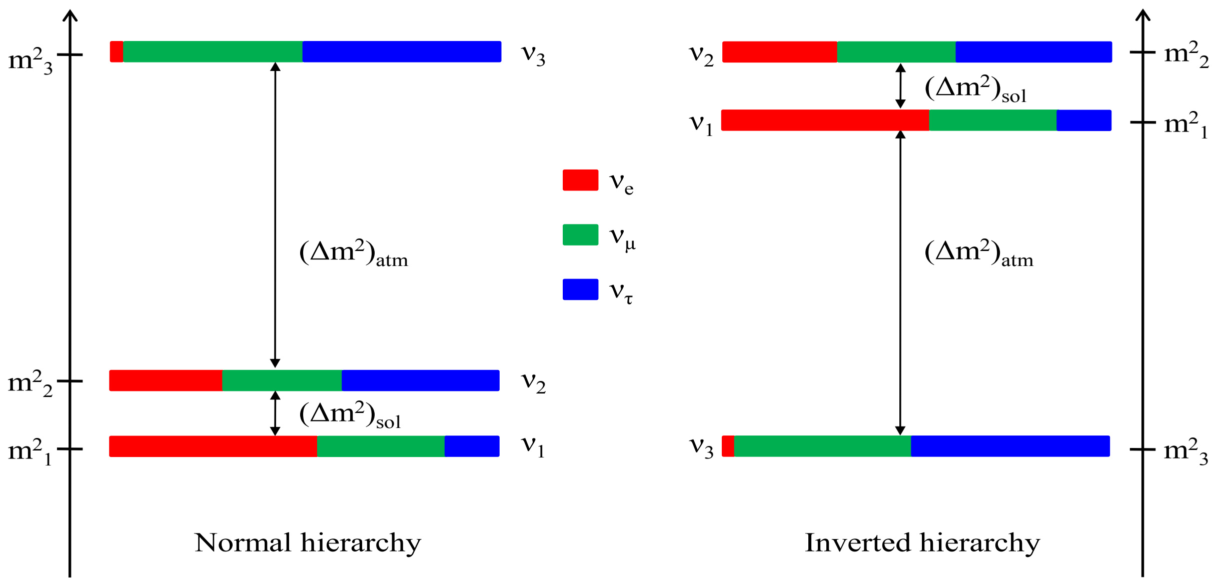

Figure 2.3: Two possible mass hierarchies of three flavours of neutrino. The ν_e, the ν_μ, and the ν_τ content of each mass eigenstate, denoted by colored bands, represents the level of mixing of each mass eigenstates with each weak eigenstate.

Table 2.1: Best fit and 3 σ ranges of 3 generation neutrino oscillation parameters obtained from the global 3-ν analysis [69].

Parameters	Best Fit	3 σ range
$\Delta m^2_{21}/10^{-5}$ eV^2	7.54	6.99−8.18
$\lvert\Delta m_{31}\rvert^2/10^{-3}$ eV^2	2.43 (NH) 2.38 (IH)	2.23−2.61 (NH) 2.19−2.56 (IH)
$\sin^2\theta_{12}$	0.308	0.259−0.359
$\sin^2\theta_{23}$	0.437 (NH) 0.455 (IH)	0.374−0.626 (NH) 0.380−0.641(IH)
$\sin^2\theta_{13}$	0.0234 (NH) 0.0240 (IH)	0.0176−0.0295 0.0178−0.0298
δ	1.39/ π (NH) 1.31/π (IH)	

surements on θ_{13} were carried out by the LBL accelerator based experiments MINOS [50] and T2K [52] and their results indicate its non-zero value. Precise measurements of θ_{13} were carried out in the short-base line (SBL) reactor neutrino experiments *viz.* Double Chooz: $\sin^2\theta_{13} \simeq 0.086 \pm 0.041$ (stat.) $\pm$ 0.030 (syst.) [45], and Daya Bay: $\sin^2\theta_{13} \simeq 0.092 \pm 0.016$ (stat.)$\pm$ 0.005 (syst.) [46] and RENO: $\sin^2\theta_{13} \simeq 0.113 \pm 0.013$ (stat.) $\pm$ 0.019 (syst.) [47]. The nonzero value of θ_{13} will help in discovering a possible CP violation in the lepton sector and matter effects in LBL oscillation experiments, which could allow one to identify the neutrino mass hierarchy *viz.* normal or inverted [68]. The phenomenon of neutrino oscillation in vacuum is insensitive to the sign of Δm^2, however matter effects (the MSW effect) on the 1 - 2 flavour mixing in the Sun have determined Δm^2_{21} to be positive-definite. On the other hand, the present experimental data are not yet able to determine the sign of Δm^2_{32}. There are two possible combinations of mass hierarchy as shown in Fig. 2.3. In the "normal hierarchy (NH)", the smallest mass-squared difference is between the two lightest eigenstates *i.e.* ($m_1 < m_2 < m_3$), whereas in the "inverted hierarchy (IH)" the smallest mass-squared difference is between the two heaviest *i.e.* ($m_3 < m_1 < m_2$) and almost degenerate eigenstates. Several global analyses have been carried out by various groups for estimating the neutrino oscillation parameters using data from various experiments [69–72]. The latest best-fit and 3 σ ranges are given in Table 2.1. It may be noted here, the CP-violating phase δ is only weakly constrained by global fits. For the NH case, the magnitude of PMNS matrix using the best-fit values of the mixing angles is given as

$$|U| \simeq \begin{pmatrix} 0.822 & 0.548 & 0.153 \\ 0.501 & 0.568 & 0.653 \\ 0.271 & 0.614 & 0.742 \end{pmatrix}. \tag{2.37}$$

However, the final parameters of the PMNS matrix, the CP-phase, δ, for 3 generation neutrinos is not yet known. The recent measurement of a nonzero value of θ_{13} provides us an opportunity to search for CP violation in lepton sector. There are several experiments which focus on the measurement of this phase and thus establish whether CP is violated in leptonic weak interactions or not. More importantly, the observation of CP-violation in the neutrino sector, through leptogenesis, may be a possible means of explaining the observed asymmetry between matter and antimatter [73, 74].

4 Sterile Neutrino

The study of neutrinos has moved beyond the SM of particle physics after the discovery of neutrino oscillations. The phenomenon of neutrino oscillations implies a nonzero value of neutrino mass. At present, most of the experimental data can be described by the 3-ν oscillation formalism. However, there exist some results which may not be be accommodated within this formalism, and suggest a new physics. It has been observed that the sum of masses of three active neutrinos is less than $\sim$ 1 eV. On the other hand, there are possible hints for the existence of one or more additional neutrinos with masses at the eV scale, which is not consistent with the well-established solar and atmospheric Δm^2 scales. This new particle is called a sterile neutrino as it does not interact with matter through any of the known fundamental interactions in the SM of particle physics. The name 'sterile' neutrino was suggested by B. Pontecorvo [57]. If sterile neutrinos are present, they may mix with the active flavour neutrinos. On the other hand, they will participate, like all matter and energy, through the gravitational interaction.

4.1 Experimental Evidence on Possible Existence of Sterile Neutrino

The evidence on the possible existence of sterile neutrinos from the various experimental measurements are described below.

LSND

The most significant indication of sterile neutrino with $\Delta m^2_{41} \sim 1$ eV^2 comes from the LSND experiment [75] which measured the appearance of $\bar{\nu}_e$ arising from the oscillation of $\bar{\nu}_\mu$s. The LSND was a $\pi^+ \rightarrow \mu^+$ decay-at-rest experiment produce $\bar{\nu}_\mu$, with source to detector distance $\sim$ 30 m and neutrinos having energy E_ν = 10 - 50 MeV. The liquid scintillator detector was used to identify the $\bar{\nu}_e$ events from a background of possible $\bar{\nu}_\mu$ events. The detection principle is based on IBD process, $\bar{\nu}_e + p \rightarrow e^+ + n$. It showed an excess of electron anti-neutrino events above the expected background with about 3.8 σ significance. The experimental results of solar neutrino measurements correspond to $\Delta m^2_{sol} \simeq 7.5 \times 10^{-5}$ eV^2 while atmospheric neutrino oscillations correspond to $\Delta m^2_{atm} \simeq 2.4 \times 10^{-3}$ eV^2. As the LSND result is not compatible with those from solar and atmospheric neutrino experiments a fourth neutrino, which needs to be sterile, is strongly suggested.

MiniBooNE

The MiniBooNE experiment has studied both $\nu_\mu \rightarrow \nu_e$ and $\bar{\nu}_\mu \rightarrow \bar{\nu}_e$ oscillation channels at a higher energy neutrino beam and longer baseline such that L/E is about the same as in the LSND experiment. In their experiment, a conventional pion beam $\pi^\pm \rightarrow \mu^\pm + \overset{(-)}{\nu}_\mu$ was used to study the anomaly observed by LSND experiment. For the neutrino mode *i.e.* $\nu_\mu \rightarrow \nu_e$ and at energy range 475 - 1250 MeV (the region which corresponds to the LSND event excess)[4], the observed number of events are consistent with no excess. The lack of excess above 475 MeV in the MiniBooNE $\nu_\mu \rightarrow \nu_e$ search resulted in an exclusion of the LSND 90 % CL allowed parameters at the 98 % CL. However, a 3.0 σ excess of ν_e events was observed at a lower energy, below 475 MeV, corresponding to a significantly different L/E than that of the LSND excess [76]. On the other hand, results from an analysis of $\bar{\nu}_e$ appearance data show an excess of 78.4 ± 28.5 events (2.8 σ) [77] in the energy range $200 < E_\nu < 1250$ MeV. At $\Delta m^2 \simeq 0.1$ to 1.0 eV^2 range, MiniBooNE found the result was consistent with the indication for the anti-neutrino oscillations and is not inconsistent with the evidence for antineutrino oscillations from LSND experiment.

[4]Under the assumption of CP conservation, which implies $\overset{(-)}{\nu}_\mu \rightarrow \overset{(-)}{\nu}_e$.

Reactor Neutrino

Recently, the reactor antineutrino flux has been reevaluated considering the thermal neutron induced fission of ^{235}U, ^{239}Pu, ^{241}Pu and ^{238}U [78, 79] and shows that there is an increase of ~ 3 % in the predicted flux. Based on these new antineutrino fluxes, a reanalysis was performed on the ratio of observed to predicted event rate for various published experiments at reactor to detector distances between about 10 m to 100 m. The ratio is decreased to 0.943 ± 0.023 from 0.976 ± 0.024, leading to a deviation from unity at 98.6 % CL, and is referred to as the "reactor antineutrino anomaly" [80]. This deficit suggests the existence of a sterile neutrino with $\Delta m^2 \sim 1$ eV^2 and $\sin^2 2\theta \sim 0.1$.

Gallex and SAGE

The radioactive source calibration experiments on electron neutrino disappearance have also observed similar anomalies. In the SAGE [81] and GALLEX [82] solar neutrino experiments, ^{51}Cr and ^{37}Ar radioactive sources are used for calibration of their detectors. The radioactive nuclei decay through electron capture and produce electron neutrinos, as follows

$$e^- + {}^{51}Cr \rightarrow {}^{51}V + \nu_e, \;\; \mathrm{E}_{\nu_e} : 0.747, 0.752, 0.427, \text{and } 0.432 \text{ MeV} \tag{2.38}$$

$$e^- + {}^{37}Ar \rightarrow {}^{37}Cl + \nu_e, \;\; \mathrm{E}_{\nu_e} : 0.811 \text{ and } 0.813 \text{ MeV} \tag{2.39}$$

It may be observed that neutrinos produced by these sources as given in Eq. 2.38 and Eq. 2.39 have a lower energy compared to the accelerator based LSND, MiniBooNE or the reactor based experiments. The ν_e interacts with ^{71}Ga (threshold energy correspond to E_ν^{th} = 233 keV) via the reaction as given in Eq. 2.30. The detector used in the GALLEX experiment has a radius, R_G = 1.9 m and height of H_G = 0.7 m whereas for the SAGE experiment, radius R_S = 5 m and height H_S = 1.5 m. They put their sources within the detector resulting in small propagation distances for neutrinos such that the L/E is similar to that in the LSND experiment. Hence, these detectors are able to measure a similar range of parameter space accessed by LSND. The measured event rate is ~ 2.8 σ smaller than the predicted rate and is known as the "Gallium anomaly". A statistical study on this anomalous deficit of electron neutrinos was carried out in Ref. [83] including the uncertainty of the detection cross section. The neutrino oscillation parameters obtained from the analysis are $\sin^2 2\theta \gtrsim 0.07$ and $\Delta m^2 \gtrsim 0.35\,\mathrm{eV}^2$ at 99 % CL.

Null Results

In addition, there are several other experiments which have searched for signals of sterile neutrino mixing with null results and have placed upper bounds on the mixing as a function of Δm^2 when analysed within the 3 + 1 neutrino oscillation formalism. The KARMEN [84] experiment, which is similar to the LSND experiment, and is based on the appearance channel, $\bar{\nu}_\mu \rightarrow \bar{\nu}_e$, did not show a signal at 90 % CL. It ruled out most of parameter space allowed by LSND. The NOMAD [85] experiment looked for ν_e in the appearance channel, $\nu_\mu \rightarrow \nu_e$, starting with the ν_μ beam at the CERN Super Proton Synchrotron (SPS). Evidence of oscillation was not found and their result excludes the LSND allowed oscillation parameters space for $\Delta m^2 \geq 10$ eV^2. Result from the ICARUS experiment [86] on the search for $\nu_\mu \rightarrow \nu_e$ anomalies is compatible with the absence of additional anomalous contributions. At 90 % and 99 % C.L., the oscillation probabilities are 3.4×10^-3 and 7.6×10^-3, respectively. The OPERA experiment [87] also looked for the appearance of ν_e from the oscillation of $\nu_\mu \rightarrow \nu_e$ which is located at the Gran Sasso Underground Laboratory. The OPERA experiment limits the allowed parameter space suggested by the results of the LSND and MiniBooNE experiments. At 90% C.L. and for large Δm^2_{new} values (>0.1 eV^2), the upper limit on $\sin^2 2\theta_{new}$ is about 7.2×10^{-3}. The SK experiment has searched for rapid oscillations due to sterile neutrinos using atmospheric neutrinos as the source. Their result did not show evidence of sterile neutrinos and limits on active-sterile neutrino mixing are given in Ref. [88]. The MINOS experiment has also searched for sterile neutrino oscillations through NC disappearance. Results based on their analysis did not show evidence for the depletion of NC events [89]. They put the constraint on the fraction of neutrinos which may transition to $\nu_s < 22$ % at the 90 % CL. However, results from the global analysis based on 3 + 1 neutrino oscillation theory, show tension between the allowed region from all appearance experiments and from all disappearance experiments in the plane of $\sin^2 2\theta_{\mu e}$ and Δm^2_{41}. There is a marginal overlap regions at above 99% CL around $\Delta m^2{}_{41} \approx 0.9\ eV^2$ and at 3σ around $\Delta m^2{}_{41} \approx 6\ eV^2$ [90].

The studies of active-sterile neutrino mixing are from a purely phenomenological point of view, without introducing a specific theoretical model. The presence of sterile neutrinos modifies the oscillation probabilities of active neutrinos in appearance and disappearance experiments. As they do not interact with the matter, their presence may be confirmed experimentally, only indirectly, by measuring the active flavours from their appearance or disappearance probabilities.

4.2 Oscillation Probability Using 3 + 1 Model

The sterile neutrino oscillation probabilities are based on the expansion of the 3 generation PMNS matrix to the 3 + 1 generation, "3" stands for active and "1" for sterile neutrinos, respectively. For this, the unitary mixing matrix is given as

$$\begin{pmatrix} \nu_e \\ \nu_\mu \\ \nu_\tau \\ \nu_s \end{pmatrix} = \begin{pmatrix} U_{e1} & U_{e2} & U_{e3} & U_{e4} \\ U_{\mu 1} & U_{\mu 2} & U_{\mu 3} & U_{\mu 4} \\ U_{\tau 1} & U_{\tau 2} & U_{\tau 3} & U_{\tau 4} \\ U_{s1} & U_{s2} & U_{s3} & U_{s4} \end{pmatrix} \begin{pmatrix} \nu_1 \\ \nu_2 \\ \nu_3 \\ \nu_4 \end{pmatrix}. \tag{2.40}$$

In Eq. 2.40, elements of the mixing matrix describe the coupling between the flavour state and mass state, that can mix with the three active flavours. It may be observed from Eq. 2.40 that the matrix U has seven new elements, four of which (U_{s1}, U_{s2}, U_{s3}, U_{s4}) may not be directly constrained by experiment due to the non-interacting nature of the sterile neutrino. Assuming zero CP phase in the lepton sector for simplicity, the convention on the order of rotation for the mixing matrix was considered from Ref. [91] and given by,

$$U = R(\theta_{34})R(\theta_{24})R(\theta_{23})R(\theta_{14})R(\theta_{13})R(\theta_{12}), \tag{2.41}$$

where $R(\theta_{ij})$ are the rotation matrices and θ_{ij} are the mixing angles with $i, j = 1, 2, 3, 4$. Matrices which constitute to Eq. 2.40 are

$$U = \begin{pmatrix} c_{14} & 0 & 0 & s_{14} \\ 0 & 1 & 0 & 0 \\ 0 & 0 & 1 & 0 \\ -s_{14} & 0 & 0 & c_{14} \end{pmatrix} \times \begin{pmatrix} c_{13} & 0 & s_{13} & 0 \\ 0 & 1 & 0 & 0 \\ -s_{13} & 0 & c_{13} & 0 \\ 0 & 0 & 0 & 1 \end{pmatrix} \times \begin{pmatrix} c_{12} & s_{12} & 0 & 0 \\ -s_{12} & c_{12} & 0 & 0 \\ 0 & 0 & 1 & 0 \\ 0 & 0 & 0 & 1 \end{pmatrix} \times$$

$$\begin{pmatrix} 1 & 0 & 0 & 0 \\ 0 & 1 & 0 & 0 \\ 0 & 0 & c_{34} & s_{34} \\ 0 & 0 & -s_{34} & c_{34} \end{pmatrix} \times \begin{pmatrix} 1 & 0 & 0 & 0 \\ 0 & c_{24} & 0 & s_{24} \\ 0 & -s_{24} & 0 & c_{24} \\ 0 & 0 & 0 & 1 \end{pmatrix} \times \begin{pmatrix} 1 & 0 & 0 & 0 \\ 0 & c_{23} & s_{23} & 0 \\ 0 & -s_{23} & c_{23} & 0 \\ 0 & 0 & 0 & 1 \end{pmatrix}. \tag{2.42}$$

The individual elements of the final U matrix are as follows,

$$\begin{cases} U_{e1} & = c_{12}c_{13}c_{14} \\ U_{e2} & = s_{12}c_{13}c_{14} \\ U_{e3} & = s_{13}c_{14} \\ U_{e4} & = s_{14} \end{cases}$$

$$\begin{cases} U_{\mu 1} & = -s_{12}c_{24}c_{23} - s_{13}c_{12}c_{24}s_{23} - s_{14}c_{13}c_{12}s_{34}c_{24} \\ U_{\mu 2} & = c_{12}c_{24}c_{23} - s_{13}s_{12}c_{24}s_{23} - s_{14}c_{13}s_{12}s_{24} \\ U_{\mu 3} & = c_{13}c_{24}s_{23} - s_{14}s_{13}s_{24} \\ U_{\mu 4} & = c_{14}s_{24} \end{cases}$$

$$\begin{cases} U_{\tau 1} & = s_{12}(s_{34}s_{24}c_{23} + s_{23}c_{34}) - s_{13}c_{12}(-s_{34}s_{24}s_{23} + c_{34}c_{23}) - s_{14}c_{13}c_{12}s_{34}c_{24} \\ U_{\tau 2} & = c_{12}(s_{34}s_{24}c_{23} + s_{23}c_{34}) - s_{13}s_{12}(-s_{34}s_{24}s_{23} + c_{34}c_{23}) - s_{14}c_{13}s_{12}s_{34}c_{24} \\ U_{\tau 3} & = c_{13}(-s_{34}s_{24}s_{23} + c_{34}c_{23}) - s_{14}s_{13}s_{34}c_{24} \\ U_{\tau 4} & = c_{14}s_{34}c_{24} \end{cases} \tag{2.43}$$

$$\begin{cases} U_{s1} & = -s_{12}(-s_{24}c_{34}c_{23} + s_{34}s_{23}) + s_{13}c_{12}(s_{24}c_{34}s_{23} + s_{34}c_{23}) - s_{14}c_{13}c_{12}c_{34}c_{24} \\ U_{s2} & = c_{12}(-s_{24}c_{34}c_{23} + s_{34}s_{23}) + s_{13}s_{12}(s_{24}c_{34}s_{23} + s_{34}c_{23}) - s_{14}c_{13}s_{12}c_{34}c_{24} \\ U_{s3} & = -c_{13}(s_{24}s_{34}s_{23} + s_{34}c_{23}) - s_{14}s_{13}c_{34}c_{24} \\ U_{s4} & = c_{14}c_{24}c_{34}. \end{cases}$$

Using the above definition, neutrino flavour change can be described as a function of the mixing elements and neutrino masses in terms of neutrino oscillation probability

$$\begin{aligned} P_{\alpha\beta} = \delta_{\alpha\beta} - 4\sum_{i>j} Re(U_{\alpha i}U^*_{\beta i}U^*_{\alpha j}U_{\beta j}) sin^2\frac{\Delta m^2_{ji}L}{4E} \\ + 2\sum_{i>j} Im(U_{\alpha i}U^*_{\beta i}U^*_{\alpha j}U_{\beta j}) sin\frac{\Delta m^2_{ji}L}{2E}, \end{aligned} \tag{2.44}$$

where α, β = e, μ, τ, s; $\Delta m^2_{ji}= m^2_j - m^2_i$ at $j > i$ [5]. Additional parameters which describe the oscillation in 3 + 1 formalism are three mixing angles (θ_{14}, θ_{24}, θ_{34}), and one new

[5]It may also noted that in '3 + 1' generation, 3 active neutrinos have very small mass compared to the sterile neutrino *i.e.* $m_4 >> m_{1,\,2,\,3}$

mass-squared difference, which we choose to be $\Delta m_{41}^2 = m_4^2 - m_1^2$. It is to be noted that the other two extra mass-squared differences, Δm_{42}^2 and Δm_{43}^2, are not independent and can be expressed as $\Delta m_{42}^2 = \Delta m_{41}^2 - \Delta m_{21}^2$ and $\Delta m_{43}^2 = \Delta m_{41}^2 - \Delta m_{31}^2$. It may be noted here, for the sterile neutrino with mass of about 1 eV, to observe the first oscillation minimum or maximum, it requires a few MeV to few GeV neutrinos for a distance of few meters to a few km. On the other hand, at squared mass difference of Δm_{sol}^2 or Δm_{atm}^2, these baselines are relatively short for observing the oscillation due to solar or atmospheric neutrinos. Therefore, experiments which are sensitive to the sterile neutrino oscillations are referred as also SBL oscillation experiments. Then, at the SBL approximation, $|\frac{\Delta m_{ji}^2 L}{4E}| \ll 1$ $(i, j = 1, 2, 3)$, the corresponding oscillation probability for a 3 + 1 model is reduced to "1 + 1" model. As the CP violating phases in 'U' is zero then the last term in Eq. 2.44 will be also zero. Hence, the corresponding disappearance probability is as follows,

$$P\left(\nu_\alpha \to \nu_\alpha\right) \simeq 1 - 4\left(1 - U_{\alpha 4}\right)|U_{\alpha 4}|^2 sin^2\left(\frac{1.27\Delta m_{41}^2 L}{E}\right), \tag{2.45}$$

where the assumption is based on $\Delta m_{41}^2 \simeq \Delta m_{42}^2 \simeq \Delta m_{43}^2$. Similarly the appearance probability is given as,

$$P\left(\nu_\alpha \to \nu_\beta\right) \simeq 4|U_{\alpha 4}|^2|U_{\beta 4}|^2 sin^2\left(\frac{1.27\Delta m_{41}^2 L}{E}\right). \tag{2.46}$$

4.3 Matter Effect on Sterile Neutrino Oscillation

In Section 2, we have already discussed that the evolution of the amplitude of the neutrino flavour eigenstate in matter is governed by the MSW effect. The effective mass matrix in matter then changes to

$$M_F^2 = UM^{(3+1)}U^\dagger + A, \tag{2.47}$$

where

$$M^{(3+1)} = diag(m_1^2, m_2^2, m_3^2, m_4^2), \tag{2.48}$$

$$A = diag(A_{CC}, 0, 0, A_{NC}), \tag{2.49}$$

where

$$A_{CC} = \pm 2\sqrt{2} G_F \rho N_A Y_e E, \tag{2.50}$$

$$A_{NC} = \pm\sqrt{2} G_F \rho N_A (1 - Y_e) E. \tag{2.51}$$

Here, A_{CC} and A_{NC} are the matter induced weak CC and NC potentials, respectively. The '+' and the '−' sign correspond for the neutrinos and antineutrinos, respectively. Only ν_e has CC interaction with electrons and NC interaction with electrons and nucleons, whereas ν_μ and ν_τ have only NC interaction and sterile neutrinos have no weak interactions.

4.3.1 Constraint on Active-Sterile Neutrinos Mixing Parameter from Global Analysis

The search for sterile neutrinos has been performed by several experiments considering either the appearance or disappearance oscillation channel of neutrinos over a wide range of energies and baselines. Some of the experimental data provide positive results on the presence of sterile neutrinos and other experiments have null results. It has also seen that the limits on oscillation parameters provided by various experiments are not compatible with each other. Nevertheless, combining the experimental data from various experiments searching for sterile neutrinos, a global analysis has been carried out by two groups and their results on the active-sterile neutrino mixing are presented in Ref. [90] and in [92]. The authors of Ref. [90] have analyzed their data considering one or two sterile neutrinos with mass-squared differences $\sim$ eV^2 within the 3 + 1, 3 + 2 and 1 + 3 + 1 models. Here, we list the best fit values of the parameters $|U_{e4}|^2$, $|U_{\mu4}|^2$ and Δm^2_{41}, characterizing the active-sterile neutrino (antineutrino) oscillations in the 3 + 1 scheme:

$$|U_{e4}|^2 = 0.0225,\ |U_{\mu4}|^2 = 0.0289,\ \Delta m^2_{41} = 0.93\ \text{eV}^2. \tag{2.52}$$

The authors of Ref. [92] also perform their analysis considering 3 + 1, 3 + 2 and 3 + 1 + 1 neutrino mixing scheme. We have only considered their results in the 3 + 1 scheme, where in contrast to Ref. [90] only the MiniBooNE data above 475 MeV is used. The best fit values of $|U_{e4}|^2$, $|U_{\mu4}|^2$ and Δm^2_{41} obtained from their analysis are

$$|U_{e4}|^2 = 0.03,\ |U_{\mu4}|^2 = 0.013,\ \Delta m^2_{41} = 1.60\ \text{eV}^2. \tag{2.53}$$

4.4 Cosmology

Neutrinos are produced in copious amounts in the early Universe, and are still present as a cosmic neutrino background. Cosmological measurements are sufficiently precise to constrain the sum of the neutrino masses and may also provide information on the existence of sterile neutrinos. A non-zero mass sterile neutrino could impact the cosmic microwave background (CMB) power spectrum and modify large scale structure formation. The existence of sterile neutrinos which have been thermalised in the early Universe may contribute to the number of relativistic degrees of freedom (effective number of neutrino species). The radiation energy density contribution from an effective number of neutrino species, N_{eff} [93] is given by

$$\rho_\nu = N_{eff}\frac{7\pi^2}{120}T_\nu^4, \tag{2.54}$$

where ρ_ν is the total neutrino energy density in the radiation domination era, T_ν is the neutrino temperature related with photon temperature, T_γ, given as

$$T_\nu = \left(\frac{4}{11}\right)^{1/3} T_\gamma, \tag{2.55}$$

after e^+e^- annihilation.The Planck Collaboration has provided the upper limit on the sum of the neutrino masses [94] $\sum m_\nu \leq 0.66$ eV at 95 % CL and with addition of data on baryon acoustic oscillation (BAO) further lowers the limit to $\sum m_\nu \leq 0.23$ eV at 95 % CL. The cosmological bounds from cosmic microwave background (CMB) data [94] are $N_{eff} < 3.91$ and $m^{eff}_{\nu,sterile} < 0.59$ eV at 95 % CL.

4.5 Sterile Neutrino Search in Future

There is no preferred theoretical model or framework that has emerged so far from the above mentioned experimental results to confirm the presence of sterile neutrino. There have been several attempts to interpret those results in terms of 3 + N neutrino oscillation models involving three active neutrinos and N additional sterile neutrinos [95, 96]. The possible existence of sterile neutrinos is very interesting because they are new particles which could give us valuable information on the physics beyond the SM. The hypothesis of active-sterile neutrinos mixing at eV scale masses will be tested by several experiments using accelerator- and reactor-based artificial sources of neutrinos. In the MiniBooNE experiment, in particular, the measured signal in the neutrino mode, does not quite agree with expected sterile neutrino signal. The main disadvantage of their detector was that it cannot discriminate an e^-/e^+ and a gamma ray which is a potential background. Therefore, experimental efforts are going on using the MicroBooNE [97] large liquid argon (LAr) TPC (Time Projection Time Chamber) detector to test the MiniBooNE signal.

To confirm the reactor neutrino anomaly due to presence of eV^2 sterile neutrino oscillation, there are several projects and proposals to measure a spectral distortion in the antineutrino rate which varies with distance from the reactor core. So it is important to put detectors at a few tens of meters from a compact reactor cores which is preferable in comparison with larger commercial reactors to prevent washing out the hypothetical sterile oscillation pattern. A high segmented plastic scintillator based detector DANSS [98] was proposed to be installed under the industrial 3 GWth reactor of the Kalinin Nuclear Power Plant (KNPP). The PROSPECT [99] collaboration proposes to address anomalies in neutrino physics by precisely measuring the antineutrino spectrum produced from a reactor with a core highly enriched in ^{235}U. The STEREO [100, 101] detector is in construction at ILL which will measure precisely the antineutrino spectrum and flux at very short distance (9 - 11 m). The detector will be able to confirm or refute the hypothesis of a light sterile neutrino.

To test the gallium anomaly, there are proposals to use kCi to MCi radio-active neutrino sources *viz.* ^{51}Cr and ^{144}Ce - ^{144}Pr. The new Gallium experiment BEST at Baksan was proposed to thoroughly explore the gallium anomaly using an artificial compact 3 MCi ^{51}Cr source. A list of experiments set up to search for sterile neutrinos using radioactive sources and accelerators is given in Refs. [102, 103].

There have been studies carried out to see the impact of eV^2 scale sterile neutrino mixing on measurements of atmospheric neutrinos. At this mass scale, the disappearance of atmospheric ν_μ in the few tens of GeV to TeV energy range can be enhanced due to the matter effects in the Earth's core [104, 105]. Neutrinos with energies $\sim$ TeV have already been observed by the IceCube experiment [106–108]. Such an experiment can place bounds on a possible active-sterile neutrino mixing using the zenith angle and energy dependent upward-going neutrinos. The downward-going atmospheric ν_μ and $\bar{\nu}_\mu$ fluxes may be significantly altered due to the presence of eV^2-scale active-sterile oscillations [109]. So both the upward-going and the downward-going neutrinos may be used to explore the sterile neutrino mixing sensitivity. A large magnetized iron detector such as the proposed iron calorimeter (ICAL) at the India-based Neutrino Observatory (INO) will also look for signatures of sterile neutrino mixing in atmospheric neutrinos.

5 Further Challenges

There are several theoretical and experimental studies which have been carried out on neutrinos. The study of neutrino oscillation provides information on neutrino mixing parameters while confirming that the neutrino has non-zero mass. Some other experimental results place upper limits on an absolute mass of the neutrino, others give hints of the existence of the sterile neutrinos *etc.*. Nonetheless it is fair to say that at present day our knowledge and understanding of neutrinos is rather limited and there are many open questions, some of which are listed below:

- Is there CP violation in the lepton sector, and what is the value of δ_{CP}?
- Does the neutrino mass spectrum follow normal or inverted hierarchy? Future experiments using atmospheric, accelerator and reactor neutrino experiments may solve this problem.
- Is the mixing angle θ_{23} exactly maximal or are there deviations?
- Are there sterile neutrinos? This problem may be solved by various SBL reactor, radioactive source and accelerator-based neutrino oscillation experiments.
- What is the absolute mass of the neutrino?
- Is the neutrino a Dirac or a Majorana particle? There are several ongoing efforts to find out the nature of the neutrino using neutrinoless double β-decay. Such experiments will also give the effective Majorana mass of the neutrino.

In addition there are also further challenges in theoretical aspects *viz.*

- why is $m_\nu \ll m_{u,d,e}$?
- Why is neutrino mixing so different from quark mixing (Neutrino mixing is larger than quark mixing)?
- From experimental measurements, we have $\frac{\Delta m^2_{sol}}{\Delta m^2_{atm}} \ll 1$, but $\frac{\Delta m^2_{sol}}{\Delta m^2_{atm}} \gg \left(\frac{m_\mu}{m_\tau}\right)^2$. why?

To resolve these questions and shape the future direction of particle physics, several new experiments worldwide have been proposed and some are already under construction.

Chapter 3

Design of the ICAL Magnet

In this chapter, the design of the iron calorimeter (ICAL) magnet for the proposed India-based Neutrino Observatory (INO) will be described. The motivation is to find out the configuration which has the desired uniformity of as high a magnetic field as possible at the lowest power dissipation in the coils. At first, the ICAL detector and its role in the measurement of atmospheric neutrinos is described in detail. In subsequent sections, the electromagnetic simulation technique which has been used to obtain the magnetic field distribution in the ICAL magnet is discussed. The results obtained from the simulation for the standard base-line design as well as for the configurations that deviate from the standard one are highlighted.

1 ICAL detector and its importance at INO

The ICAL detector at the INO is designed to measure atmospheric neutrinos. It will be located in a cavern, as shown in Fig. 3.1, with a minimum all round rock cover of 1 km in order to reduce the cosmic ray background. The magnetized ICAL detector can be configured in one of the many possible geometries. For example, it could be a toroid (with or without iron), a layered cylindrical shape oriented in suitable fashion with a central conductor or a layered rectangular shaped one with embedded coils. The shape and dimensions of the ICAL detector are based on the cavern dimensions of about 132 m (length) $\times$ 26 m (width) $\times$ 32 m (height). The latter two dimensions are the maximum possible for a self supporting cavern in a monolithic charnockite rock. The ICAL detector has a rectangular shape with dimension of $\sim$ 49 m $\times$ 16 m $\times$ 15 m as shown in Fig. 3.2.

To build such a massive detector as a single entity would be difficult, if not impractical. Hence, a modular approach has been adopted and there are three modules with each module having a mass of ~ 17 kton and size of ~ 16 m × 16 m × 14.5 m. There is a gap of about 20 cm between adjacent modules which may be useful from the point of view of mechanical assembly and a provision for visual inspection. The details of the ICAL magnet are given in Table 3.1. The design of the ICAL magnet is similar to that in the MONOLITH proposal [110].

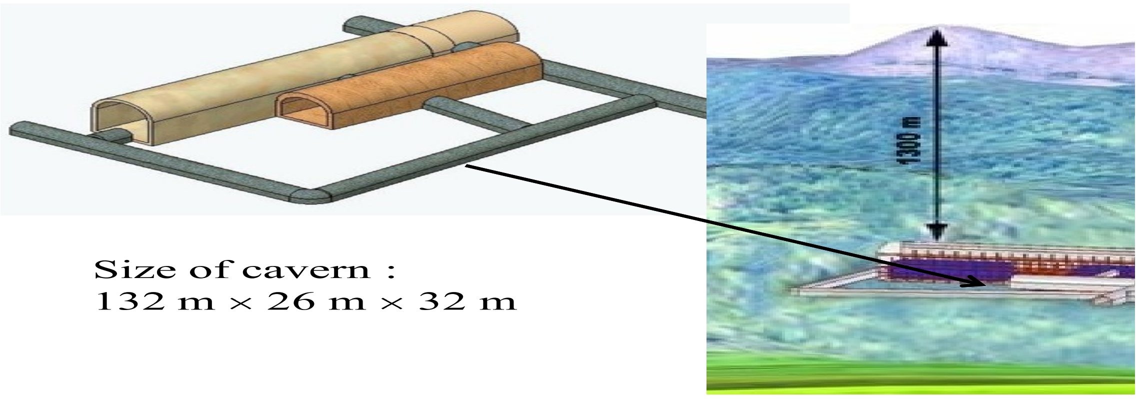

Figure 3.1: Schematic of the ICAL detector at the INO surrounded by rock.

The atmospheric neutrino flux varies with energy ~ $E^{-2.7}$ whereas the interaction cross section varies linearly with energy ($\sigma \sim 10^{-42}$ $(m^2) \times E/(GeV)$) and both of them cannot be changed. An acceptable event rate may be obtained either by increasing the mass of detector or counting for a longer time. Hence, the mass of the ICAL detector has been decided on the basis of getting a reasonable number of events within a specified time. To address the physics goal, it has been proposed to begin with a detector of mass about 51 kton, which subsequently may be enlarged to double the size in stages. A large mass and high density are necessary to provide the necessary number of neutrino-nucleon interactions. The baseline ICAL magnet configuration for each of the three modules consists of 151 layers of low carbon steel. The thickness of each iron layer has been decided after considering various factors. For example, at a given cavern height and at fixed detector thickness, a smaller iron plate thickness results in a lower iron mass implying a smaller neutrino event rate. Also, a larger plate thickness, results in an increase in the multiple Coulomb scattering of the neutrino induced muon and leads to a worsening in the momentum resolution. A nominal thickness of 56 mm has been chosen for the iron plate. After taking into account the height needed for the supporting base pillars and

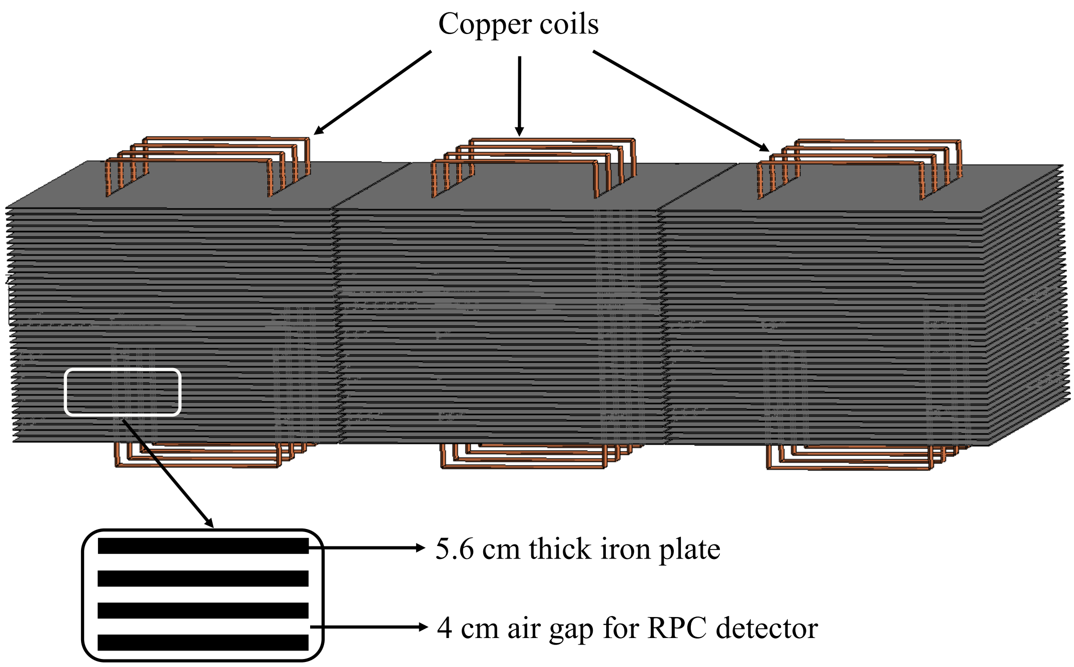

Figure 3.2: The three modules of the ICAL magnet at the INO.

the crane headroom one can accommodate about 151 steel layers which are adequate to have a reasonable efficiency for the muons in the energy range of 1 - 20 GeV. The steel layers are alternated with gaps of 40 mm in which will be placed active gas detectors of the resistive plate chamber (RPC) type as shown in Fig. 3.3. The RPC detector helps to track the charged particles produced in a neutrino interaction with the nucleons of iron. The position information will be obtained from the mutually perpendicular X, Y-pick-up strips (golden yellow color shown in Fig. 3.3) of the RPC detectors at ~ 0.86 cm spatial resolution and the layer number will provide the Z-coordinate. The detector has a very good timing resolution (σ_t) ~ 1 ns [111], which helps to distinguish the upward-going from downward-going neutrino events. Each iron layer has a dimension of 16 m × 16 m × 0.056 m assembled from 2 m × 4 m × 0.056 m tiles. The gap between any two adjacent tiles is ~ 2 mm which is necessary in order to assemble the magnet given the plate machining and locating pin and hole tolerances. Copper coils carrying DC current having a height (H) of ~ 15 m and width (W) ~ 8 m are used to magnetize the low carbon steel plates. The cross-section of the copper conductor used in fabricating the coils is 30 mm × 30 mm with a 17 mm diameter hole through which demineralized chilled water will flow to limit the temperature rise to ~ 4° C in the conductor. The calorimeter will be magnetized, with a uniform magnetic field of ~ 1 - 1.5 Tesla (T), to distinguish the μ^- and the μ^+ events from the opposite curvature of their tracks.

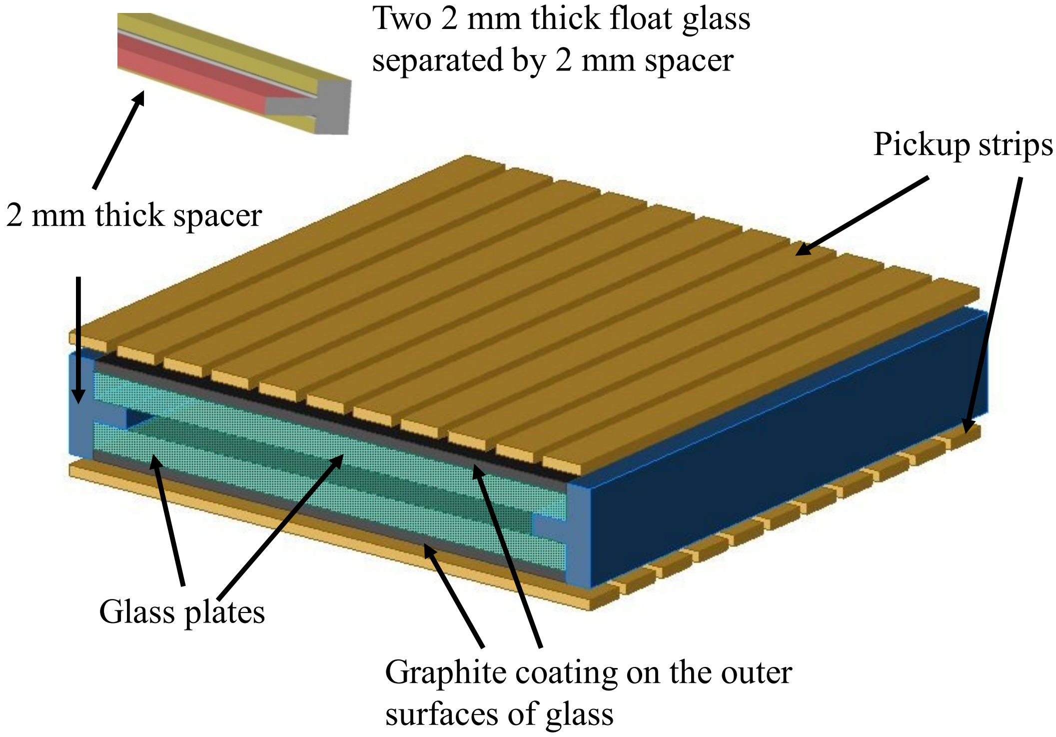

Figure 3.3: Schematic of the RPC detector.

A precise measurement of the oscillation parameters depends on several detector properties like, low energy threshold for measuring low-energy neutrinos (*e.g.* solar neutrinos), good angular resolution for reconstructing the direction of incoming neutrinos interacting with the detector (*e.g.* in case of atmospheric neutrinos, it is important to estimate the source to detector distance), good particle and charge identification ability which help to reduce the systematic uncertainties, good energy and timing resolution. However, it is not possible for a detector to satisfy all these requirements. Detectors are designed and constructed depending upon the type(s) of neutrino(s) to be measured, its energy range and the physics goal. The neutrino is an electrically neutral particle and therefore cannot be detected directly. It is detected by measuring the signals from secondary charged particles produced when it interacts with the detector material. In NC interactions, the neutrino does not change to a charged lepton and remains a neutrino. However, it transfers energy and momentum to the target and the transferred energy-momentum is measured. To detect the lepton produced in the CC interaction, such as the electron or muon, several detectors *viz.* water Cherenkov, liquid scintillator and magnetized iron calorimeters (such as MINOS) have been used.

Table 3.1: Details of the ICAL magnet.

ICAL magnet	
Mass of ICAL magnet	~51 kton
No. of modules	3
Module dimension	16 m × 16 m × 14.5 m
Detector dimension with coils	49 m × 16 m × 15 m
No. of iron layers	151
Dimension of each iron layer	16 m × 16 m × 0.056 m
Dimension of tiles to fill each layer	4 m × 2 m × 0.056 m
Gap between tiles	2 mm
Gap for RPC detectors	40 mm
No. of coils	4
No. of copper turns per coil	30
Copper turns cross section	30 mm × 30 mm with 17 mm Φ hole for chilled water flow
Magnetic field	1.5 T

When a charged particle travels faster than the speed of light in a refractive medium, such as water, it produces a cone of Cherenkov light and is the basis of Cherenkov detectors. The cone angle depends on the velocity of the particle and the refractive index of the medium. The optical sensors (such as the PMT) are used to measure the conical hit pattern. From the hit pattern, the incoming direction and energy (summing over PMT light) of the particle is reconstructed while the shape of the ring determines the type of lepton. The limitation of the Cherenkov method is that it is insensitive to the sign of the lepton charge.

In a scintillator detector, the energy deposited by a passing charged particle is converted to light, with a characteristic spectrum. Due to the isotropic emission of scintillation light, it is not possible to reconstruct the incoming direction of the particle. The main advantage of this type of detector is the low energy threshold (few hundred of keV for neutrinos) unlike the much higher energy threshold of the water Cherenkov detectors.

The tracking detectors are used to detect high energy neutrino induced particles. Such detectors are made up of active layers separated by passive layers. For example, in the ICAL detector at the INO, the passive iron layers stop particles quickly due to their high density. The active layers, comprising of RPC detectors, perform the actual detection. In the tracking detector, the energy of the particle may be measured from the track length. In case of a magnetized tracking detector the energy can also be measured from the curvature. The main advantage of a magnetized tracking detector is the charge identification ability. This type of detector is suitable for high energy muon neutrinos, as in a CC interaction a muon is produced. The minimum ionizing muon travels a long distance, produces a clean track and is suited for very good reconstruction of its energy-momentum. The ICAL is not a good detector for electrons, and hence for electron neutrinos, as they produce electromagnetic showers which undergo significant absorption in the iron.

The probability for the oscillation of neutrinos from one flavor to another depends on the mixing angle, energy and the source to detector distance which is estimated from their incoming direction. In order to measure the oscillation parameters more precisely, it is important that the neutrino energy and its incoming direction be accurately measured for each event. In case of atmospheric neutrinos, it is also necessary to establish the flight direction (up vs. down) for estimating the distance traversed by the neutrino with the necessary accuracy. In a tracking detector, the incoming direction of neutrinos may be determined from the slope of the track or from the measurement of timing in the successive detector layers. The ICAL detector has an ability to measure both these quantities. To measure the energy of neutrinos, it is crucial to measure the energy of leptons and hadrons produced in the interaction of neutrinos with the detector medium. The sum of their energies gives the total energy of the detected neutrino. It is very difficult to measure the energy of individual hadrons from the shower they produce. However, the hit multiplicity of charged particles distinct from the muon track may be used to measure the total energy of individual hadrons. The precise measurement of neutrino energy also depends on the accurate measurement of muon energy. The principle of the muon energy measurement in a magnetized tracking detector has been discussed earlier. The momentum measurement of muons depends on the strength of the magnetic field and its uniformity. In the following sections, the design of the ICAL magnet and its field profile for several configurations will be described.

2 Production of strong and uniform magnetic field

A uniform and high strength magnetic field can be produced in many ways using, for example, Helmholtz coils, a solenoid, permanent magnets, a room temperature electromagnet or a superconducting magnet. The magnetic field strength of an electromagnet depends on Ampere-turns of the current carrying coils and the magnetic permeability of the material used. The uniformity of the magnetic field depends on the arrangement of coils [112, 113], the tiling geometry of each layer and the homogeneity of the (ferro) magnetic material. To produce a strong magnetic field using the Helmholtz coils or solenoid, it is preferable to increase the number of turns rather than to increase the current. Even though the magnetic field (H) is proportional to current (I), the heat developed in the coil is proportional to I^2R, where R is its resistance. So increasing the number of turns and keeping the Ampere-turns constant, both H and R increase but the amount of heat production is reduced. Let us consider the case, doubling the current leads double H, and quadruples the heat. In the laboratory, a magnetic field of ~ 0.1 T may be produced using only coils (from conventional solenoid) whereas a superconducting solenoid may produce about 20 T. A uniform magnetic field can be obtained using the solenoid, if its length is more than about five times its diameter and in this configuration the field at the center of the solenoid is about 2 % larger than at its edge (in a finite size solenoid, the magnetic field at the edge is half of its mid value). While using a DC magnetic field larger than about 0.1 T with an electromagnet, it is usually necessary to cool the current carrying coils. This can be done in several ways, such as by blowing air over the solenoid with a fan, by submerging the solenoid in a chilled liquid, usually water but possibly liquid nitrogen, by winding the turns on a water-cooled tube, or by forming the winding from copper tubing so that it can carry both electric current and cooling water. On the other hand, permanent magnets, independent of coils, are used for high magnetic field strength applications. A high quality rare-earth permanent magnet may be used to produce a maximum field of about 2 T, but it is also quite expensive for a large volume application. In addition, the brittleness of a permanent magnet may put a constraint on building such a huge mass detector. Finally the magnetic field in an electromagnet can be easily reversed or changed by suitably changing the current in the energizing coil, whereas for a large setup using permanent magnets this is almost impossible.

In the laboratory, apart from conventional solenoids, electromagnets are used to produce magnetic fields up to about 2 T. An electromagnet consists essentially of an iron "core", enclosed with coils of wire carrying a DC current. Due to the iron, the magnetic induction (B-field) is a sum of the H-field, proportional to the current, and magnetization (M) of the iron. There are several shapes that an electromagnet can have *viz.* C-core, H-core electromagnets which are used to produce a strong and homogeneous B-field. Almost all commonly used electromagnets have iron yokes and poles because the magnetization of the iron magnifies a thousand-fold the magnetic field produced by the energizing coils. Here use is made of the B-field outside, rather than inside, of the magnet. The ICAL detector has at its heart a large electromagnet and the challenge here is not only to generate a magnetic field, B, of adequate uniformity but also of the required strength of ∼ 1 T in the entire volume of the 51 ktons of steel. So the size or extent of steel over which this field is required is challenging from the point of view of fabrication and installation in the limited space of the cavern. The estimation of Ampere-turns for the required B-field and its distribution in 16 m × 16 m are carried out for several configurations and conditions in the subsequent sections.

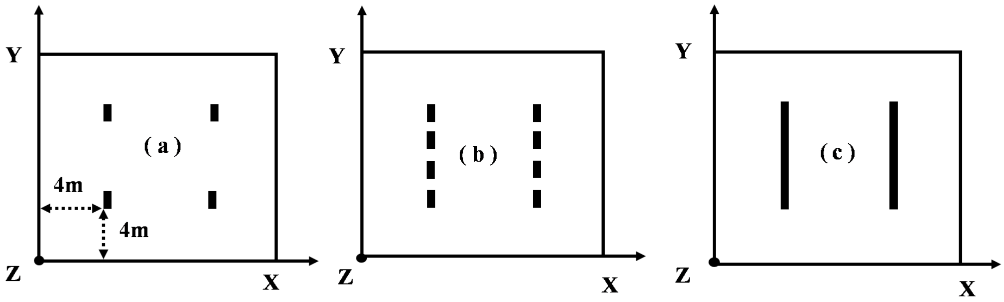

Figure 3.4: Schematic of iron plates with base of 16 m × 16 m having different slot configurations. Filled rectangular boxes show the slots through which copper coil pass to energize the magnet.

3 Electromagnetic simulation of the INO ICAL magnet

The magnetic field in a region is estimated using Maxwell's equations,

$$\vec{\nabla} \times \vec{H} = \vec{J} \tag{3.1}$$

$$\vec{\nabla} \cdot \vec{B} = 0, \tag{3.2}$$

where the H-field is produced due to the current source $\vec{J}$ (free current). In presence of ferromagnetic material,

$$\vec{B} = \mu_0 \mu_r \vec{H} = \mu_0(\vec{H} + \vec{M}), \tag{3.3}$$

where μ_0 is the magnetic permeability in free space, μ_r is the relative magnetic permeability of the ferromagnetic material ($\mu_r = 1 + \chi,\ \chi = \frac{M}{H}$), M is the magnetization of the ferromagnetic material. The $\vec{B}$-field related with magnetic vector potential $\vec{A}$ is given as

$$\vec{B} = \vec{\nabla} \times \vec{A}. \tag{3.4}$$

In an isotropic material, Eq. 3.1 can be expressed as

$$\vec{\nabla} \times \left(\frac{1}{\mu_0 \mu_r} \vec{\nabla} \times \vec{A}\right) = \vec{J}. \tag{3.5}$$

Applying the Coulomb gauge condition $\vec{\nabla} \cdot \vec{A} = 0$, and rewriting Eq. 3.5 as,

$$\nabla^2 A = -\mu J, \tag{3.6}$$

where $\mu = \mu_0\, \mu_r$ and Eq. 3.6 has been solved to determine $\vec{A}$. Both Dirichlet and Neumann boundary conditions are used in the simulations. In Dirichlet type of boundary condition, A, is explicitly defined on the boundary, *e.g.* $A = 0$ such that it keeps magnetic flux from crossing the boundary. On the other hand, Neumann boundary condition *i.e.* $\frac{\partial A}{\partial n} = 0$, is defined along a boundary to ensure the flux crosses the boundary at exactly 90° with respect to the boundary. In the magnetostatic case, both tangential and normal components of the magnetic field are continuous across the boundary.

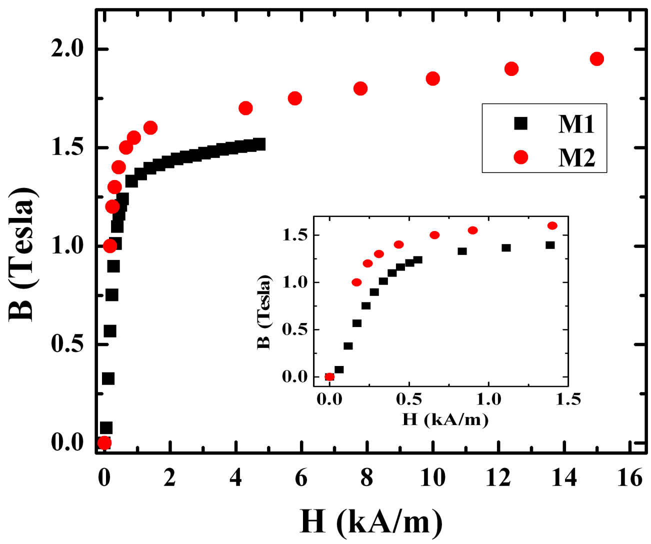

Figure 3.5: B-H profiles of soft magnetic materials M1 and M2.

The 3D electromagnetic simulations are carried out for studying the B-field distribution and its uniformity in iron using the Magnet software (Magnet 6.26 from Infolytica, Canada) [114]. The finite element software uses tetrahedral meshing to get the solution in the region of interest. The H-field versus B-field data for two different soft magnetic materials M1 and M2 [115], as shown in Fig. 3.5, are used in the electromagnetic simulation of the ICAL magnet. It shows that the material M2 is magnetically softer than M1 *viz.*

for a given B-field, M2 requires a smaller H-field than M1. The insert in Fig. 3.5 shows the blown up part of the B-H curve at low H-field. The softness of magnetic properties depends on the chemical composition with the carbon content being crucial. The chemical composition of each material is given in Table 3.2. The procedure followed for B-H profile measurement of soft magnetic material is described below.

Table 3.2: Chemical compositions of soft magnetic materials M1 and M2.

Chemical compositions									
Sample	C(%)	Mn(%)	Si(%)	P(%)	S(%)	Cr(%)	Ni(%)	Cu(%)	Fe(%)
M1	0.054	0.09	-	0.009	0.01	-	-	-	balance
M2	0.03	0.18	0.05	0.012	0.025	0.05	0.08	0.06	balance

3.1 BH-loop measurement

The B-H properties of the ICAL magnet are obtained by measuring the BH-loop of the low carbon steel using a hysteresis loop tracer. The measurement has been carried out using a toroidal sample which has primary and secondary turns. The main advantage of using a toroid of circular cross section is that it has no sharp corners so that the magnetic field changes smoothly as one moves from the inner radius to the outer. Then the H-field in a toroid is due to an actual applied current. The magnetic field in a toroid is inversely proportional to the distance as a result it is maximum at the inner radius and minimum at the outer radius. So to qualify as a test specimen, suitable for evaluation of B-H properties, the effective ratio of radial width to mean diameter should be $\leq$ 0.1 [116] (as per IEC 60404-4 standard). This ensures that the field is uniform within ± 11 % over the volume of the toroidal sample. The sample of inner diameter D_I = 8 cm and outer diameter D_O = 10 cm has been wound with the primary turns carrying the DC current to magnetize the sample and integrated induced voltage measured from the secondary turns using a flux meter. The primary winding current may be converted directly to the magnetic field by using the Ampere's circuital law, and the integrator output is proportional to the changes in the B-field within the sample. Before starting the measurement, the instrument should be adjusted for minimum drift, such that it should give zero B-field at zero input current. The B-H loop tracer measures the B-field, not the magnetization M as it is not possible to apply very large circumferential fields to a toroidal sample and B is large relative to H and the distinction between B and M is not significant. From the measurement, it has been found that the material M1 has the maximum B-field (B-saturation) of about 1.5 T, the remanent B-field (B_r) is about 0.7 T, the coercive H-field is about 160 A/m. The maximum relative permeability is about 2500.

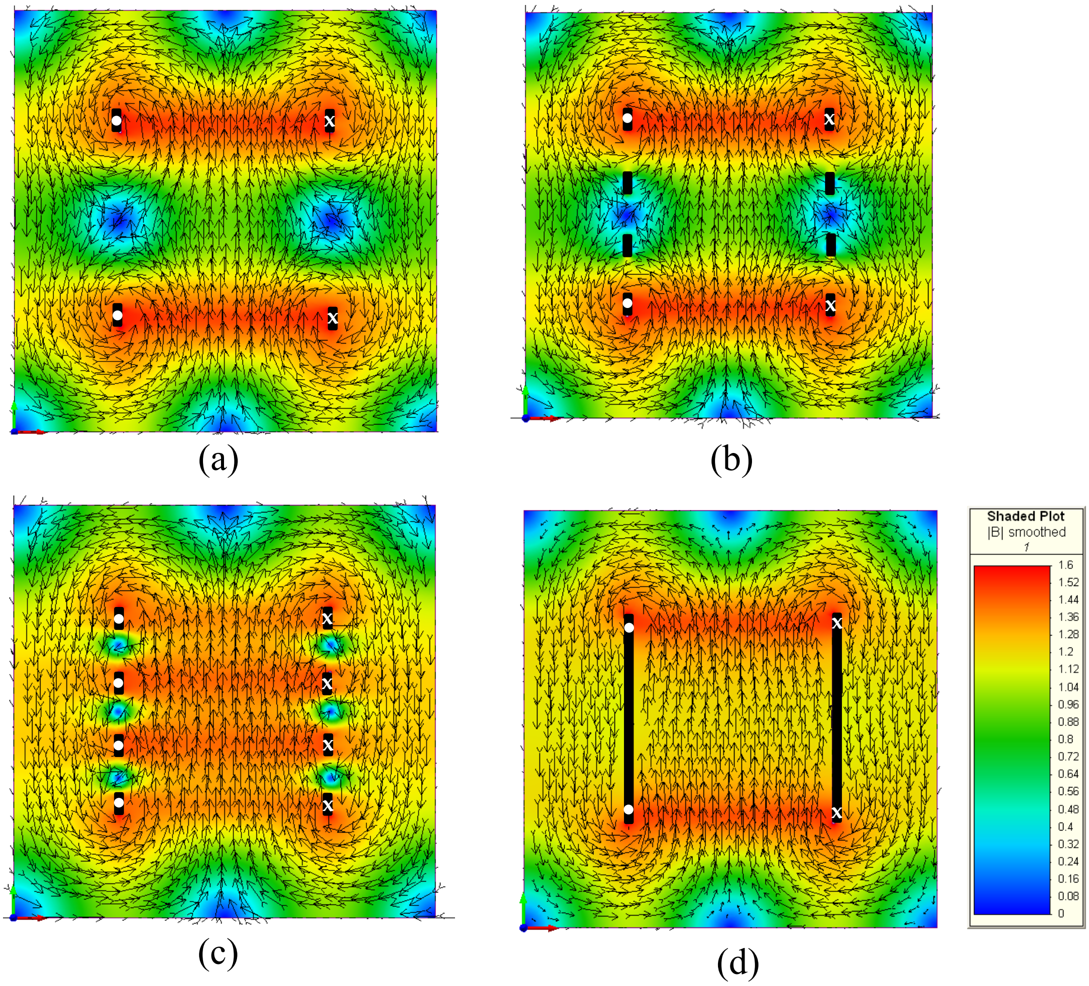

Figure 3.6: The B-field profile at 20 kA-turns for various slot configurations (top view of the ICAL), (a) 4 discrete slots carrying 2 coils, (b) 8 discrete slots carrying 2 coils, (c) 8 discrete slots carrying 4 coils and, (d) 2 continuous slots carrying 2 coils.

3.2 B-field distribution using various types of slots

The computation time to simulate the ICAL magnet having 151 layers of iron plate is very large. To reduce this time, a single layer of iron plate (16 m × 16 m × 0.056 m) with

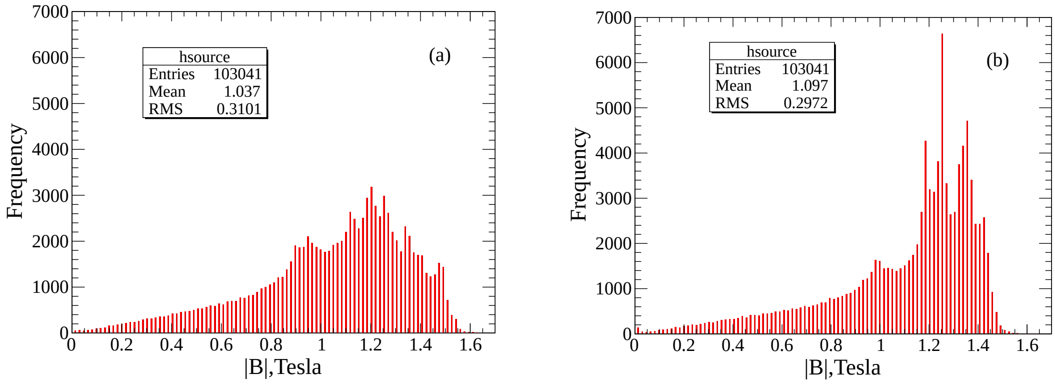

Figure 3.7: Distribution of the |B|-field in area of 16 m × 16 m, for the iron plate with (a) 4 discrete slots carrying 2 coils and (b) 8 discrete slots carrying 4 coils.

4, 8 discrete and 2 continuous slots having 2, 2 (4) and 2 (4) copper coils, respectively, has been used in the simulation. Figures 3.4 (a), (b) and, (c) show the iron plates having discrete and continuous slots, respectively, through which copper coils pass to energize the ICAL magnet. The coil length is ∼ 0.456 m and its width ∼ 8 m. The cross section of the coil through which current pass is 0.08 m × 0.625 m. The iron plate has 8 discrete slots carrying 2 coils which are placed at the 1st and 4th pair of slots (slot pairs are counted from the bottom to the top). The comparative studies on B-field for the configurations having one and three layers of iron plate with continuous slots carrying 4 coils are given in the Appendix[1]. The dimensions of the smaller sized slot, in Figs.3.4 (a) and (b) are 0.1 m (width) × 0.645 m (length) and the corresponding numbers for the continuous slots in Fig. 3.4 (c) are 0.1 m × 8 m. The center to center longitudinal separation between 2 coils is 7.355 m for the iron plate with 2 discrete and continuous slots (each carrying 2 coils) and for the configuration with 8 discrete slots carrying 4 coils is 2.452 m (same for continuous slots having 4 coils). Slots are positioned at a distance of about 4 m (slot edge to iron edge in both X and Y-directions) as shown in Fig. 3.4 (a) which is (considered as the baseline design) the reference slot configuration of the ICAL magnet for which magnetic lines of force should distribute symmetrically.

The B-field profiles for the configurations with various slot types are shown in Fig. 3.6. The filled white circles and crossed symbols represent, respectively, the outward and inward directions of current flow in the coils. The shaded plot with color gradient shows the

[1]We have checked that the simulated B-field with configuration having single layer of iron plate (coil dimensions: length - 8 m and height - 0.456 m) agrees with that for a single central plane (within 4 %) with that carrying coils of 8 m in length, 15 m in height and also for 3 layers placed symmetrically at the top, middle and bottom.

Table 3.3: Comparative study of the B-field distribution of the ICAL magnet for various slot configurations at 20 kA-turns.

No. of slots	Slots type	No. of coils	Currents per coil	FA (%)		
				$\lvert B\rvert >$ 1.0 T	$\lvert B\rvert >$ 1.2 T	$\lvert B\rvert >$ 1.3 T
4	Discrete	2	10	60.6	35.1	20.1
8	Discrete	2	10	61.1	35.1	20.1
8	Discrete	4	5	71.5	49.1	27.6
2	Continuous	2	10	78.7	40.9	17.5
2	Continuous	4	5	74.8	58.6	30.0
2	Continuous	1	20	70.8	54.9	26.8

magnitude of the B-field and shows how uniform or non-uniform it is over the area of 16 m $\times$ 16 m. The orientation and length of the arrows represent the direction and magnitude of the B-field, respectively. To find out the fiducial volume of the detector, the B-field distribution over the area of 16 m $\times$ 16 m is needed. Then, the B-field is averaged over a pixel size of 5 cm $\times$ 5 cm to find out the distribution in the entire area. The distributions of the B-field for configurations having 4 and 8 discrete slots carrying 2 and 4 coils, respectively, are shown in Fig. 3.7. A comparative study on B-field distribution in iron due to various slot types is given in Table 3.3. The iron plate with either 4 or 8 discrete slots containing 2 coils gives nearly the same fractional area (FA) for $|B| > 1$ - 1.3 T. On the other hand, plate layers with 8 discrete slots carrying 4 coils, provide a larger FA of ~ 71 %, compared to that containing 2 coils (~ 61 %) at $|B| > 1$ T. This is due to the fact that when the iron plate has 4 coils, the high field region is distributed over a larger area compared to that of 2 coils. The reduced separation between consecutive coils also helps. An iron plate with continuous slot, on the other hand, gives B-field uniformity over a much larger area (~ 79 %) as compared to the plate with 4 (~ 61 %) and 8 (~ 61 %) discrete slots for $|B| > 1$ T, with each of these configurations containing 2 coils (iron plate with 8 discrete slots containing 2 coils are placed at first and fourth pair of slots, counted from bottom to top). In discrete slot configurations, magnetic lines of force partly go in between slots whereas in a configuration that has continuous slots, magnetic lines of force go around the slots as shown in Fig. 3.6. This is because magnetic lines of force follow a path of

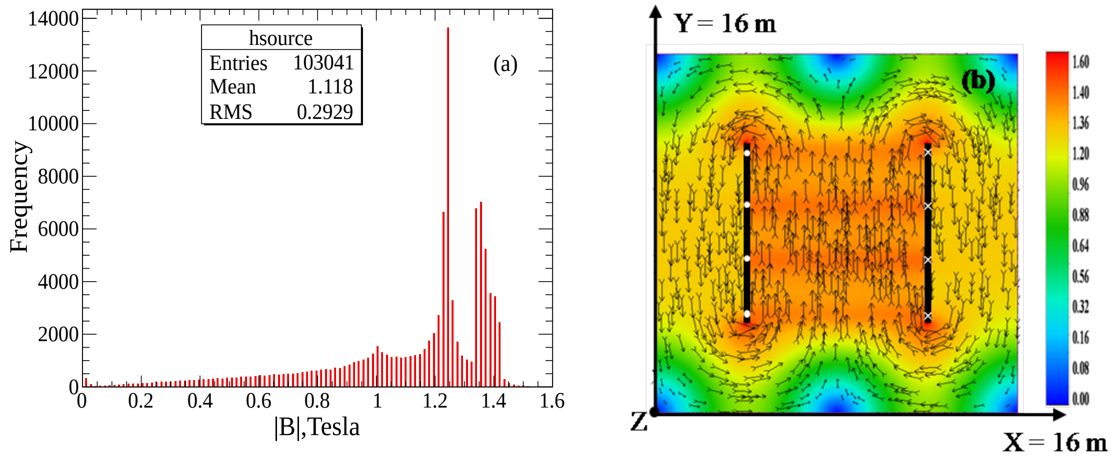

Figure 3.8: (a) Distribution of the |B|-field in area of 16 m × 16 m, (b) shaded plot of B-field with arrows, for magnet with continuous slots containing 4 coils at 20 kA-turns.

minimum reluctance (defined as $\frac{l}{\mu A}$, 'A' is cross sectional area through which magnetic lines of forces pass and 'l' is the path length traversed in iron) and get distributed more evenly compared to the case when the plate has discrete slots. Further, studies have been carried out on the B-field distribution for the configuration with continuous slots carrying 4 coils. The B-field distribution is shown in Fig. 3.8 (a), at 20 kA-turns where each coil carries 5 kA. It shows an average B-field of ~ 1.1 T over the 16 m × 16 m area. It has been found that at 20 kA-turns, the configuration with continuous slots and 2 coils gives about 79 % of the FA for which $|B| > 1$ T, whereas for the configuration with 4 coils it is about 75 % (sea Table 3.3). On the other hand, the configuration with 4 coils provides a larger area for which $|B| > 1.2$ T (or 1.3 T). Hence, it has been concluded that the configuration with continuous slots carrying 4 coils is suitable with respect to the B-field distribution. Figure 3.8 (b) shows the shaded plot of the B-field. A lower B-field is found in the peripheral regions of the plate i.e. at the four corners and at the middle top and bottom part of the plate, whereas, a higher field is found in regions which have proximity to the coils. From this, it is clear that all parts of the plate will not be equally effective for reconstruction of muon momenta and charge. It also shows that the B-field variation i.e. $\frac{|\Delta B|}{|B|}$, on either side of a slot is about 9 % and reduced to ~ 8 % at 60 kA-turns. Unless otherwise mentioned, the B-field variation along the plate thickness is about 0.1 %.

3.3 Improvement of B-field distribution

Further studies have been carried out for improving the strength and uniformity of the B-field with several modifications such as changing slot dimension, coil distributions in slot, magnetic materials and varying the plate thickness.

3.3.1 Effect of various coil distributions and Ampere-turns

In the previous section, it may be recalled, a better B-field distribution is obtained in the iron plates with continuous slots containing 4 sets of coils. In addition, increasing the number of coils (of the same cross section) results in a decrease in current per coil leading to a reduction in the Ohmic losses. Therefore, the simulation has been also carried out

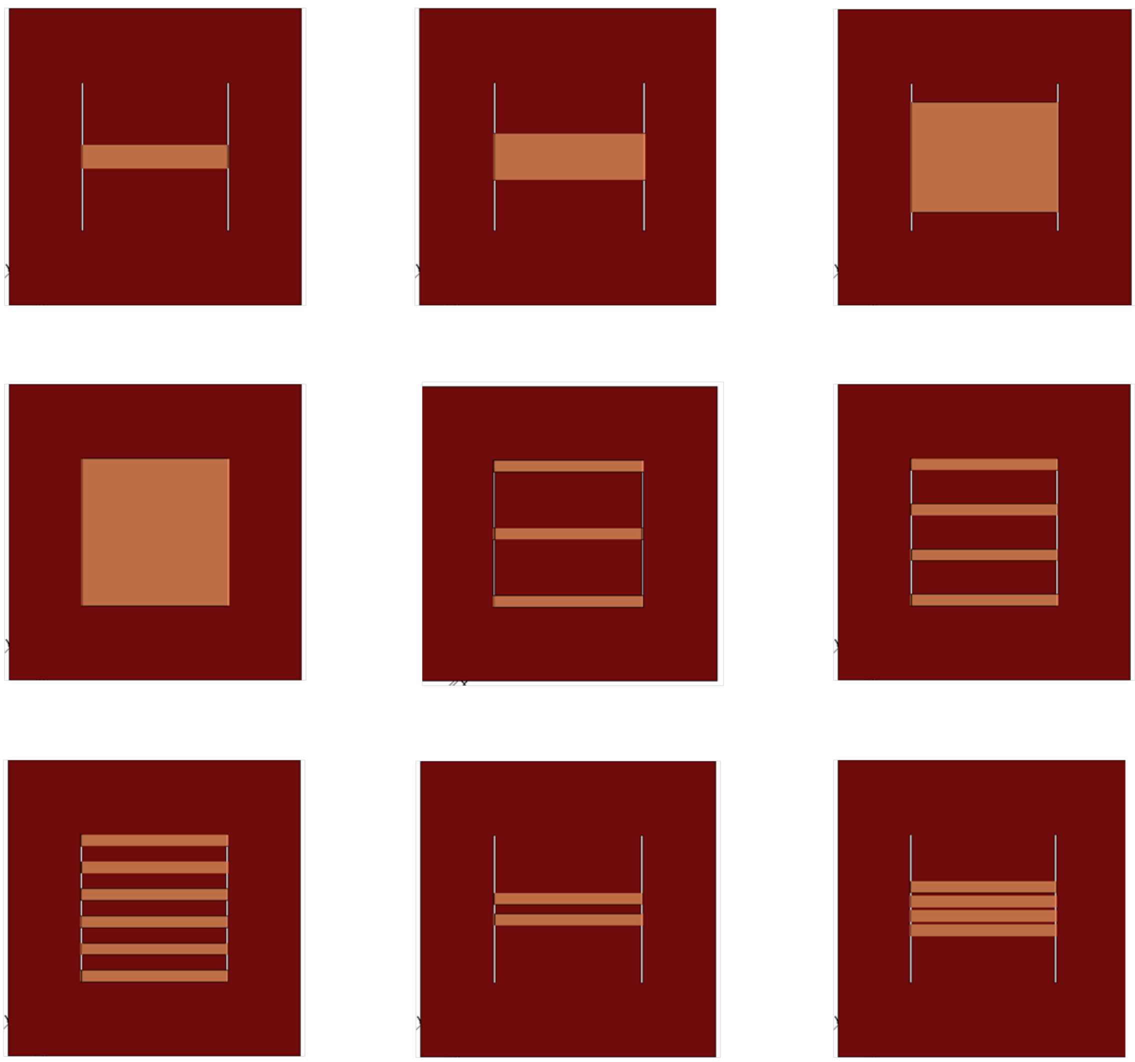

Figure 3.9: Plate has continuous slots with different coil distributions.

considering continuous slots having various coil distributions within the slots as shown in Fig. 3.9 at a fixed current of 20 kA-turns. Results obtained from the simulation on B-field distribution are given in Table 3.4. The distributions with 2 (min.) and 4 (min.) coils correspond to the minimum separation of 50 cm and 15 cm, respectively, between adjacent coils. It has been found that the B-field distributions improve by placing only single coils and by increasing its cross-section. However, it further increases putting discrete coils in place of single coils. It has been also observed that the configuration carrying 3 or 4 coils in continuous slots gives similar results on B-field distribution with the average |B| > 1.0 T. Hence, the plate with 4 coils is optimum with respect to field distribution and Ohmic loss.

Table 3.4: Comparison of the B-field distribution for the ICAL magnet with continuous slots carrying coil of different cross sections at 20 kA-turns.

Sl. No.	No. of coils	Current per coil(kA)	cross-section (m^2)	FA (%)		
				|B| > 1.0 T	|B| > 1.2 T	|B| > 1.3 T
1	1	20.0	0.08×1.250	57.63	26.31	11.28
2	1	20.0	0.08×2.500	59.86	32.03	13.18
3	1	20.0	0.08×6.000	66.61	48.88	21.73
4	1	20.0	0.08×7.800	70.79	54.98	26.85
5	2	10.0	0.08×0.625	78.69	40.96	17.55
6	3	6.666	0.08×0.625	76.20	59.42	29.53
7	4	5.0	0.08×0.625	74.87	58.63	30.00
8	6	3.333	0.08×0.625	72.33	56.66	28.44
9	2(mini.)	10.0	0.08×0.625	59.27	30.16	12.51
10	4(mini.)	5.0	0.08×0.625	60.91	35.30	14.33

It is also desirable to optimize the B-field with respect to Ampere-turns considering the design in which iron plate has continuous slots carrying 4 coils as shown in Fig. 3.10 (a). The

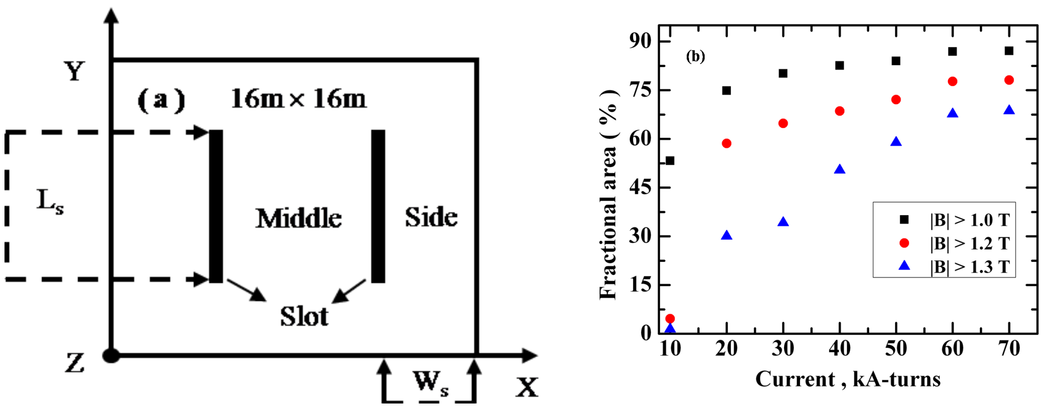

Figure 3.10: (a) Schematic of the ICAL magnet with different sections. L_s, W_s are length of slot and width of side section, respectively and (b) the |B|-field uniformity as a function of current for steel plate with slot length of 8 m.

dimensions of the continuous slots are: length, L_s = 8 m and width, W_s = 0.1 m. Figure 3.10 (b) shows that the FA for which |B| > 1 T increases with current and starts saturating about 20 kA-turns. However, at higher values (≥1.2 T), it increases with Ampere-turns though the increase is slow. So it has been concluded, the configuration with single plate carrying 4 coils, the desired current is about 25 kA-turns to 30 kA-tuns. It may noted here that all the studies reported in the subsequent sections have been carried out considering continuous slots carrying 4 coils.

3.3.2 Effect of slot dimensions

Studies show that the configuration with continuous slots gives an acceptable B-field distribution over the 16 m × 16 m area. In order to seek further improvement, the simulation has been carried out by changing the length of continuous slots, L_s , and their position (i.e. reducing the width (W_s) of side section) as shown in Fig.3.10 (a). The details of the comparative study are given in Table 3.5 at two different Ampere-turns. It shows that at fixed W_s (3.95 m) and current of 20 kA-turns, the B-field distribution in iron increases from nearly 66 % to 84 % with increase in L_s from 7 m to 10 m for |B| > 1 T and then further decreases with increase in slot length. The increase of FA by increasing slot length is due to the fact that lines of force turn around the slot and concentrate towards the edge of the plate (minimum reluctance path). The FA for which |B| > 1 T decreases with a further increase in slot length because the large B-field fringes out at the edge of the plate close to slot positions *i.e.* at x = 4 m and 12 m for y = 0 m and 16 m respectively. At 20 kA-turns, the FA for which |B| > 1.2 T increases from L_s = 7 m to 9 m (similarly 7 m to

Table 3.5: The B-field uniformity of a single plate with several slot lengths (L_s) and width of side sections (W_s) for currents of 20 kA-turns and 60 kA-turns. Here 'd' is the centre to centre separation between 2 consecutive coils.

L_s(m)	W_s(m)	d(m)	FA (%), 20 kA-turns			FA (%), 60 kA-turns		
			|B| > 1.0 T	|B| > 1.2 T	|B| > 1.3 T	|B| > 1.0 T	|B| > 1.2 T	|B| > 1.3 T
8.0	3.95	2.452	74.8	58.6	30.0	86.9	77.7	67.6
8.0	3.50	2.452	76.0	61.8	36.4	86.7	74.7	66.6
7.0	3.95	2.118	65.8	53.1	26.9	77.3	63.7	55.5
7.0	4.50	2.118	46.2	26.7	22.8	64.0	32.0	26.5
9.0	3.95	2.785	81.5	63.2	32.4	88.3	80.9	68.6
9.0	3.50	2.785	82.1	69.3	33.7	89.6	82.7	76.2
10.0	3.95	3.118	83.1	46.9	20.3	89.6	82.1	60.5
10.0	3.50	3.118	84.4	55.1	20.1	91.6	85.9	80.4
10.5	3.95	3.285	82.6	44.8	16.2	89.8	81.8	56.7
11.0	3.95	3.451	80.5	31.4	11.6	89.6	80.3	51.7
11.5	3.95	3.617	76.8	20.8	7.5	89.3	75.1	49.3
12.0	3.95	3.784	64.5	13.2	6.2	88.6	71.9	48.7
13.0	3.95	4.117	27.7	5.4	4.0	85.7	67.4	35.4
14.0	3.95	4.450	5.9	2.7	2.1	79.4	45.6	26.1

8 m at |B| > 1.3 T) and then decreases as the path length followed by the lines of force around the slot increases and also the separation between coils increases. In addition, at L_s = 7 m and W_s = 4.50 m, FA reduces from ~ 46 % and ~ 23 % at |B| > 1 T to 1.3 T, respectively. This is because the lines of force follow the minimum reluctance path and are not evenly distributed in the plate. The FA for which |B| > 1 T to 1.3 T increases with decreasing W_s for a given L_s. This is due to the increase in the B-field within a smaller

area (W_s × plate thickness). A similar behavior has been also observed at a current of 60 kA-turns. The configuration with slot length L_s = 10 m and W_s = 3.5 m seems to be the optimal with respect to the B-field distribution in 16 m × 16 m area of iron plate. The configuration with slot length L_s = 9 m and width of side section W_s = 3.95 m is suitable from a practical design standpoint and is close to the optimal value. From this study, it has been observed that by increasing the length of the slot and decreasing the width of the side section, the B-field uniformity increases in a larger area. In reality, the choices of the slot dimension and their position will also be constrained by the other mechanical properties of the ICAL magnet and the sizes of the RPC detectors.

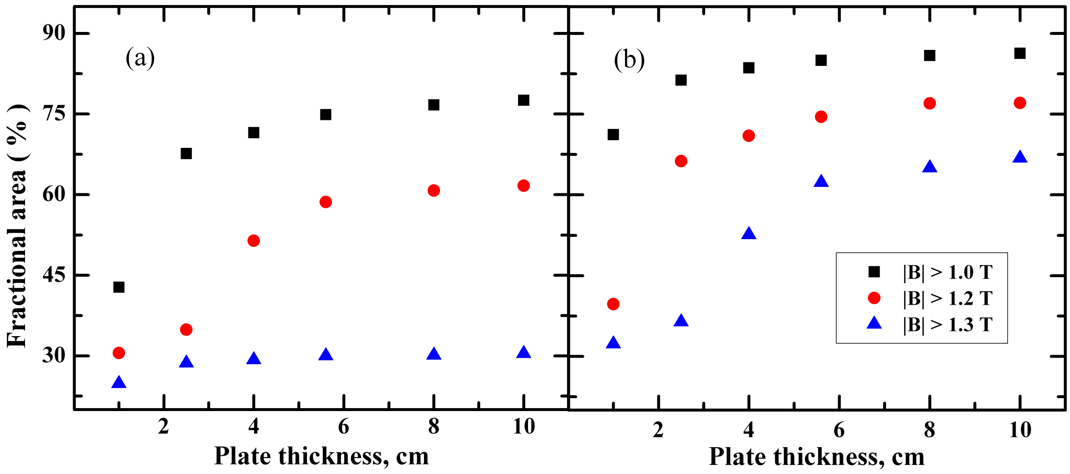

Figure 3.11: Comparison of FA for different |B|-field, using a single layer of iron plate with continuous slots carrying 4 coils as a function of plate thicknesses for (a) NI = 20 kA-turns and (b) NI = 60 kA-turns.

3.3.3 Effect of plate thickness

At low energy, the momentum resolution of muons is affected by the multiple Coulomb scattering, which increases with increase in plate thickness. At high energy, the resolution becomes poorer and there is decrease in charge identification capability due to the reduction in bending of the particle trajectory. This study has, therefore, been carried out using the "baseline" ICAL configuration (continuous slots with 4 coils) by varying only the plate thickness. It shows that at fixed value of current of 20 kA-turns, the FA for which |B| > 1 T increases with increase in plate thickness as shown in Fig. 3.11 (a) and saturates for plate thickness beyond about 4 cm. This is because the magnetic lines of force get redistributed in the iron due to increase in plate thickness. It has been also found that FA for which |B| > 1.3 T shows saturation effect with increase of plate thickness. A similar behaviour is found for total current of 60 kA-turns (15 kA per coil) as shown in

Fig. 3.11 (b). Therefore, the fractional area for which |B| > 1.0 T increases with current and is roughly independent of plate thickness when the latter is greater than about 4 cm. Finally, the dependence of field uniformity with plate thickness reinforces our choice of 56 mm as the design value.

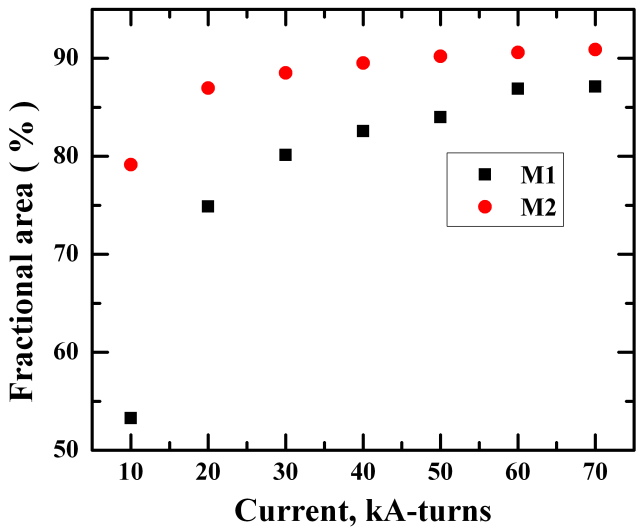

Figure 3.12: Comparison of FA with |B| > 1.0 T, as a function of current for the iron plate with two different soft magnetic properties M1 and M2.

3.3.4 Effect of different soft magnetic properties

While making such a huge magnet with a reasonably high B-field, it is necessary to choose the magnetic material which requires less current (Ampere-turns) to magnetize it. A study of the B-field distribution has been carried out using materials with different magnetic properties such as softness (for which the carbon content is crucial). In the electromagnetic simulation of the ICAL magnet, the B-H data has been assigned as a material property in the input of the software. The comparative study has been carried out by considering two representative materials with different magnetic properties as shown in Fig. 3.5, for the configuration with single layer of iron plate (16 m $\times$ 16 m $\times$ 0.056 m) with continuous slots carrying 4 coils. It has been found that an ICAL magnet made up of material M2 gives a larger FA for which |B| > 1 T compared to that with M1 at the same Ampere-turns, as shown in Fig. 3.12. In particular, at lower Ampere-turns (10 kA-turns), material M2 gives more FA ($\sim$ 79 %) compared to M1 ($\sim$ 53 %) and at higher current (60 kA-turns) the difference between them reduces (material M2 gives $\sim$ 90 % and M1 $\sim$

87 %) for which |B| > 1 T. Both materials show the saturation of B-field at higher currents. This study shows the importance of using a magnetic material with a large susceptibility, which could lead to large savings in electrical power as a lower current is required to energize the magnet for the same B-field. Alternatively, for the same current, a higher B-field is obtained. In practice, though, the availability and cost might be the overriding factors.

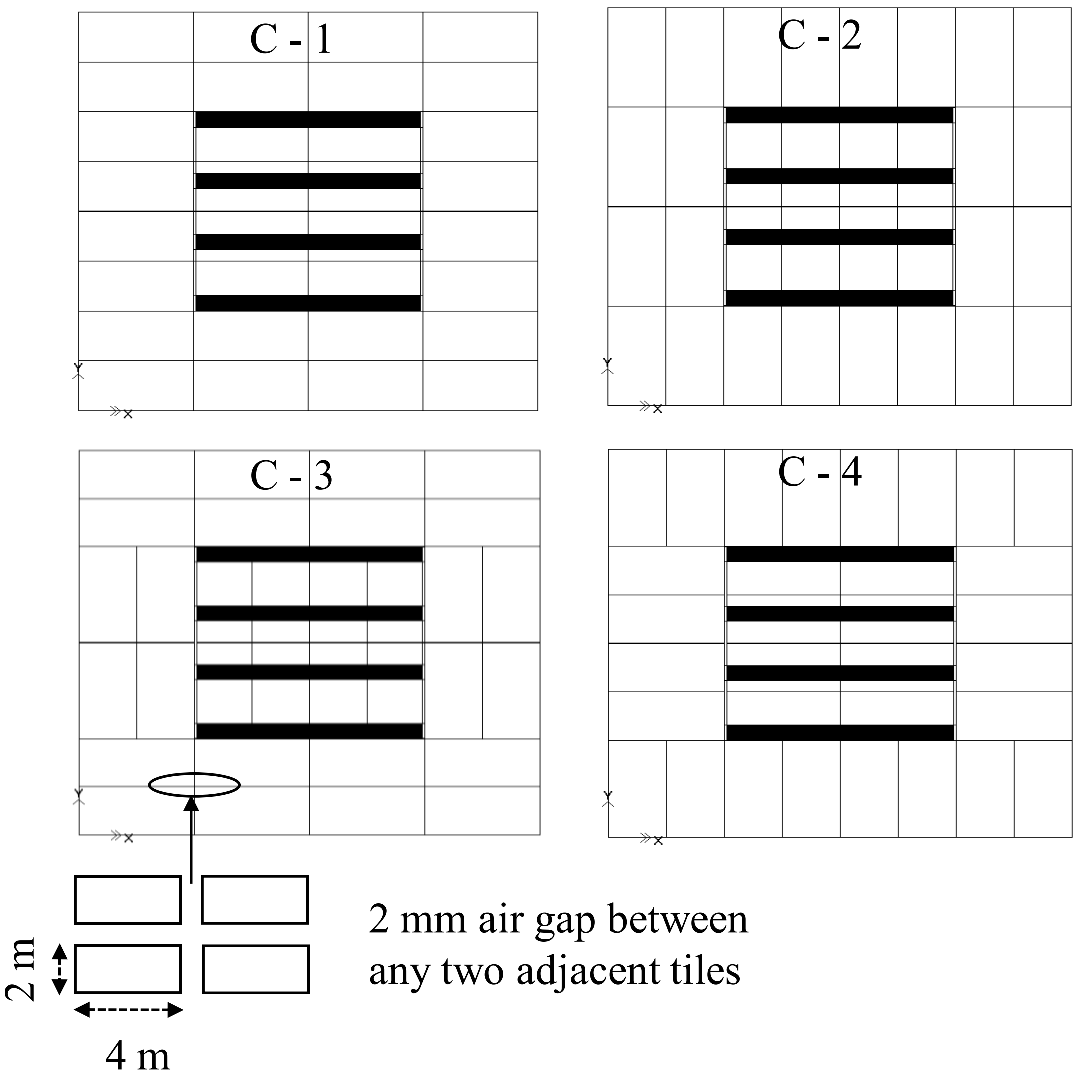

Figure 3.13: The ICAL magnets with various arrangements of tiles. The dark black rectangular boxes show the coils (Top view).

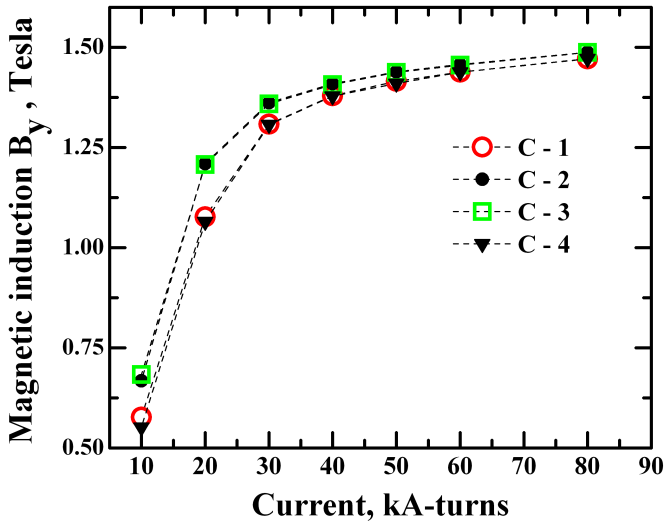

Figure 3.14: The B-field variations with currents for configuration C1 to C4.

3.4 B-field distribution using realistic design of the ICAL

All the studies described above are carried out for various designs considering only a single layer of 16 m × 16 m × 0.056 m iron plate. Practically, however, building the ICAL detector using such a large sized plate, even if it is available, is not possible because it cannot be transported to the cavern through a tunnel of transverse dimension ∼ 7.5 m. So, the 16 m × 16 m area will be tiled with smaller sized plates. Due to mechanical tolerances, there may be air gaps among the tiles. At the air gaps, the magnetic lines of forces "fan out" a bit leading to a fringe field in the vicinity of the air gap which also leads to the reduction of flux linkage between the iron plates. As a result, more Ampere-turns are needed for getting the required B-field. Hence, it is important to consider the orientation and positioning of the tiles such that the magnetic lines of force follow a path where the ratio of length of air gaps to the path length in iron for any layer should be the minimum possible. A smaller size of the tile results in a larger ratio making it inefficient while a smaller ratio due to a larger tile size results in difficulties in handling plates. Therefore, the choice of 4 m × 2 m × 0.056 m as the iron plate unit or tile (mass ∼ 3.5 tons) to construct the 16 m × 16 m iron layer is a good compromise between mechanical constraints imposed by the cavern size and power economy in generation of the magnetic field.

Initially, the simulation was carried out considering tiles of size 4 m × 2 m with a gap

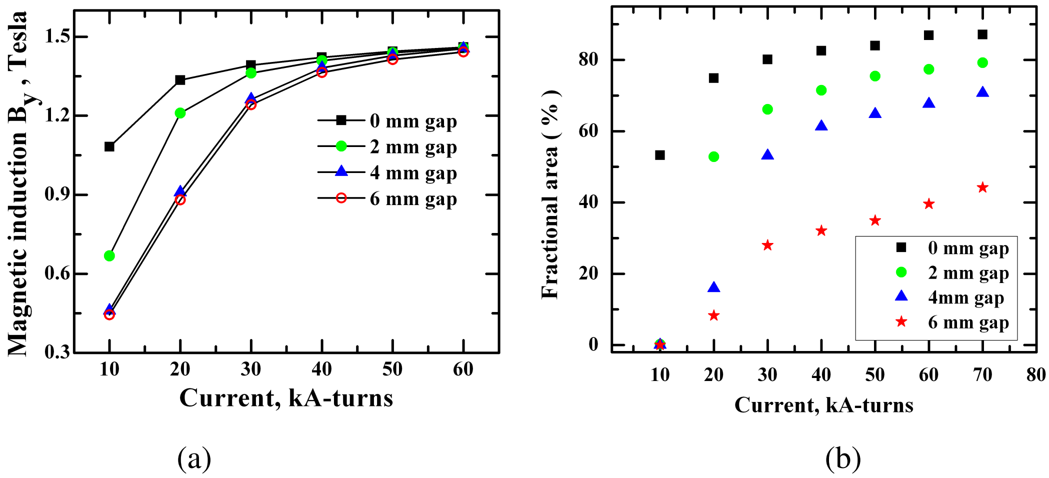

Figure 3.15: (a) The B-field variation as a function of current for various gaps between any two adjacent tiles of the C-2 configuration, (b) Comparison of variation of FA with current for single layer of ICAL magnet and C-2 configuration at |B| > 1 T.

of 2 mm between them. The gap as shown in Fig. 3.13 (extended view) arises due to mechanical tolerances. The tiles are arranged in 4 configurations, C-1 to C-4, to evaluate which of the configurations give the maximum B-field for the minimum Ampere-turns. Figure 3.14 shows that configurations C-1 and C-4 give the same B_y (point of observation is nearly middle of the plate where B-field is almost in the y-direction) for any current and a similar behaviour is displayed by the C-2 and C-3 pair. The configuration C-2 gives $\sim$ 14 % and $\sim$ 2 % more B_y at a total current of 20 kA-turns and 50 kA-turns, respectively, as compared to C-1. This is due to a smaller number of air gaps seen by the magnetic lines of force in a closed loop which results in less leakage of flux so that the C-2 configuration appears to be optimum. Therefore, considering the C-2 configuration, the effect of air gaps on both the B_y-field and FA area for which |B| > 1 T in iron are shown in Fig. 3.15 (a) and (b), respectively, for gaps of 0 mm (single plate, no tiling structure), 2 mm, 4 mm and 6 mm. The B-field in iron decreases with increase of air gaps as the fringing flux increases. At a lower current the fractional reduction in B-field is higher than that at higher values of the current.

Further, a comparative study has been carried out between a single monolithic layer (no tiling structure) of iron plate of size 16 m $\times$ 16 m $\times$ 0.056 m and a layer with the C-2 tiling configuration, with inter-tile gaps of 2 mm, 4 mm and 6 mm, considering their B-field distribution. It has been observed that the FA for which $|B| \geq 1$ T reduces by increasing of gaps among the tiles with respect to a single monolithic plate as shown in

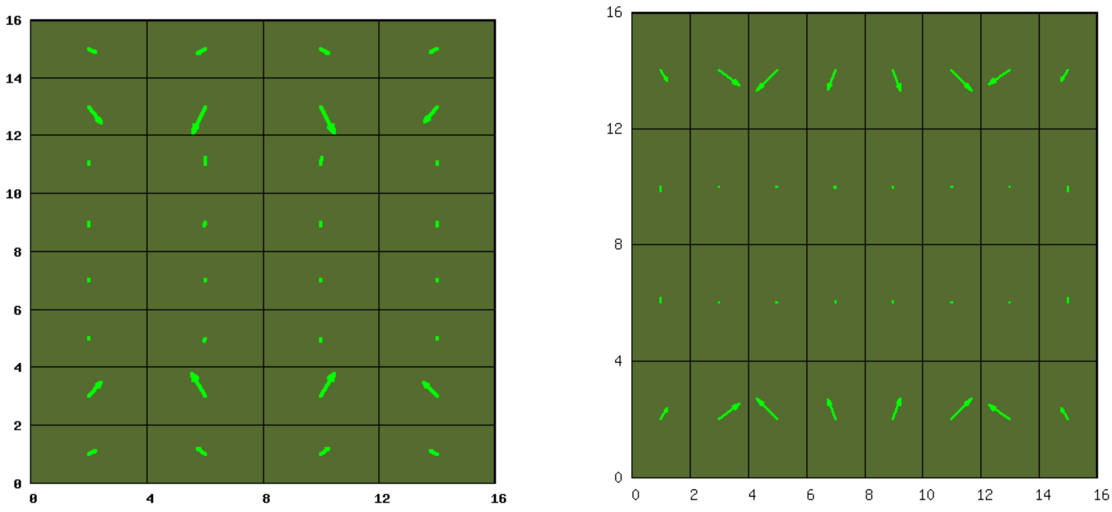

(a) (b)

Figure 3.16: Magnetostatic forces among tiles for configurations (a) C1 and (b) C2. The length of arrows represents the magnitude of resultant force (normalized with respect to maximum value ~ 100 kN) and the orientation shows the resultant direction.

Fig. 3.15 (b) at a given Ampere-turns. This is due to the leakage of field lines which occurs at the air gaps. The reduction in field distribution is more at a low current, for example at 20 kA-turns, where a single monolithic plate gives ~ 76 % whereas for the tiling structure of various gaps the FA for which $|B| > 1$ T is between 10 % and 54 % and the difference between single plate and tiled structure reduces for higher current. This shows that the smaller the gap between the tiles the larger the FA of ICAL magnet for a certain minimum B-field. An inter-tile design gap of 2 mm, therefore, has been decided taking into account the simulations and mechanical tolerances involved in the mechanical assembly of the ICAL magnet.

3.5 Magneto-static forces among tiles

The study of the magneto-static forces on the tiles has been carried out for configuration C-1 to C-4 with the nominal gap of 2 mm among tiles. As the magnetic lines of forces pass from one tile to other, the force of attraction among tiles could have out of plane components that may tend to disrupt the planar arrangement. Consequently the mechanical stability of the ICAL may be affected and the movement of RPC detectors may get constrained. The mechanical stability of the ICAL detector could also be compromised by the magnetostatic forces between the iron plates. Instead of using the conventional

Maxwell stress tensor, the Magnet software uses a novel tunable method [117] to estimate the magnetostatic force. Figure 3.16 shows the magneto-static forces among tiles for configuration C1 and C2. The length of the arrow represents the magnitude ($\sim$ 100 kN against the $\sim$ 35 kN tile weight) of the resultant force (dominated by the x-component and y-component of forces) and the orientation shows the resultant direction. It has been found that forces among tiles are inwards which tends to squeeze them together. The magnitude of force on a plate is more on the peripheral ones and very small on the inner ones as in latter case the forces, while themselves large, cancel each other.

Chapter 4

The ICAL Response to Muons

In the previous chapter, we have studied the magnetic field uniformity and its strength in the ICAL magnet for various conditions. The magnetic field map obtained from the electromagnetic simulation may be used to study the response of the ICAL to muons produced as a result of a neutrino induced event when the latter interacts with the nucleons of iron. In the magnetized ICAL detector at the INO, the reconstruction of the hadron 4-momentum is almost independent of magnetic field whereas the reconstruction of the 4-momentum for the muon depends on the strength of the magnetic field. The response of the ICAL to muons at various strengths of the magnetic field will be described in this chapter. The main aim of this study is to optimize the magnetic field with respect to the response of the muon.

1 Effect of magnetic field on relativistic muons

The principal goal of the ICAL detector at the INO is to address the neutrino mass hierarchy. So, it is important to distinguish the neutrinos by identifying the leptons produced in a CC interaction. Also, it is necessary that the neutrino energy and incoming direction be accurately measured in each event. The measurements of energy and incoming direction of the neutrino depend on the detector resolution. The energy of the neutrino is the sum of the muon and the hadron energy for a given CC events. The muon energy may be measured either from its curvature in a magnetic field or from the range of muons stopping in the detector or both. The muon energy resolution is affected by both the multiple Coulomb scattering and the uncertainty in position measurement. The details of the magnetic field strength dependent energy resolution are described below.

The motion of a charged particle in a magnetic field is governed by the Lorentz force (F),

$$\vec{F} = q(\vec{v} \times \vec{B}) \,, \tag{4.1}$$

where q is the electric charge of the particle, $\vec{v}$ is velocity of the particle and $\vec{B}$ is the magnetic induction. The charged particle experiences a force in a direction perpendicular to the velocity. A force perpendicular to the velocity results in centripetal acceleration. Therefore the charged particle describes a helical path with constant speed and the magnetic force works as the centripetal force. Then, rewriting Eq. 4.1, we have

$$\frac{mv_{\perp}^2}{r} = qv_{\perp}B \,, \tag{4.2}$$

where 'r' is the radius of curvature of the trajectory and 'm' is the mass of charged particle (in relativistic case, $m = \frac{m_0}{\sqrt{1-\frac{v^2}{c^2}}}$). Then rewriting Eq. 4.2,

$$p = 0.3B\,r \,, \tag{4.3}$$

where 'r' is measured in m, 'B' is measured in Tesla (T) and 'p' is the momentum (component perpendicular to B) of the charged particle measured in GeV/c. In a magnetized detector, the momentum resolution depends on the precise measurement of sagitta as shown in Fig. 4.1 (defined as the perpendicular distance from center of an arc to center of the base) which is related to the angular deflection. The angular deflection of the charged particle caused by the magnetic field as shown in Fig. 4.1 is given by,

$$sin\frac{\theta}{2} = \frac{L}{2r} \Rightarrow \frac{\theta}{2} \approx \frac{L}{2r} \Rightarrow \theta \approx \frac{0.3BL}{p}, \tag{4.4}$$

where L is the length of an arc. The sagitta (s) of the track may be measured as,

$$s = r - r\,cos(\theta/2) \approx r\left[1 - \left(1 - \frac{1}{2}\frac{\theta^2}{4}\right)\right]. \tag{4.5}$$

Then incorporating Eq. 4.4 in Eq. 4.5 and expressing s in terms of momentum,

$$s = \frac{r\theta^2}{8} \approx \frac{0.3BL^2}{8p} \,. \tag{4.6}$$

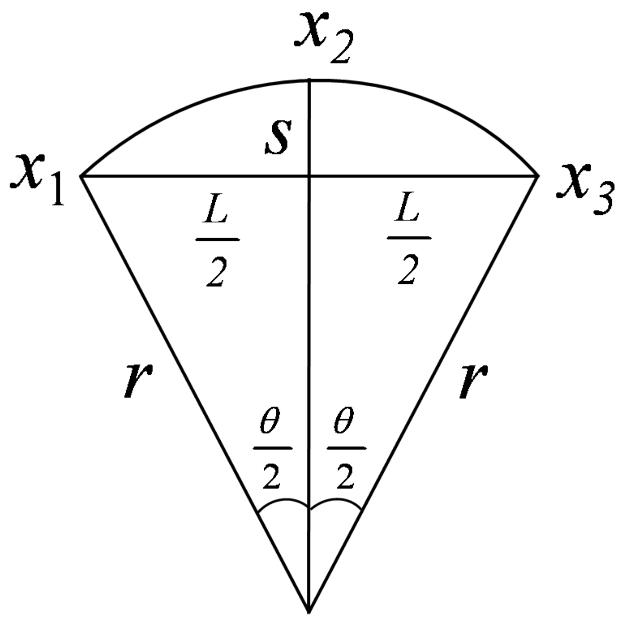

Figure 4.1: Schematic representation of arc and sagitta (s) of a track.

The error on momentum measurements depends on the fluctuation on sagitta (δs),

$$\begin{aligned} \delta s &= \frac{0.3BL^2}{8p^2}\delta p \\ \Rightarrow \frac{\delta p}{p} &= \frac{\delta s}{s}. \end{aligned} \tag{4.7}$$

So the relative momentum error can be written as

$$\frac{\delta p}{p} = \frac{8\delta s}{0.3BL^2}p\,. \tag{4.8}$$

From Eq. 4.8, it may be observed that the relative momentum error varies as $1/BL^2$. So it may be reduced by increasing the magnetic field (increases the bending leading to a smaller δs) and increasing the size of tracking detector (L^2). It also shows that the error increases linearly with the momentum. Therefore, increase in the momentum of particle to a large values causes the s very small so that one cannot distinguish whether it is a positive or a negative charged particle. Thus, at sufficiently high momentum, the detector is less capable of identifying the charge of a particle. In an actual experiment, sagitta can be estimated from the position measurement. The fluctuation in position measurement leads to the uncertainty in s. Let us consider that, s was measured using three points x_1, x_2 and x_3 as shown in Fig. 4.1. Then expressing s in terms of position co-ordinates, we have

$$s = x_2 - \left(\frac{x_1 + x_3}{2}\right). \tag{4.9}$$

Assuming $dx_i \approx \sigma(x)$, i=1, 2, 3, are the errors on the position measurements and they are independent of each other, then

$$\begin{aligned} ds = dx_2 - \frac{dx_1}{2} - \frac{dx_3}{2} \\ \Rightarrow (ds)^2 =& \sigma^2(x) + \frac{\sigma^2(x)}{4} + \frac{\sigma^2(x)}{4} \\ =& \frac{3}{2}\sigma^2(x) = \sigma^2(s)\ , \end{aligned} \tag{4.10}$$

where σ_s is the error on s. Now the relative momentum error considering the error on s (as $s \propto$ 1/p),

$$\begin{aligned} \frac{\delta p}{p} = \frac{\sigma(s)}{s} =& \frac{\sqrt{(3/2)}\,\sigma(x)}{s} \\ =& \sqrt{\frac{3}{2}}\,\sigma(x)\frac{8p}{0.3BL^2}\ . \end{aligned} \tag{4.11}$$

However, the momentum resolution is also affected by the multiple Coulomb scattering and it is more for a tracking detector with thicker absorbers. When a charged particle passes through a medium, the electric field due to an atomic nucleus may give a large acceleration or deceleration to it. This results in a change of direction for a heavy charged particle (m > m_e, m: mass of any other particle, m_e: mass of electron). The width of the angular deflection due to multiple scattering is given by [118, 119]

$$\theta_0 = \frac{13.6MeV}{\beta pc} z \sqrt{\frac{L}{X_0}}\,[1 + 0.038\,ln(L/X_0)]\ , \tag{4.12}$$

where βc and z are the velocity and charge number of the incident particle, and X_0 is the radiation length. The uncertainty in sagitta due to multiple scattering is given by,

$$\sigma_{ms}(s) = \frac{1}{4\sqrt{3}} L\,\theta_0\,. \tag{4.13}$$

Thus, the relative momentum resolution in terms of multiple scattering is given by

$$\frac{\sigma_{ms}(s)}{s} = \left(\frac{\delta p}{p}\right)_{ms} \approx kz\frac{1}{B\sqrt{LX_0}}\,[1 + 0.038\,ln(L/X_0)]\,, \tag{4.14}$$

where k is a proportionality constant. We can see from Eq. 4.14 that the relative momentum resolution due to the multiple Coulomb scattering is independent of p and is inversely proportional to B. So combining Eq. 4.11 and Eq. 4.14, the net relative momentum error can be expressed as,

$$\frac{\delta p}{p} = a_0 \oplus a_1 p \; , \tag{4.15}$$

where a_0 measure the uncertainty due to multiple scattering and a_1 is the uncertainty due to sagitta measurements. The energy and angle resolution of the ICAL detector depend on the muon energy, its incoming direction, strength of magnetic field, iron plate thickness etc. Unless otherwise mentioned, we deal with relativistic muons where E ~ pc and the momentum resolution is equal to the energy resolution.

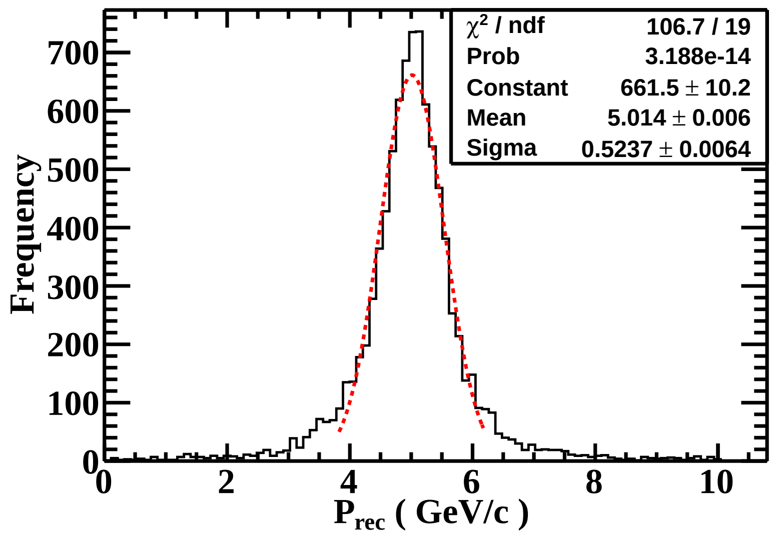

Figure 4.2: Reconstructed momentum distribution of 5 GeV muons at cos θ_z = 0.65 and B-field = 1.5 T. The dashed line shows the Gaussian fit to the distribution.

2 Simulation procedure

The study was carried out using the Monte Carlo based simulation toolkit GEANT4 [120] to find out the detector resolution and efficiency as a function of both the energy and direction (angle from vertical) of the muon. The magnetic field map in a grid size of 5 cm × 5 cm of the iron plate obtained from the electromagnetic simulation of ICAL magnet

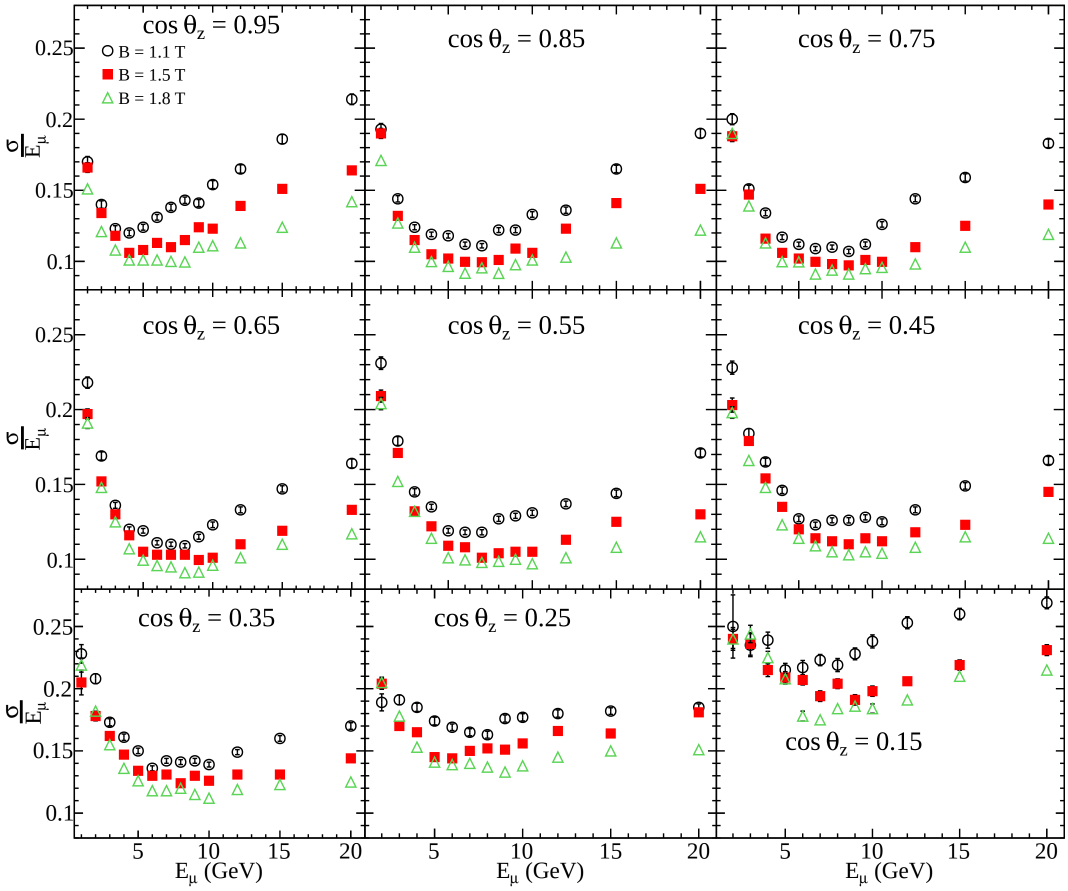

Figure 4.3: Comparison of energy resolution at B-field strengths of 1.1 T, 1.5 T, 1.8 T for various zenith angles, where muon vertices are generated in the central part of the detector.

was interpolated for the 16 m × 16 m area and used for muon tracking. A sample of 10^4 muons (μ^-) with fixed energies originate in the central region (8 m × 8 m × 12 m, central module of the detector, Chapter 3, see Fig. 3.2) of the detector where the B-field is nearly uniform as shown in Fig. 3.8 (b) of Chapter 3. It is important to consider the energy range 2 GeV to 10 GeV where ICAL has the highest sensitivity to the neutrino mass hierarchy. In this analysis we have considered the energy range from 1 GeV to 20 GeV. The lower limit on energy was based on the consideration that the thickness of iron plates in the ICAL detector makes it difficult to measure sub-GeV muons with a reasonable accuracy in momentum. At the higher end, the flux decreases and also, the measurement precision and efficiency becomes poor. The muons are incident at fixed zenith angles (θ_z) while the azimuthal direction (ϕ) is allowed to take any value from 0 to 2π. The range of zenith angles chosen for the analysis is cos θ_z = 0.1 - 1.0 with bin width Δcos θ_z = 0.1. The choice of the lower limit of the zenith angle of the neutrinos reaching at the detector is natural while the upper limit is guided by the fact that neutrinos at a zenith angle of 90°, leading to muons at a similar angle, would be very difficult, almost impossible, to reconstruct. In this analysis, for $\theta_z > 90°$ was not considered, as the incoming direction for neutrinos reaching at the detector is symmetric with respect to zenith angle. To find out the effect of the magnetic field on muons, values of B-field strengths considered are 1.1 T, 1.5 T and 1.8 T (values corresponds to the central region of the steel plate). To get magnetic field of strength 1.8 T, we have used material M2 as shown in Fig. 3.5 of Chapter 3.

An algorithm developed by the INO collaboration based on the Kalman Filter [121]

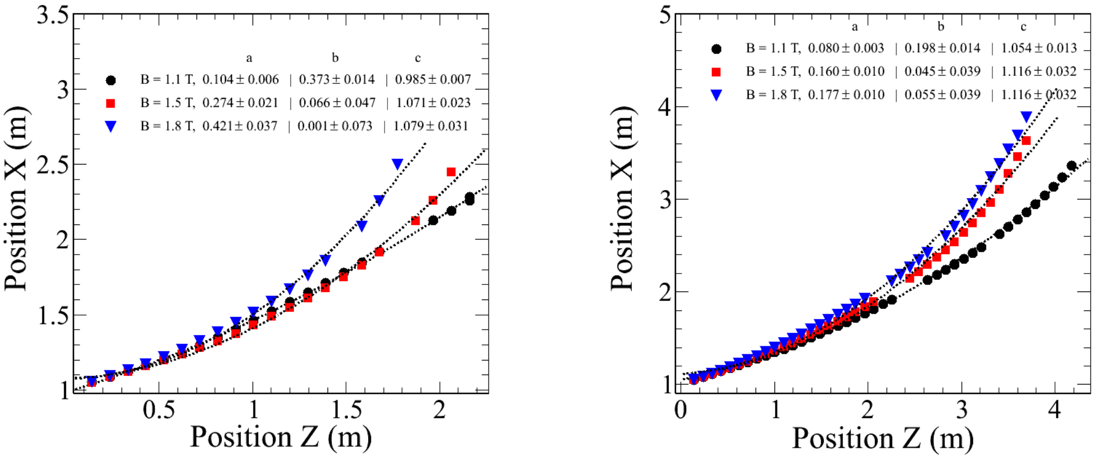

(a) (b)

Figure 4.4: Bending of muon tracks at different B-field for energy (a) 2 GeV and (b) 4 GeV, at cos θ_z= 0.95. Dotted lines show the track fitted with function, $ax^2 + bx + c$, where parameter 'a' measures the curvature of the track.

technique was used to reconstruct the muon considering the tracks close to the vertex. The momentum of the muon was reconstructed by putting a cut on χ^2, *i.e* χ^2/number of degrees of freedom is < 10. The reconstructed momentum distribution obtained from the simulation is plotted in the range of 0 to 2P$_\mu$, where P$_\mu$ is the input momentum measured in GeV/c. Figure 4.2 shows the distribution of the reconstructed momentum (P$_{rec}$) for 5 GeV muons incident at a zenith angle corresponding to cos θ_z = 0.65 and for all the azimuthal directions. This reconstructed momentum distribution is fitted to a Gaussian probability distribution function (p.d.f) in the range of P$_\mu$ − FWHM (full width half maximum) to P$_\mu$ + FWHM[1]. The dashed line shows the fitted Gaussian p.d.f of the reconstructed momentum spectrum. The standard deviation (σ) obtained from the fit was used to extract the energy resolution of muons. It was found that the reconstructed mean momentum agrees quite

[1]In the fit we have considered up to 1σ, keeping in mind that the momentum reconstruction will improve further in future by improving the reconstruction algorithm. As it is also affected by the spacers, the gap between detectors and the error on reconstruction of track leads to more uncertainty

well with the input value. A 3σ range of the reconstructed momentum spectrum was considered to estimate the detector reconstruction and charge identification efficiency for muons.

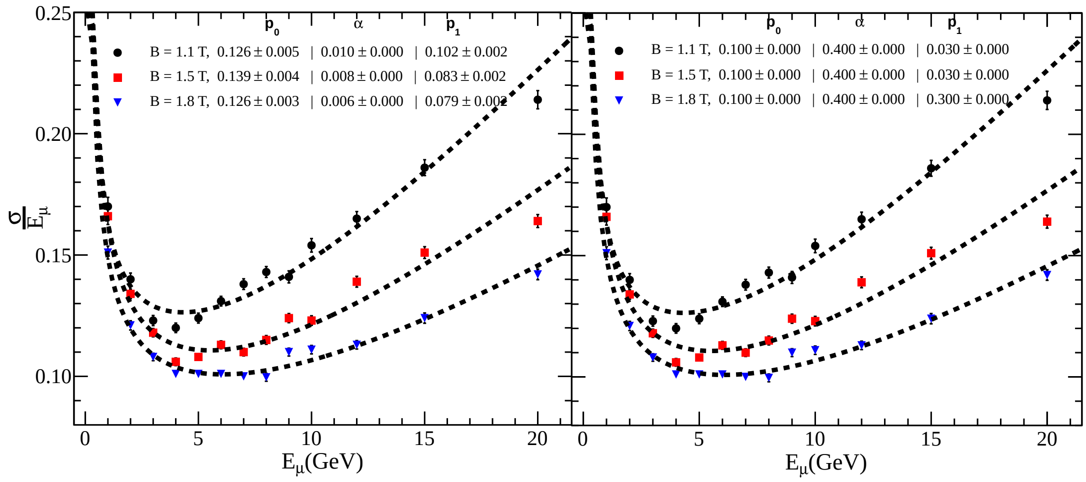

(a) (b)

Figure 4.5: Muon energy resolution incident at (a) cos θ_z = 0.95 and (b) cos θ_z = 0.65, for B-field strengths of 1.1 T, 1.5 T, 1.8 T. Energy resolution is fitted to a function $\frac{p_0}{E^\alpha} + p_1 E$ (dashed line)

3 Effect of Magnetic field on muon energy resolution

The energy resolution of muons is not only affected by the multiple scattering and bending of the trajectory, but also depends on the number of hit points used to fit the track [122]. At low energy, the resolution is mostly affected by the multiple Coulomb scattering and this reduces with increase of energy. Figure 4.3 shows the variation of resolution with energy at various magnetic fields strength of about 1.1 T, 1.5 T and 1.8 T for muons incident at cos θ_z = 0.95 (muons incident almost vertically downward) to 0.15. At a given strength of B-field, the energy resolution improves with increase in energy and thereafter becomes poorer at higher energy. At low energy ($E_\mu \leq 5$ GeV), the energy resolution improves with increasing energy as the number of hit points increases for fitting the track. At higher energy, the poorer resolution may be attributed to more uncertainties in the sagitta measurement as given in Eq. 4.11. Apart from this, the poorer resolution may also arise due to muons passing through the spacer of the detector or the trajectory falling in the gap between two RPC detectors and it is independent of energy. For a given energy, the resolution improves with increase in magnetic field due to increase in bending of trajectory as shown in Fig. 4.4 resulting a less uncertainty in the measurement of the sagitta. As muons are incident almost at the centre of the detector along the Z-direction and magnetic field at the central part of the detector is along the Y-direction, then the bending of muon is along the X-direction. The hit points also show discontinuity as it passes through the gap between detectors. The hit points are fitted with a function,

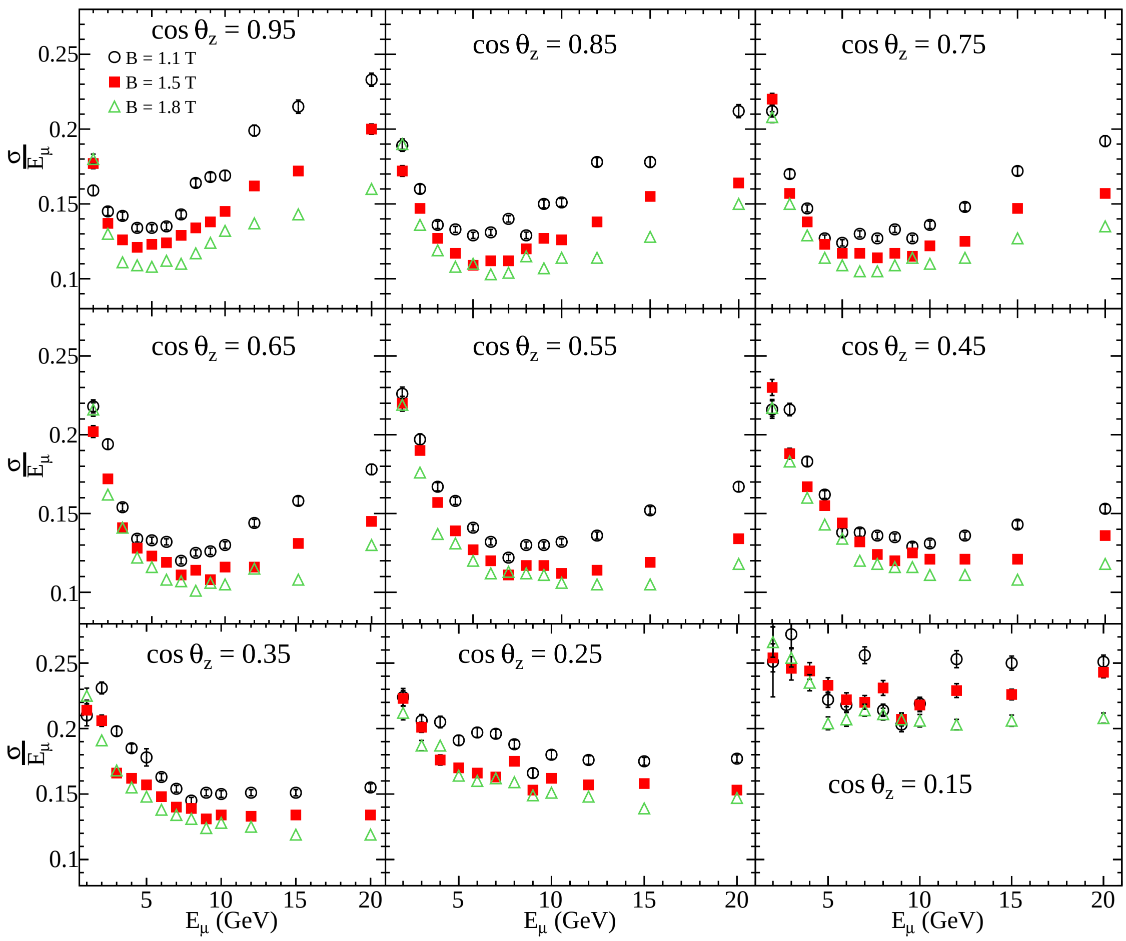

Figure 4.6: Comparison of energy resolution vs magnetic field for strengths of B = 1.1 T, 1.5 T, 1.8 T at zenith angles of cos θ_z = 0.95 to 0.15, where muon starting points are smeared over the entire volume.

$ax^2 + bx + c$, where parameter 'a' measures the curvature of the track. It shows that with increase of magnetic field, 'a' increases from ~ 0.1 to ~ 0.4 and ~ 0.08 to ~ 0.18 at fixed energy of 2 GeV and 4 GeV, respectively, for the muon incident at cos θ_z = 0.95. It may be observed that, the increase in curvature for 4 GeV muons is almost the same by increasing the magnetic field from 1.5 T to 1.8 T. It was also observed that the value of 'a' decreases with increase of energy. It was found that, at the higher energies, the energy resolution improves by ~ 21 % to ~ 29 % for energies about 9 GeV to 20 GeV, when the magnetic field is increased from 1.1 T to 1.8 T for muons incident at a zenith angle corresponding to cos θ_z = 0.65 (muon travels almost along the body diagonal of the detector corresponds to the maximum path length). It was also found that, with increasing the zenith angle (cos $\theta_z \leq 0.45$), the resolution deteriorates, as approaching the horizon, for which there is a reduction in the number of layers of RPC detector crosses by the muon.

Figures 4.5 show the muon energy resolutions at zenith angle (a) cos θ_z = 0.95 and (b) cos θ_z = 0.65, fitted with a function $\frac{p_0}{E^\alpha} + p_1 E$, where '$p_0$' represents the contribution from the multiple Coulomb scattering which is important at very low energies and 'p_1' is due to the error in position measurement which is important at high energies, where the bending is very small (leading to a larger error on sagitta measurement). The parameter 'α' takes a value of ~ 0.4 and between ~ 0.5 to ~ 0.6 for muons incident at zenith angles cos θ_z = 0.95 and cos θ_z = 0.65, respectively. Nevertheless, it was concluded that the resolution does not improve significantly in the energy range of 1 to 20 GeV by increasing the B-field from 1.5 to 1.8 T. As mentioned earlier, that mass hierarchy sensitivity of the ICAL detector at the INO arises from neutrinos of energies ~ few GeV.s. Hence a choice of 1.5 T B-field seems quite appropriate. On the other hand, a higher magnetic field may be obtained by increasing the current in the coils or using softer magnetic materials. This will increase the running cost of the detector with compelling justification in terms of better detector performance.

Further studies have been carried out by smearing the incident position of the muon in the entire volume of the detector. It was already seen from the magnetic simulation that the B-field is piecewise uniform over the surface of 16 m × 16 m area. Also there is a 50 % chance, that the track of muon is confined within the detector. These factors may deteriorate the energy resolution of the muon. Figure 4.6 shows the behavior of muon energy resolution at the magnetic field strengths of 1.1 T, 1.5 T and 1.8 T incident at fixed cos θ_z = 0.95 to 0.15. At a given magnetic field, the maximum additional deterioration of energy resolution is about 15 % compared to muons incident only in the central region of the detector.

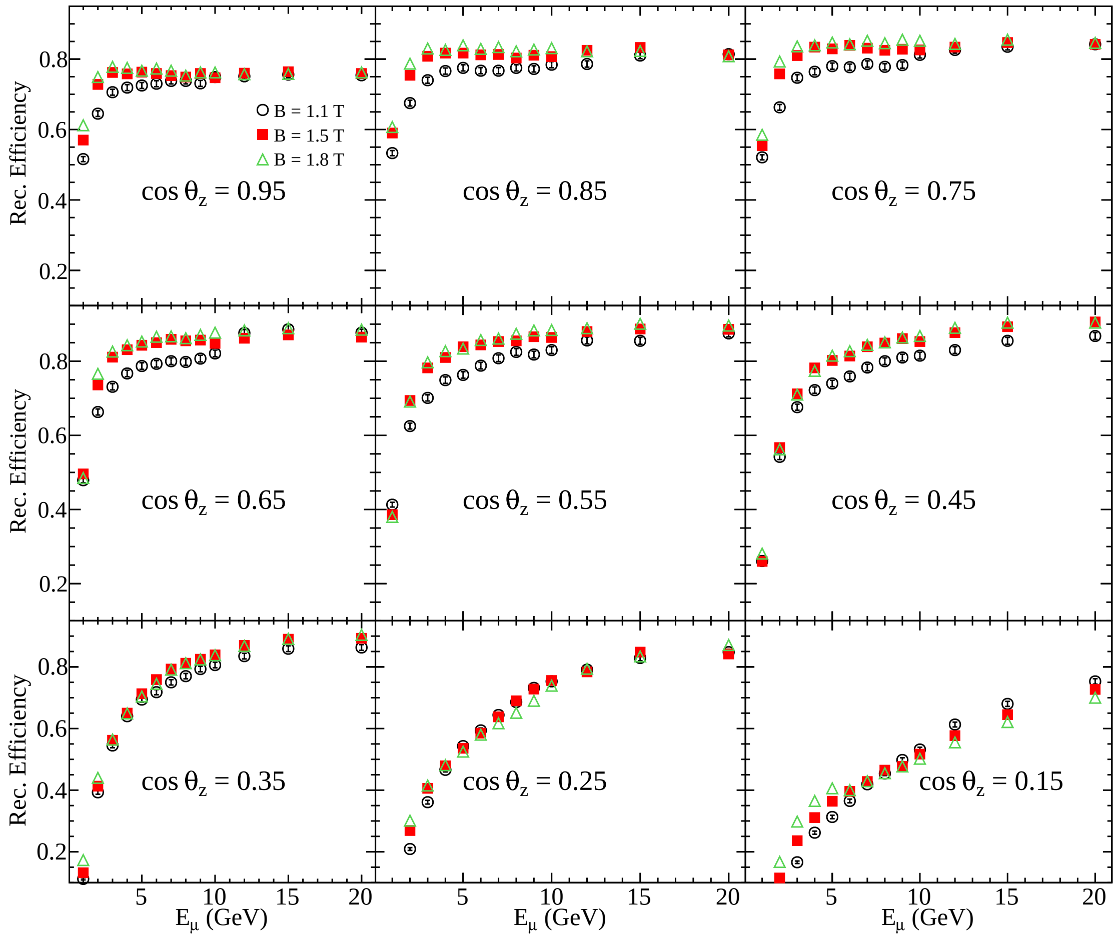

Figure 4.7: Comparison of reconstruction efficiency of muon at various zenith angles for B-field strengths of 1.1 T, 1.5 T, 1.8 T. The muon vertices are generated in the central part of the detector.

4 Effect of magnetic field strength on charge identification efficiency

The ICAL detector has the potential to identify the charge of (anti-) muons due to the magnetized iron, which will help to distinguish anti-neutrino and neutrino events. The main advantage of this property is to reduce the systematic uncertainty of the detector helping in the determination of the mass hierarchy of neutrinos. In the magnetized ICAL detector, the charge of muon will be determined from the curvature of its track. The charge identification (CID) efficiency of the detector defines as the ratio of rightly charged identified particles from the total number of reconstructed muons. It is expressed as,

$$\text{CID efficiency } (\eta) = \frac{N_{cid}}{N_{rec}}\,, \tag{4.16}$$

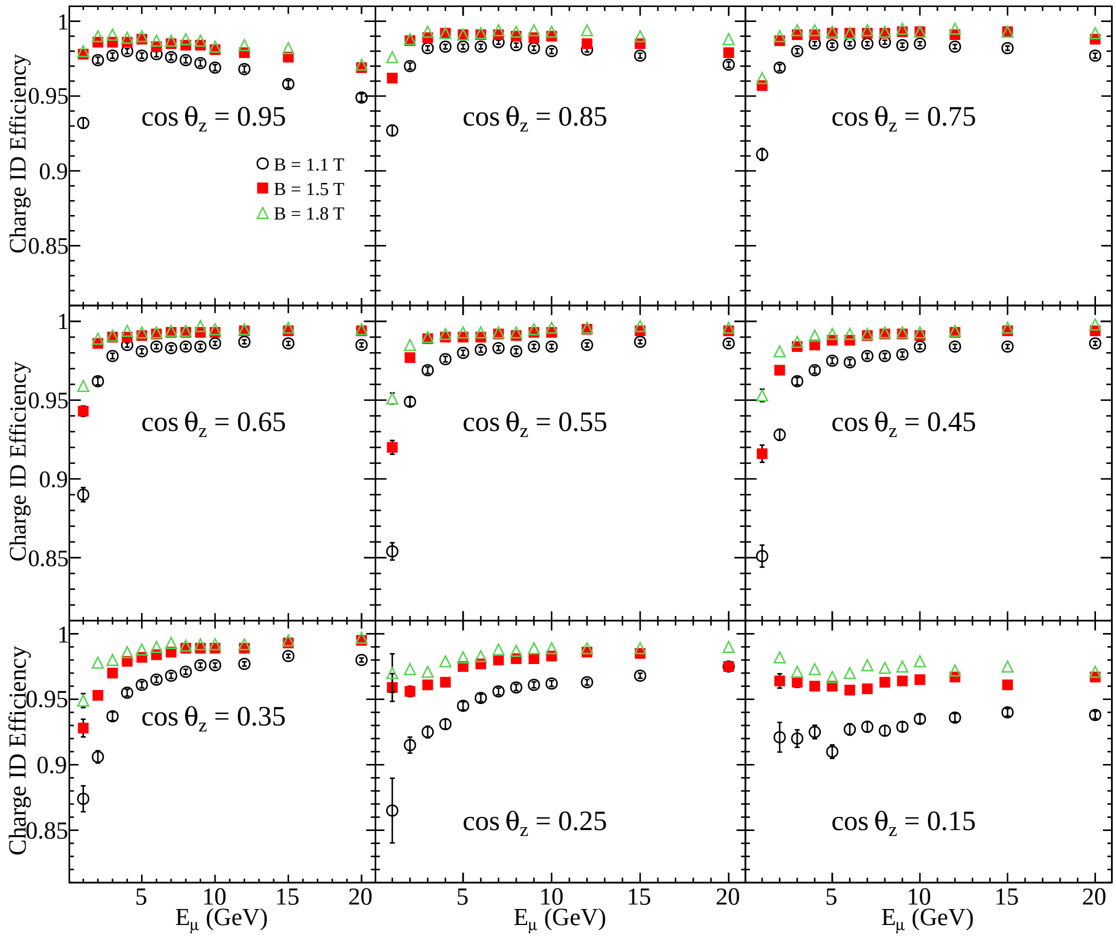

Figure 4.8: Comparison of charge identification (CID) efficiency with zenith angle for B-field strengths of 1.1 T, 1.5 T, 1.8 T. The muon vertices have been generated in the central part of the detector.

where 'N_{cid}' represents the number of rightly charged identified events and 'N_{rec}' is the number of reconstructed events from the incident muons. The error on the efficiency ($\delta\eta$) is expressed as follows,

$$\delta\eta = \sqrt{\eta\,(1-\eta)\,/\,N_{rec}}\,, \tag{4.17}$$

where the fraction, '(1-η)', comes from the identification of wrong sign charged muons. The magnetic field strength dependent reconstruction efficiencies are shown in Fig. 4.7. It can be seen that, at lower energy *i.e.* E_μ < 2 GeV, the reconstruction efficiency of the detector varies from 20 % to 60 % for cos θ_z = 0.95 to 0.15. Also at a given magnetic field, the reconstruction efficiency of the detector is ~ 80 % for cos $\theta_z \geq 0.55$, at energy, $E_\mu \geq 2$ GeV. The reconstruction efficiency increases by about 5 % for an increase in the magnetic field from about 1.1 T to 1.5 T and thereafter it saturates. Figure 4.8 shows the variation

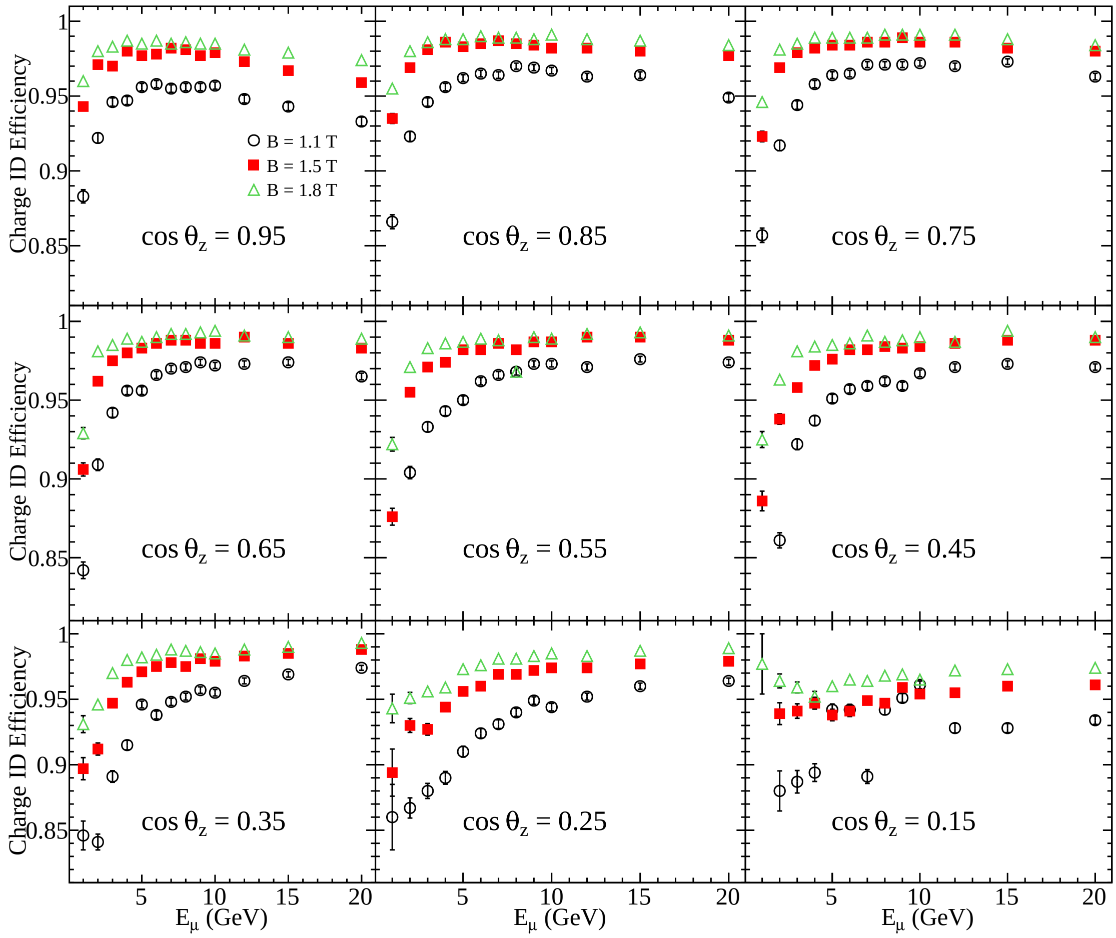

Figure 4.9: Comparison of CID efficiencies vs zenith angles for B-field strengths of 1.1 T, 1.5 T, 1.8 T. The muon vertices are smeared over the entire ICAL volume.

of charge identification efficiencies of muons with energy at various strengths of the magnetic field. For a given magnetic field, the muon CID efficiency at low energy is affected by the multiple Coulomb scattering while traveling through the detector which may lead to an incorrectly reconstructed direction of bending and resulting in wrong charge identification. At high energy, the CID efficiency is almost the same (∼ 98 - 99 %) and the effect of the multiple Coulomb scattering is smaller. At the magnetic field ∼ 1.1 T, the CID efficiency is relatively lower (∼ 96 %), as there is less bending compared to higher magnetic field of 1.5 - 1.8 T (see Fig. 4.4). A similar behaviour for charge identification efficiency with the magnetic field has been observed for the zenith angle range of cos θ_z between 0.95 and 0.15 as for the reconstruction efficiencies.

In an actual experiment, neutrinos may come from any direction and will interact at any part of the detector volume. Hence, it is important to study the charge identification efficiency of the muon considering the entire volume of the detector. It has been observed

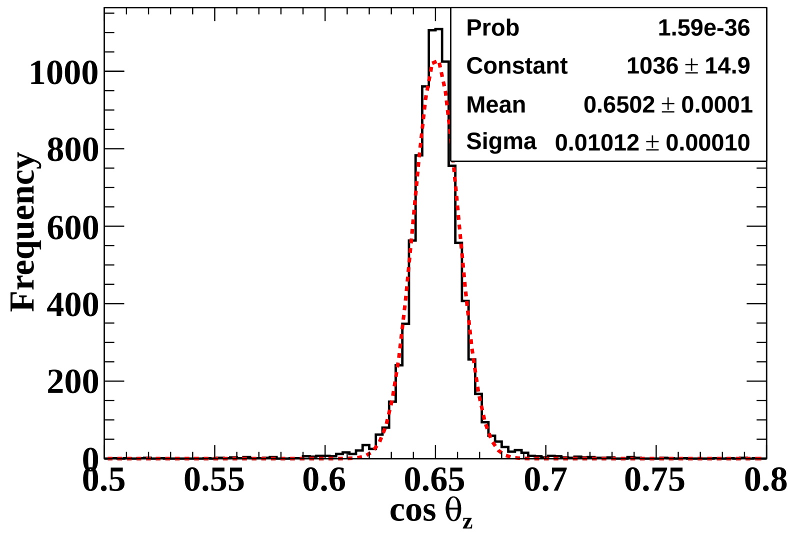

Figure 4.10: Reconstructed zenith angle distribution. The red dashed line shows the Gaussian fit of the distribution.

that, the charge identification efficiencies of muons incident at cos θ_z = 0.95 to 0.15, improve with increase in the magnetic field as shown in Fig. 4.9. However, it has been found that, at a given energy and magnetic field strength, the efficiency degrades by about 2 %, when the muon originates anywhere in the entire volume of the detector rather than only in the central volume, where the magnetic field is almost uniform. This is due to loss of efficiency for muon momentum reconstruction for events originating close to the detector periphery and also due to the those muons that experience a small average B-field on the 4 corners and around x = 8 m at y = 0 m and x = 8 m at y = 16 m.

5 Effect of magnetic field on zenith angle resolution

To measure the neutrinos squared mass difference, Δm^2, more precisely, it is important to reconstruct the incoming direction of the atmospheric neutrinos while estimating the source to detector distance (in addition to energy). In case of atmospheric neutrinos, the source to detector distance is a function of zenith angle and is expressed as,

$$L = \sqrt{(R_E + h)^2 - (R_E \, sin\, \theta_z)^2} - R_E \, cos\, \theta_z, \tag{4.18}$$

where 'R_E' is radius of the Earth, 'h' is the height where the neutrinos are produced and 'L' is the distance traveled by neutrinos to reach the detector. The incoming direction of the muon-neutrinos will be inferred from the measured track of the corresponding muon produced in a CC neutrino-nucleon interaction in the ICAL. The events distribution as a function of the reconstructed cos θ_z is shown in Fig. 4.10 for muons having energy 5 GeV incident at a fixed zenith angle of cos θ_z = 0.65 and B-field of 1.5 T. The zenith angle resolution has been obtained from the width of the Gaussian p.d.f while fitting the reconstructed zenith angle. It has been found that the mean of the distribution almost matches with the input and shows a good angular resolution for muons. The angular

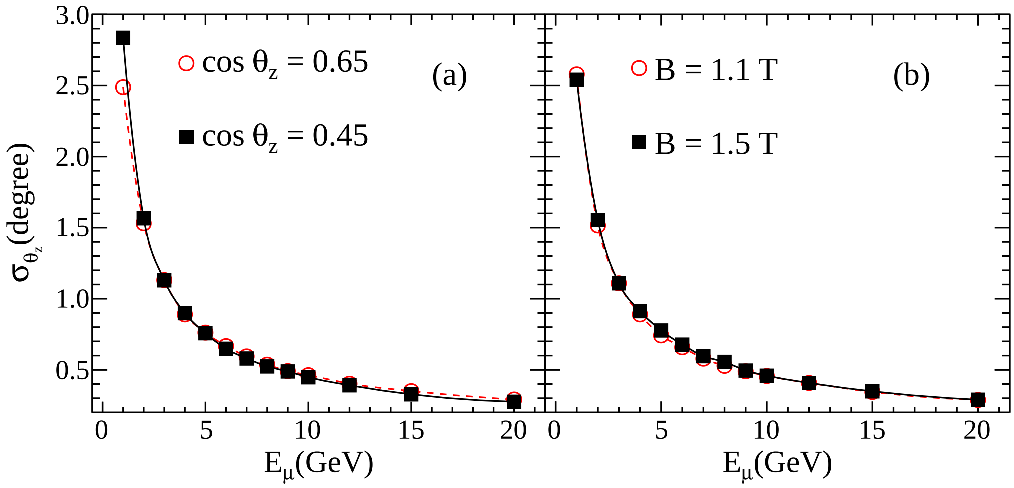

Figure 4.11: Zenith angle resolution vs energy at (a) two different zenith angles with B = 1.5 T and (b) for various magnetic field strengths at cos θ_z= 0.65.

resolution variation with muon energy, at a B-field of 1.5 T, for zenith angles given by cos θ_z = 0.45 and 0.65 is shown in Fig. 4.11 (a). It shows that the resolution is less than 1° for energy greater than about 4 GeV. At low energy, the poorer resolution is mainly because of multiple Coulomb scattering. The variation of angular resolution with energy for a given zenith angle, cos θ_z = 0.65, is almost independent of the strength of B-field as shown in Fig. 4.11 (b). This is due to the angle of incident particles that has been reconstructed using hits point obtained from first two layers of the ICAL detector.

In conclusion the detector response to muons improves with increase of the magnetic field and in particular a B-field of about 1.5 T seems to be optimal. This response of the magnetised ICAL to muons will be used to study the sensitivity to the atmospheric neutrino oscillation parameters but also other experimental investigations such as the possible muon pair decay of dark matter particles [123].

Chapter 5

Active-Sterile Neutrino Mixing Sensitivity of the ICAL at the INO

In this Chapter, the study of the sensitivity of the ICAL detector at the INO for active-sterile neutrino mixing parameters at an exposure of 1 Mton-yr has been described. Results of an initial study were reported in Ref. [109] where the analysis was performed in terms of the neutrino energy and zenith angle, assuming fixed values of detector resolutions and efficiencies. In this work, a similar but a more extensive study has been carried out. In contrast to only downward-going neutrino events used in Ref. [109], in the present analysis, the upward-going neutrino events including Earth matter effects are considered. Initially, the behavior of oscillation probabilities for both the 3 and the 3 + 1 generation neutrinos are presented. In the following section, the simulation technique adopted to estimate the number of oscillated events is described. Results of the inclusion of the detector resolution and efficiency on the raw neutrino events (without and with oscillations) are then presented. The effect of detector response on oscillation probabilities will also be discussed. Next, a brief discussion will be made on the binning scheme and the statistical procedure followed for studying the sensitivity of sterile neutrino mixing. Finally, results based on this study will be presented in detail.

1 Oscillation Probabilities for 3 and 3 + 1 Generation Neutrinos

The neutrino induced muon events are ideally suited for the measurement using the ICAL detector at the INO. Both the disappearance ($P_{\mu\mu}$) and appearance ($P_{e\mu}$) neutrino oscillation channels contribute to these events. The list of mixing parameters used in this work is given in Table 5.1. It is to be noted that while doing the analysis normal mass hierarchy of neutrinos has been considered. Figure 5.1 shows the neutrino oscillation probabilities $P_{\mu\mu}$ for downward-going (top panel, *i.e.* $\cos\theta_z^\nu = 1.0$, θ_z^ν is the zenith angle of incoming neutrino) atmospheric (a) muon neutrinos (ν_μ) and (b) muon antineutrinos ($\bar{\nu}_\mu$). It shows that a downward-going neutrino, in a 3 generation scenario, does not show the effect of oscillation (black line). This is due to the small path length of about 15 km considering either of the neutrino squared mass difference of Δm^2_{21} and Δm^2_{31}. On the other hand, the 3 + 1

Table 5.1: Neutrino oscillation parameters used for studying active-sterile neutrino mixing. NH: normal mass hierarchy of neutrinos, δ_{CP}: Dirac CP violation phase factor.

Parameters	Values
$\sin^2\theta_{12}$	~ 0.31
$\sin^2\theta_{23}$	~ 0.5
$\sin^2\theta_{13}$	~ 0.027
Δm^2_{21}	7.5×10^{-5} eV^2
Δm^2_{31} (NH)	2.4×10^{-3} eV^2
δ_{CP}	0.0

generation neutrinos show a dip in oscillation probabilities at an energy about 2 GeV (red line) for $\Delta m^2 = 0.1$ eV^2, which is much larger than Δm^2_{21} and Δm^2_{31} and suggested by the LSND and other experiments. This behavior is the same for neutrinos and antineutrinos since all CP phases are set to be zero and only vacuum oscillations have been considered. The dip which comes from active-sterile mixing may be used to constrain the sterile neutrino parameters. The bottom panel (upward-going, $\cos\theta_z^\nu$ = -1.0 for (c) ν_μ, (d) $\bar{\nu}_\mu$) shows the oscillation probability as a function of energy for 3 and 3 + 1 generations. The matter effect, for neutrinos traversing the Earth, affects the oscillation probability for both 3 and 3 + 1 generations. The PREM density profile of the Earth [124] is used to calculate the matter effect on the oscillation probability. Due to the large Δm^2_{41}, the 3 + 1 generations plot shows a rapid oscillation. To see the rapid oscillation pattern, the detector needs to have very good energy and angular resolution. The probabilities of oscillation, $P_{e\mu}$, for downward-going (top panel, cos θ_z^ν = 1.0) and upward-going (bottom panel, cos θ_z^ν = -1.0) (anti)neutrinos as a function of energy for 3 and 3 + 1 generations are shown in Fig. 5.2. It shows that $P_{e\mu}$ = 0 for downward-going (anti)neutrinos. In case of upward-going neutrino, both 3 and 3 + 1 generation show the oscillation behavior due to the matter effect. On the other hand, the anti-neutrinos show a negligible effect of oscillation for the normal mass hierarchy.

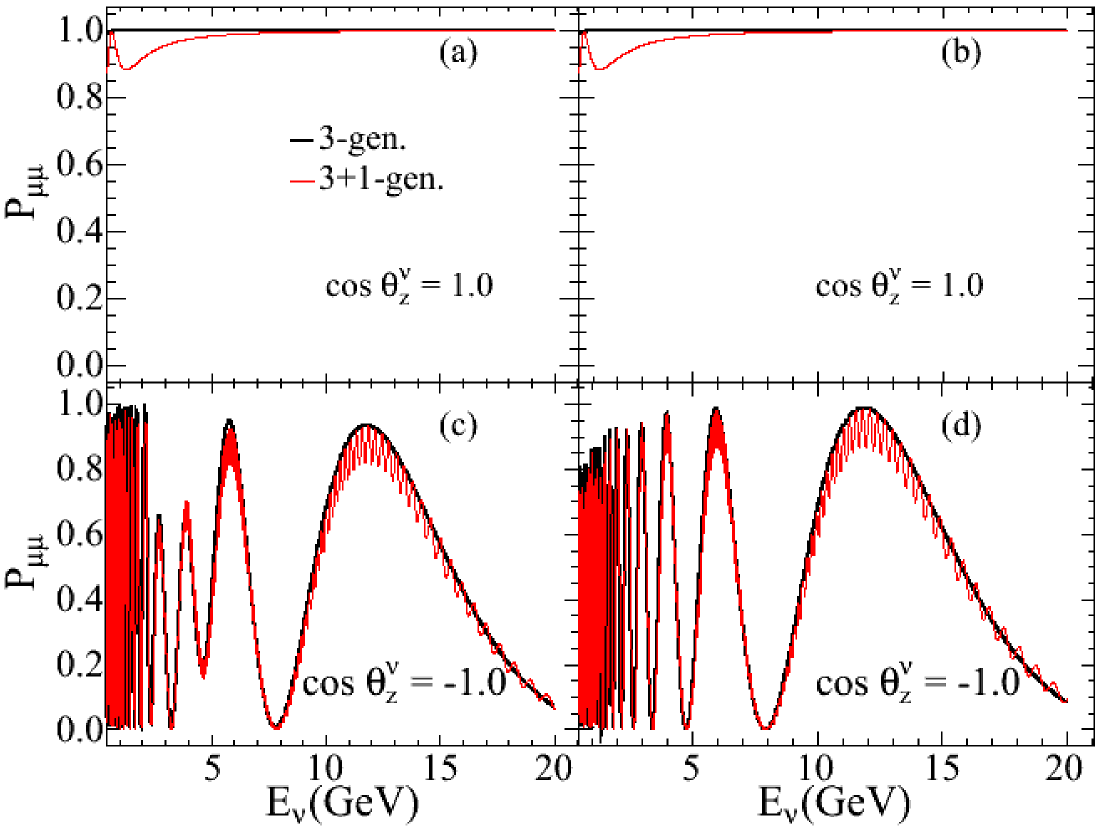

Figure 5.1: Comparison of the survival probability for neutrinos (left-hand panels) and anti-neutrinos (right-hand panels) for 3 (black line) and 3 + 1 (red line) generations, as a function of (anti)neutrino energy. The top panels are for $\cos\theta_z^\nu$ = 1.0 (downward-going neutrinos) while the bottom panels are for $\cos\theta_z^\nu = -1.0$ (upward-going neutrinos). The active-sterile oscillation parameters assumed for all panels are $\sin^2\theta_{24}$ = 0.03 , $\sin^2\theta_{14} = \sin^2\theta_{34} = 0$, Δm^2_{41} = 0.1 eV^2.

Figure 5.3 shows oscillation survival, $P_{\mu\mu}$ (bottom panels) and appearance $P_{e\mu}$ (top panels) probabilities for 3 and 3 + 1 generations, as a function of (anti)neutrino energy at path lengths of 7000 km and 10000 km. The values of 3 + 1 generation neutrino oscillation parameters chosen to generate these plots are given in the figure caption. The black line shows the plot for 3 generation and red, green and blue lines represent 3 + 1 generation neutrinos considering the Earth matter effect. The effect of active-sterile neutrino mixing

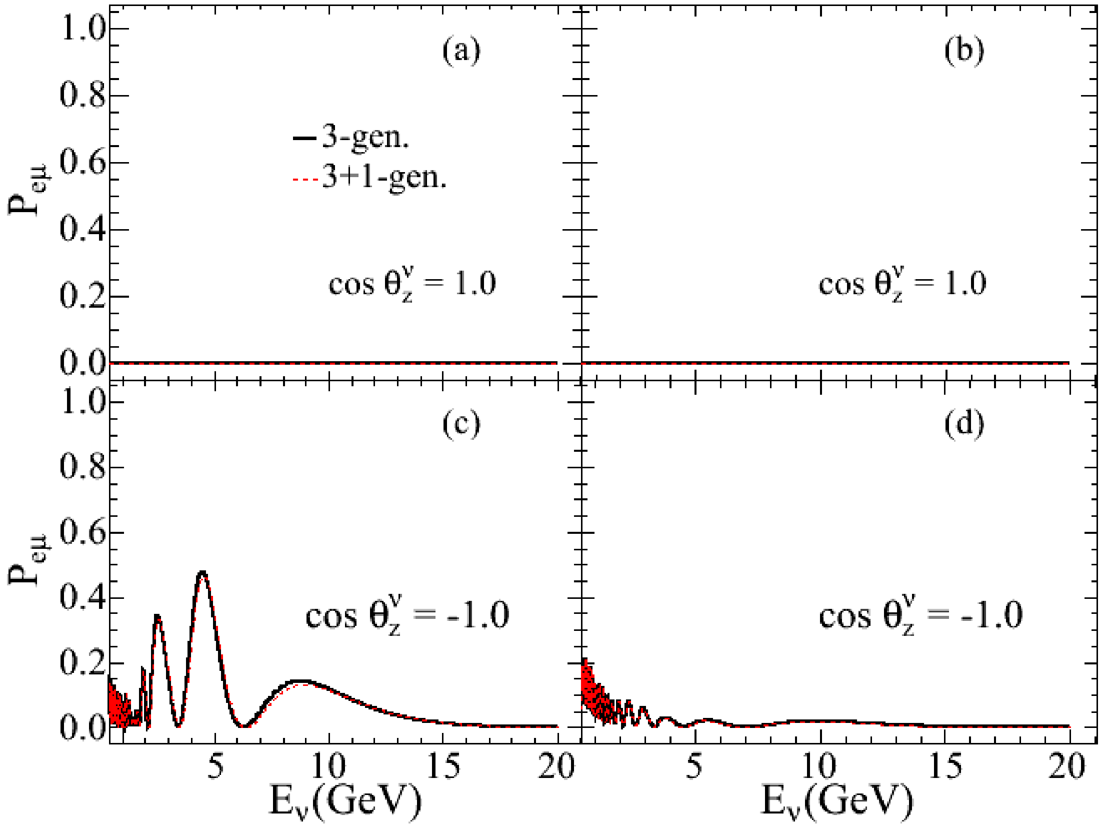

Figure 5.2: Comparison of the appearance probability for muon neutrinos starting from electron neutrinos (left-hand panels) and anti-neutrinos (right-hand panels) for 3 (black line) and 3 + 1 (red line) generations, as a function of (anti)neutrino energy. The top panels are for $\cos\theta_z^\nu = 1.0$ (downward-going neutrinos) while the bottom panels are for $\cos\theta_z^\nu = -1.0$ (upward-going neutrinos). The active-sterile oscillation parameters assumed for all panels are $\sin^2\theta_{24} = 0.03$, $\sin^2\theta_{14} = \sin^2\theta_{34} = 0$, $\Delta m^2_{41} = 0.1$ eV^2.

starts becoming apparent after the inclusion of θ_{14} in the appearance channel P$_{e\mu}$. Both the oscillation probabilities, P$_{e\mu}$ and P$_{\mu\mu}$, with inclusion of θ_{34}, show a shift in the position of the maxima or minima compared to 3 generation as well as for 3 + 1 generation with inclusion of only θ_{24} and both θ_{14} and θ_{24}, respectively. It may be noticed from the figure that while any sterile mixing changes the neutrino oscillation probabilities, the impact of θ_{34} appears to be most dramatic and changes the shape of the oscillation probabilities. Figure 5.4 shows the probability of conversion of active (anti)neutrino to sterile for both down going (green line) and upward-going(red line) neutrinos. It shows in both (anti)neutrino to sterile neutrino conversion, the rapid oscillation comes for upward-going neutrinos due to the Earth matter effect.

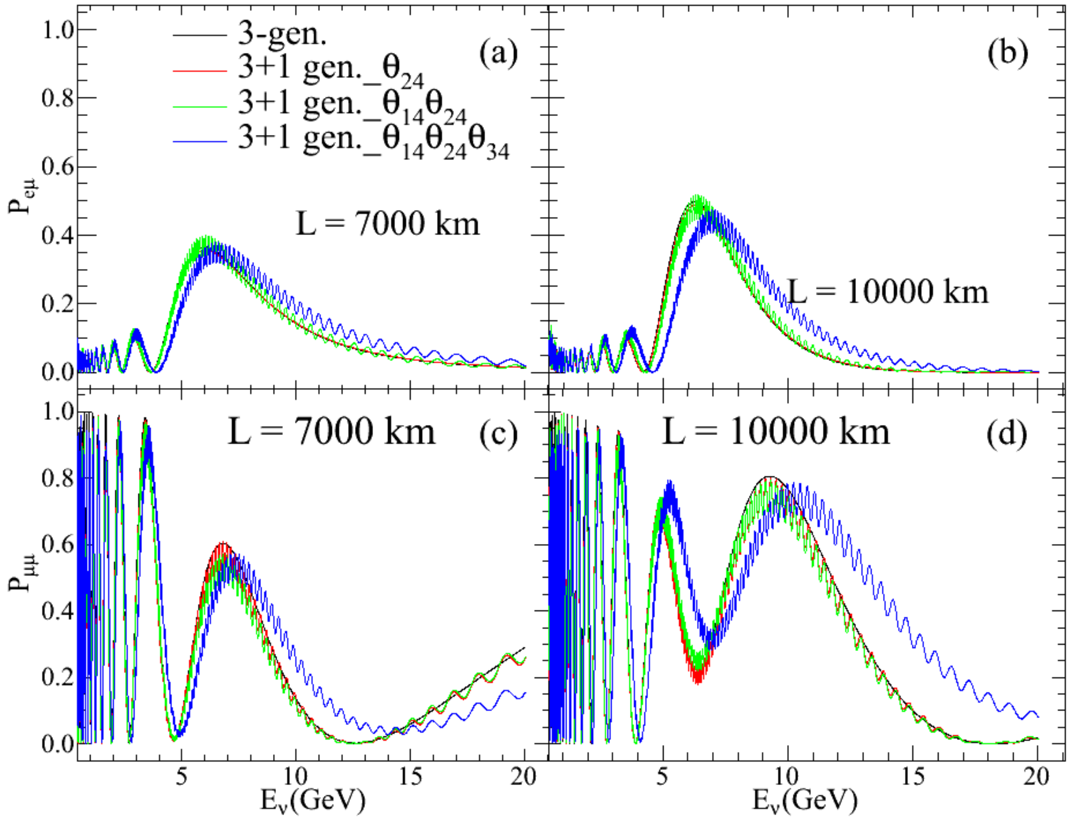

Figure 5.3: Oscillation probabilities $P_{e\mu}$ (top panels), and $P_{\mu\mu}$ (bottom panels) for the 3 (black lines) and 3 + 1 generations as a function of neutrino energy. The red, green, blue lines correspond to the oscillation probability at mixing angles θ_{24}, θ_{14} and θ_{24}, θ_{14},θ_{24} and θ_{34} respectively, for 3 + 1 generation. The active-sterile oscillation parameters assumed for all panels are $\sin^2\theta_{14} \sim 0.022$, $\sin^2\theta_{24} \sim 0.03$, $\sin^2\theta_{34} \sim 0.21$, $\Delta m^2_{41} = 1.0$ eV^2.

2 Simulation Technique

2.1 Reweighting Algorithm

Atmospheric neutrino events are generated using NUANCE [125], the neutrino event generator, appropriately modified for the ICAL detector by the INO collaboration. Here the oscillation probability part of the code has been switched off. In this analysis, an acceptance-rejection method has been applied to estimate the number of oscillated events. In order to do this, the oscillation probabilities are calculated using the 3-generation oscillation formalism considering the true energy and zenith angle of neutrinos. Next, the oscillation probabilities are compared with a uniform random number, $R(0, 1)$. In the case of oscillation of the muon neutrino ν_μ, the sum of probabilities of oscillation necessarily

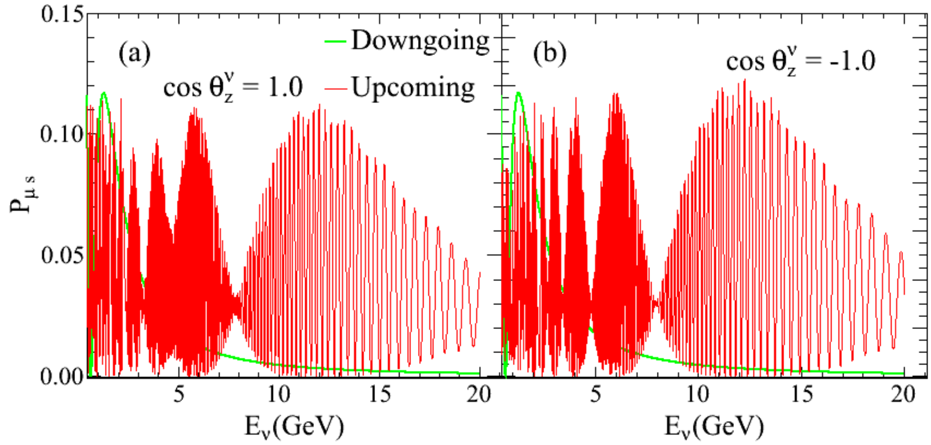

Figure 5.4: Comparison of the oscillation probability for $\nu_\mu \to \nu_s$ (left-hand panel) for downward-going (green line) and upward-going (red line) and $\bar{\nu}_\mu \to \bar{\nu}_s$ (right-hand panel), as a function of (anti)neutrino energy. The left panel are for $\cos\theta_z^\nu = 1.0$ (downward-going neutrinos) while the right panel are for $\cos\theta_z^\nu = -1.0$ (upward-going neutrinos). The active-sterile oscillation parameters assumed for all panels are $\sin^2\theta_{24} = 0.03$, $\sin^2\theta_{14} = \sin^2\theta_{34} = 0$, $\Delta m^2_{41} = 0.1$ eV^2.

obeys the equation $P_{\mu e} + P_{\mu\mu} + P_{\mu\tau} = 1$[1], where $P_{\mu e}$, $P_{\mu\mu}$ and $P_{\mu\tau}$ are oscillation probabilities for the ν_μ to ν_e, ν_μ and ν_τ, respectively. If $R < P_{\mu e}$, then it is assigned to ν_e type event. If $R > (P_{\mu e} + P_{\mu\mu})$, then it is treated as the ν_τ event. On the other hand, if $P_{\mu e} \leq R \leq (P_{\mu e} + P_{\mu\mu})$, then it is considered as the ν_μ survival event.

Also the number of muon events in the detector from the appearance channel $\nu_e \to \nu_\mu$ has been estimated. In this case, the atmospheric neutrino flux and the ν_μ charged current interactions are used in estimating the muon events. Further the oscillation probability has been compared with random number, $S(0, 1)$, and, if $S < P_{e\mu}$, then it is taken as an oscillated ν_μ event. The total number of muon events are estimated by adding events from the "disappearance" and the "appearance" oscillation channels. A similar procedure has been adopted for events due to anti-neutrinos. The incorporation of the detector response on these raw events will be described in the next section.

[1] which is true for other active flavours

2.2 Implementation of Detector Response

2.2.1 On The Neutrino Induced Events

Although atmospheric neutrinos come in all three flavours *viz* : ν_e, ν_μ and ν_τ, the magnetized ICAL detector is best suited for the measurement of the muon neutrinos because of the excellent tracking capability of the associated muons produced through the charged current (CC) interactions of ν_μ. A measurement of ν_e in ICAL is not possible due to the large iron plate thickness (5.6 cm) compared to the radiation length of iron ($\sim$ 1.76 cm). The production of the τ-lepton due to the charged current interaction of the ν_τ is also small because of high threshold for the tau production (about 4 GeV). In addition to the muon, the ICAL will also measure the energy of the hadron(s) for the same CC induced neutrino event. There are three main processes that contribute to the CC interactions in the ICAL detector. At sub-GeV energies of neutrinos, the quasi-elastic process dominates, where the final state muon carries most of the available energy and the recoiling nucleon carries very little energy. As the energy increases from sub-GeV to multi-GeV, hadrons and their showers are produced in resonance (RS) and deep-inelastic scattering (DIS) processes. In the RS process, the final state hadron shower mostly consists of a single pion, though multiple pions may contribute in a small fraction. The DIS process produces multiple hadrons, which carry a large fraction of the incoming neutrino energy. Due to the CC interaction of the neutrino, for every hadron shower, there is a corresponding muon coming from the same interaction vertex. So the true hadron energy, $E_h = E_\nu - E_\mu$, where E_ν is the true energy of the incoming neutrino and E_μ is the true energy of the muon which is obtained from the NUANCE event generator. In the detector, the energy and angular resolutions depend on particle types, energies and their incident directions. At low energy (E $<$ 0.9 GeV), the energy loss of the muon in the detector follows a Landau probability distribution function (p.d.f), P_L, and, above this it is accurately described by a Gaussian p.d.f, P_G. The detector responses are incorporated for the true events of the neutrino induced muon and hadron.

The muon and hadron response of ICAL in terms of the muon energy and zenith angle resolution and the hadron energy can be implemented in several ways such as:

- The raw NUANCE generated events can pass through the detector on a MC basis (MC-I). This incorporates all the properties of the detector *viz.* the energy and the angle resolution, the reconstruction and charge identification efficiencies.

- In another method, events can be folded with the detector response on a MC basis (MC-II), which is obtained from the GEANT4 simulation of the ICAL detector for the muon and the hadron. The procedure followed to obtain the momentum response of the muon using the ICAL detector at the INO has been described in Chapter 3 and in Ref. [126]. To incorporate the energy resolution for the muons, both P_L and P_G p.d.f, are used for reconstructing the final energy. The mean of the function is used as the true E_μ for the muon energy obtained from the NUANCE neutrino event generator. After incorporating the resolutions using the MC method, the final energy is as follows,

$$E^r_\mu = P_L(E_\mu, \sigma_{E_\mu}), E_\mu < 0.9\,\mathrm{GeV} \tag{5.1}$$

$$E^r_\mu = P_G(E_\mu, \sigma_{E_\mu}), E_\mu \geq 0.9\,\mathrm{GeV} \tag{5.2}$$

where σ_{E_μ} is the standard deviation of energy and E^r_μ is the reconstructed energy of the muon. Similarly, to incorporate the energy dependent zenith angle resolution for the muon incoming direction, the probability distribution, P_G, has been used irrespective of energy, which is as follows

$$cos^r\theta_z = P_G(cos\ \theta_z, \sigma_{cos\theta_z}), \tag{5.3}$$

where $\sigma_{cos\theta_z}$ is the standard deviation of the cosine of the zenith angles and $cos^r\theta_z$ is the reconstructed cosine of the zenith angle for the muon.

- In addition to the above methods, the functional integration method may be also used to incorporate the detector response for neutrino induced true events. The details of the procedures are as follows,

$$N^r_{ij} = \sum_k \sum_l K^k_i(E^k_T) M^l_j(cos\theta^l_T) n_{kl} \tag{5.4}$$

with

$$K^k_i = \int_{E_{L_i}}^{E_{H_i}} dE \frac{1}{\sqrt{2\pi\sigma^2_E}} e^{-\frac{\left(E^k_T - E\right)^2}{2\sigma^2_E}} \tag{5.5}$$

$$M^l_j = \int_{cos\theta_{L_j}}^{cos\theta_{H_j}} dcos\theta \frac{1}{\sqrt{2\pi\sigma^2_{cos\theta}}} e^{-\frac{\left(cos\theta^l_T - cos\theta\right)^2}{2\sigma^2_{cos\theta}}} \tag{5.6}$$

where E_T, cosθ_T are the true (kinetic) energy and the zenith angle of the muon respectively, E and cosθ are the corresponding reconstructed muon energy and cosine of zenith angle, respectively, after incorporating the detector angle and energy resolution. The indices i, j correspond to the measured energy and zenith angle bins and N^r_{ij} correspond to the number of reconstructed events, k, l are summed over the true energy and zenith angle of the muon and n_{kl} is the number of events in k^{th} and l^{th} true energy and zenith angle, respectively.

- Similarly, the hadron energy resolution has been incorporated on the MC basis using the Vavilov p.d.f and the method followed is given in Ref. [127].

It may be noted here that the method MC-II has been used while studying the active-sterile neutrino mixing sensitivity. Further, the detector reconstruction and charge identification efficiencies for the muon are incorporated in the simulation. The number of reconstructed events after incorporating the detector efficiencies are given by,

$$N^f = N^r_{\mu^-} \times \epsilon^r_{\mu^-} \times \epsilon^{cid}_{\mu^-} + N^r_{\mu^+} \times \epsilon^r_{\mu^+} \times (1 - \epsilon^{cid}_{\mu^+}) \tag{5.7}$$

where $\epsilon^r_{\mu^-}$, $\epsilon^r_{\mu^+}$ are the reconstruction efficiencies, $\epsilon^{cid}_{\mu^-}$, $\epsilon^{cid}_{\mu^+}$ are the charge identification(cid) efficiencies of muons and antimuons respectively, N^f is the final number of reconstructed μ^- events. A similar procedure may be used to reconstruct the μ^+ events.

2.3 Event Reconstruction

Figure 5.5(a) shows a typical muon energy spectrum integrated over cos θ_z = 0.6 to 0.65 and energy range from 0 to 20 GeV. The black line shows the true muon events whereas the red dashed line corresponds to events after incorporating detector response. Both spectra are generated without considering the neutrino oscillation formalism. It may be seen that for the 0 - 1 GeV bin, the number of events reduces by $\sim$ 50 % after implementing detector resolution and those are further redistributed in higher energy bins. So after incorporating the detector response, the bins beyond 1.0 GeV have more events. The Landau p.d.f has been used for energy E_μ < 0.9 GeV. Due to the long tail, there are contributions to higher energy bins and the effect of a Gaussian distribution for the higher energy bins is not visible. The energy spectrum of events, after incorporating the detector response, with respect to true events is shown in the ratio plot at the bottom of Fig. 5.5 (a). Figure 5.5 (b) shows the hadron energy spectrum integrated over zenith angle from cos θ_z

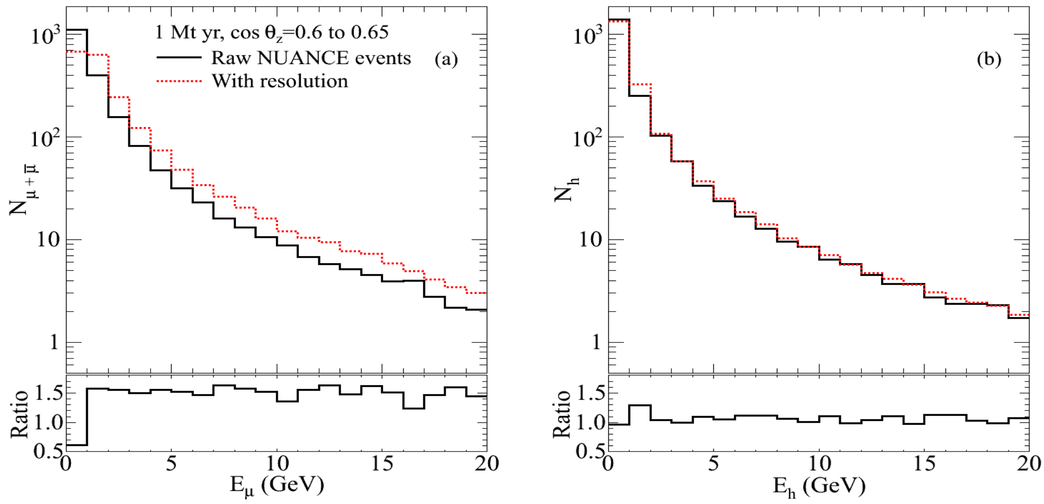

Figure 5.5: Comparison of events generated using NUANCE and incorporating the detector angle and energy resolution at 1 Mton-year integrated over the zenith angle bin of cos θ_z = 0.60 - 0.65. (a) Muon events versus energy (E$_\mu$), (b) Hadron events versus energy (E$_h$). Bottom panels show the ratio of events after and before incorporating the detector resolutions. The range for energy and cosine of zenith angle are true E$_\mu$ and cos θ_z and E$^r{}_\mu$ and cos^r θ_z, respectively before and after implementing the detector resolution.

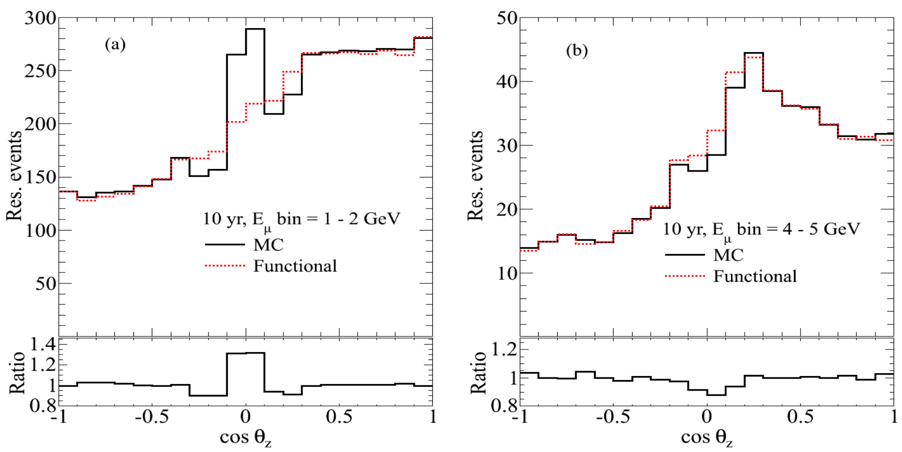

Figure 5.6: Zenith angle dependence of neutrino events after incorporating the detector resolution for muon energy and zenith angle using MC-II and functional integration method at energy bins of (a) E$_\mu$ = 1 - 2 GeV and, (b) E$_\mu$ = 4 - 5 GeV. In both cases the p.d.f, P$_G$ is used to smear the true events.

= 0.6 to 0.65 and the energy ranges from 0 to 20 GeV. The black line shows the distribution of raw events whereas the red dashed line shows the same events after incorporating energy resolutions of the detector using the Vavilov p.d.f. It is observed that some energy bins have more or less events after incorporating the detector resolutions except for the first energy bin (E$_h$ = 0 - 1 GeV) as shown in the ratio plot Fig. 5.5 (b). The behavior of

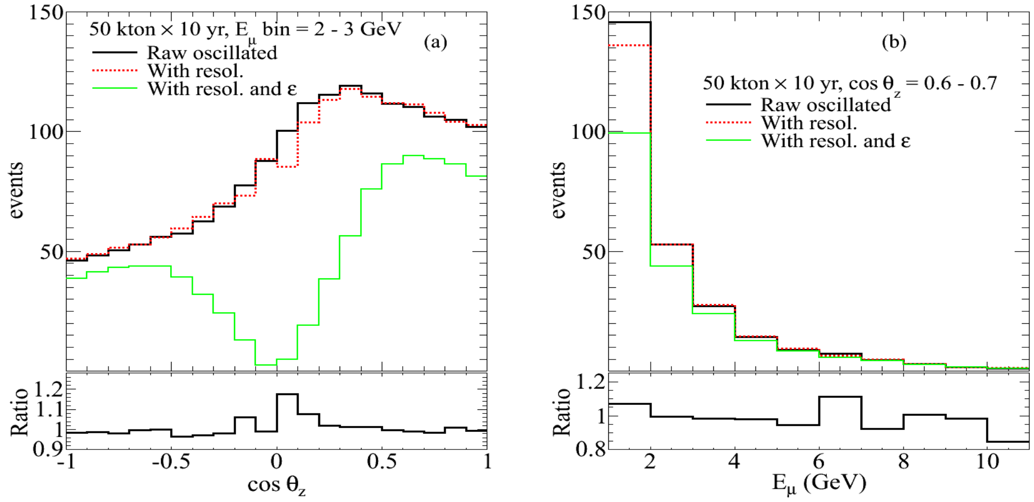

Figure 5.7: Oscillated events after incorporating detector response on the muon energy and zenith angle. The detector resolutions are incorporated using the method MC-II.

the energy spectrum in this range is similar to that of the muon. In this case, events are spilled over to other bins due to the tail of the Vavilov p.d.f.

Further, a comparative study has been carried out on the oscillated (3 generation oscillation probability was used) events after incorporating the detector response using the functional integration and MC-II methods at an exposure of 10 years as shown in Fig. 5.6. The black line shows the event distribution in which detector resolution has been incorporated using the method MC-II and the red dotted line is obtained using the functional integration method for the energy bins (a) E_μ = 1 - 2 GeV and (b) E_μ = 4 - 5 GeV. The ratio of oscillated events generated by the two methods is shown in the bottom panel of Fig. 5.6. It can be seen that for the energy of E_μ = 1 - 2 GeV plot, the maximum deviation occurs at the $\cos\theta_z$ = 0.0 bin. Both event spectra agree with each other for the energy bin of E_μ = 4 - 5 GeV.

Figure 5.7 shows the oscillated (3 generation oscillation probability has been used) events without and with incorporation of the detector energy and zenith angle resolutions at an exposure of 10 years. The detector reconstruction and charge identification efficiencies are also incorporated for these events. In Fig. 5.7 (a), events are distributed in cos θ_z with a bin width of 0.1 for the energy bin of E_μ = 2 - 3 GeV. The black line shows the true (without incorporating detector response) oscillated events distribution. It may be seen that the number of upward-going (cos θ_z < 0) events are less that the downward-going ones (cos θ_z > 0). The probability of oscillation changes due to the Earth matter effect for

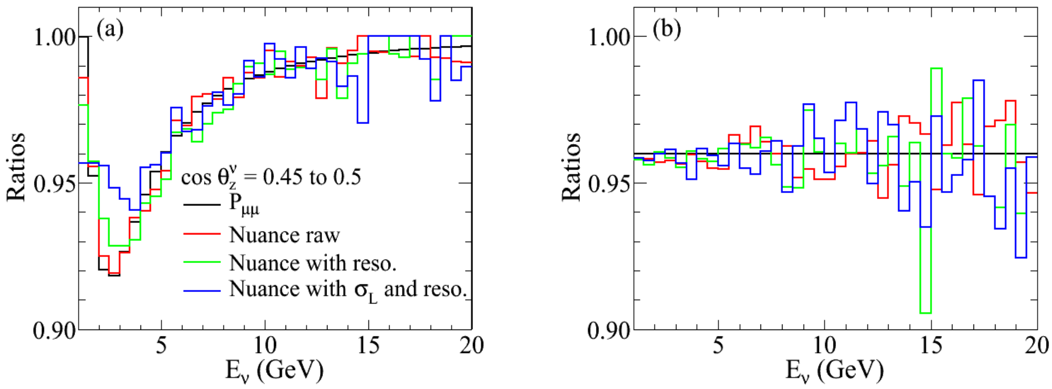

Figure 5.8: The ratio of oscillated to "without oscillations" events as a function of the energy, integrated over cos θ_z bin 0.40 to 0.45 at (a) Δm^2_{41} = 0.1 eV^2 and, (b) Δm^2_{41} = 10.0 eV^2 at neutrino mixing angle of $\sin^2 2\theta_{\mu\mu}$ = 0.083. Black line shows the plot using 2-ν oscillation formula (theory), red line shows the plot obtained using reweighted algorithm from NUANCE events without implementing the detector response, green line shows the plot after implementing the detector response with σ_{E_ν} = 0.15 E$_\nu$ and σ_{θ_z} = 10°, blue line shows the plot with detector response as well as considering the production height distribution of neutrinos.

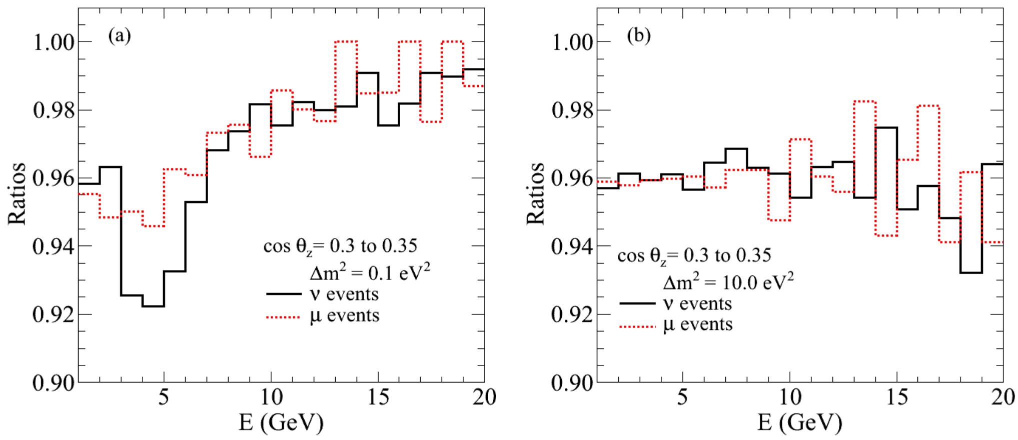

Figure 5.9: The ratio of muon events as a function of energy with and without neutrino oscillations integrated over cos θ_z bin 0.30 to 0.35 for the neutrino mixing angle $\sin^2 2\theta_{\mu\mu}$ = 0.083 at (a) Δm^2_{41} = 0.1 eV^2 and, (b) Δm^2_{41} = 10.0 eV^2.

upward-going neutrinos. The red dotted line shows the event distribution after incorporating the detector energy and angle resolutions. It can be seen that the reconstructed events spill over to the neighboring bins. The green line shows the events after incorporating resolution as well as both the reconstruction and the charge identification efficiencies. The reduction in number of events for cos $\theta_z \sim 0$ is due to the poor reconstruction efficiency of the detector. Similarly, the event distribution with energy for a given zenith angle bin, cos θ_z = 0.6 - 0.7, is shown in Fig. 5.7 (b).

2.3.1 Effect on the Oscillation Probabilities

After incorporating the detector response on the neutrino induced true events, further studies are carried out to see the effect of the detector response on oscillation probabilities *i.e.* the ratio of events with and without oscillations. For that the INO collaboration has generated a 1000 years data set in order to reduce the statistical fluctuations, which are further normalized to the required exposure during the statistical analysis. An exposure of 1 Mton-yr has been considered in this study. Thereafter, events are made to oscillate using a reweighting algorithm discussed in Section 2.1. While estimating oscillated events, the ν production height distribution in the atmosphere has been considered, which is a function of the zenith angle, and the energy of neutrino as in Ref. [128]. The path length (L) distribution has been incorporated on the MC basis by considering Gaussian smearing of the path length whose mean is 'L' and the corresponding zenith angle and energy dependent standard deviation (σ_L) are given in Table 5.2. Here, it may be noted that the production height distributions are considered for the downward-going neutrinos only. The oscillated events are then distributed two dimensionally in the muon energy and zenith angle bins. The analysis on the active-sterile neutrino mixing has been carried out separately considering only downward-going neutrinos as well as when they come from all directions to reach the detector. In the latter case, the Earth matter effect has been considered while estimating the oscillation probabilities. It may be noted here that the CP violation phase factor has been assumed to be zero in this study. Hence the oscillation probability for neutrino and antineutrinos are the same. Further, the analysis has been divided in two parts, considering (a) only the muon energy and their zenith angle information and (b) combining the hadron energy along with the muon information. To select active-sterile oscillated events (considered as observed events), the 3 + 1 neutrino oscillation formalism has been used in the reweighted algorithm. Due to higher value of squared mass difference, the survival probability $\nu_\mu \rightarrow \nu_\mu$ based on the 3 + 1 neutrino oscillation formalism is reduced to the 1 + 1 form for downward-going neutrino as given in Subsec. 4.2 of Chapter 2.

To see the impact of detector resolutions on oscillation probabilities, fixed energy and angular resolutions are incorporated considering only the neutrino events. Figures 5.8 show the ratio of events with and without oscillations as a function of neutrino energy. The results are shown for the neutrino zenith angle bin $\cos\theta_z^\nu = 0.45 - 0.5$. Figure 5.8 (a) is for $\Delta m^2_{41} = 0.1$ eV^2 while Fig. 5.8 (b) is for $\Delta m^2_{41} = 10.0$ eV^2. The black lines show the survival probability $P_{\mu\mu}$ as a function of the neutrino energy obtained from the 1 + 1 neutrino oscillation formula. The red line shows the ratio of oscillated events generated using the reweighted algorithm to without oscillated raw events coming from the NUANCE. Note that the red lines follow the survival probability quite closely, within the MC fluctuations. The green lines are obtained by including a flat energy resolution where the $\sigma_{E_\nu} = 0.15E_\nu$ and angle resolution for which the $\sigma_{\theta_z^\nu} = 10.0°$ on the true neutrino events. The resolution functions bring a mild smearing of the shape of the event spectrum. Finally, the blue lines are obtained after smearing the production point in the atmosphere *i.e.* varying the source to detector distance, as well according to Table 5.2. The impact of this smearing is rather large when the data is sensitive to the phase of the Δm^2_{41} driven oscillations (left panel). Since the atmospheric neutrino production point is uncertain, which decides the path length, this causes an attenuation of the dip of the event spectrum due to active-sterile oscillations. While studying the ICAL detector sensitivity to sterile neutrino mixing, the actual resolutions of the detector obtained from INO look up tables for the neutrino induced muon [126] and hadron [127] are used.

In the ICAL detector at the INO the neutrino induced muon will be measured. So, for the same oscillation probabilities, the behavior of the ratios of the events with and without oscillations is shown in Fig. 5.9 for neutrinos and muons. The ratios vary with energy, integrated over a fixed $\cos\theta_z$ bin of width 0.30 to 0.35, at neutrino mixing angle of $\sin^2 2\theta_{\mu\mu}$ = 0.083 and squared mass difference of (a) $\Delta m^2_{41} = 0.1$ eV^2 and, (b) $\Delta m^2_{41} = 10.0$ eV^2. At the $\Delta m^2_{41} = 0.1$ eV^2, the black line shows the event ratios for neutrinos where the probability of oscillation has been calculated using their true energy and zenith angle. The red dashed line shows the event ratios due to muons, where the survival probabilities for the same are estimated using true energy and zenith angles of neutrinos. At the energy about 5 GeV, the dip in ratio reduces for muons due to the phase part *i.e.* $\sin^2\left(\frac{1.27\Delta m^2_{41} L}{E}\right)$ of the survival probability which is averaged out over the neutrino energy and zenith angle. In Fig. 5.9 (b), at the $\Delta m^2_{41} = 10.0$ eV^2, the effect is less visible, as at higher value of Δm^2_{41}, the phase part of the oscillation probability is already averaged out. Further analysis has been carried out by adding the hadron energy along with the muon information to find out the sterile neutrino sensitivity of the ICAL detector.

2.4 Binning Scheme

After incorporating the ICAL detector resolutions for the muon and the hadron, variable binning schemes are considered to constrain the mixing of active-sterile neutrinos. The

Table 5.2: Production height (slant distance in km) of neutrinos and its corresponding sigma for six values of cosθ_z for 3 neutrino energy bins [128].

cosθ_z	E = 0.3 - 2.0 [GeV]		E = 2.0 - 20.0 [GeV]		E > 20.0 [GeV]	
	L	σ_L	L	σ_L	L	σ_L
1.0	15.9	8.7	16.6	9.0	17.6	8.9
0.75	23.6	11.8	24.1	12.1	25.8	12.6
0.50	41.0	18.1	40.9	19.1	43.3	19.4
0.25	95.6	31.4	92.8	34.6	94.9	36.4
0.15	160.0	37.3	154.3	42.8	151.2	49.4
0.05	369.8	55.0	359.0	67.1	335.7	94.2

choice of the bin widths depend on two issues, (i) need for sizable number of events in each bin so that the bin width needs to be large and, (ii) also it is necessary to capture characteristic data signatures in the region of interest which points to a smaller sized bin. On the other hand, given a finite detector resolution, the smallest bin size must be less than or equal to the full width at half maximum of the spectrum. In the simulation, the bin content may be less than one, but in an experiment, the observed data in various bins should be greater than or equal to one. After considering all these factors, bins of various widths have been chosen in order to ensure that there is at least one event in each bin. In the analysis, events are distributed in two dimensions with respect to the energy and the zenith angle of neutrinos induced muons. The binning schemes have been chosen for the downward-going events and are given in Table 5.3 and Table 5.4. Table 5.3 gives the binning scheme for events having information of only the muon energies and zenith angles. The binning scheme for the analysis with the downward-going events where the hadron energy information is used in addition to the muon energy and zenith angle is given in Table 5.4. Since the muon reconstruction efficiency is nearly zero for the near-horizontal bin, a lower limit on zenith angle has been chosen *i.e.* $\cos\theta_z > 0.1$. The atmospheric neutrino energy spectrum follows a steep power law in the energy ($\sim E^{-2.7}$), resulting in a smaller number of events at a higher muon and hadron energy. Therefore, finer bins at the low energy and wider bins at high energy are considered for both the muon and the hadron, respectively. Moreover, it may be noticed that at low energy ($E = 1 - 1.5$

GeV) and high zenith angle ($\cos\theta_z = 0.1 - 0.2$), a bin of larger width is considered due to the fact that the reconstruction efficiency of the ICAL detector is poor in that region.

In the analysis, similar arguments are adopted while choosing the binning scheme for events where neutrinos come from all directions. The bin combinations for the cases when only the energy and zenith angle of the muon have been used and when the hadron energy information has been used as well, are given in Table 5.5 and Table 5.6, respectively. It is to be noted that a wider bin combinations are considered for upward-going neutrinos induced events. In this case, a depletion of events occurs as a result of oscillation of neutrinos due to the Earth matter effect. Therefore, a bin of wider width *i.e.* $\cos\theta_z = -0.3$ to 0.1 is considered. In the next section, the statistical method for estimating the χ^2 will be discussed.

Table 5.3: Bin combinations for the reconstructed parameters E_μ and $\cos\theta_z$ of muons produced due to downward-going muon-neutrinos, where χ^2 is estimated considering only muon events.

Parameter	Range	Bin width	Total bins
E_μ (GeV)	[1, 1.5]	0.5	1
	[1.5, 3.0]	0.25	6
	[3, 11]	0.5	16
	[11, 16]	1	5
	[16, 20]	2	2
$\cos\theta_z$	[0.1, 0.2]	0.05	2
	[0.2, 1.0]	0.025	32

Table 5.4: Bin combinations for the reconstructed parameters E_μ, $\cos\theta_z$ and E_h for muons and hadrons respectively, where the χ^2 is estimated considering the combined muon and hadron information of downward-going neutrino induced events.

Parameter	Range	Bin width	Total bins
E_μ (GeV)	[1, 1.5]	0.5	1
	[1.5, 5.5]	0.25	16
	[5.5, 8]	0.5	7
	[8, 13]	1	5
	[13, 17]	2	2
	[17, 20]	3	1
$\cos\theta_z$	[0.1, 0.25]	0.15	1
	[0.25, 1.0]	0.05	15
E_h	[0, 3]	3	1
	[3, 20]	17	1

Table 5.5: Bin combinations for the reconstructed parameters E_μ and cos θ_z for muons produced due to both upward-going and downward-going neutrinos, for the χ^2 estimation with muons only.

Parameter	Range	Bin width	Total bins
E_μ (GeV)	[1, 1.5]	0.5	1
	[1.5, 3.0]	0.25	6
	[3.0, 6.0]	0.5	6
	[6, 11]	1.0	5
	[11, 13]	2	1
	[13, 16]	3	1
	[16, 20]	4	1
cos θ_z	[-1.0, -0.3]	0.025	28
	[-0.3, 0.1]	0.4	1
	[0.1, 0.2]	0.1	1
	[0.2, 1.0]	0.025	32

Table 5.6: Bin combinations for the reconstructed parameters E_μ, cos θ_z and E_h for muons and hadrons where χ^2 is estimated considering the combined muon and hadron information and for the upward-going and downward-going neutrino induced events.

Parameter	Range	Bin width	Total bins
E_μ (GeV)	[1, 2]	1.0	1
	[2, 7]	0.5	10
	[7, 10]	1.0	3
	[10, 12]	2	1
	[12, 15]	3	1
	[15, 20]	5	1
cos θ_z	[-1.0, -0.3]	0.1	7
	[-0.3, 0.1]	0.4	1
	[0.1, 0.3]	0.1	2
	[0.3, 1.0]	0.05	14
E_h	[0, 2]	2	1
	[2, 20]	18	1

3 Procedure for χ^2 Estimation

After estimating the number of events with and without active-sterile oscillations, the sensitivity to the sterile neutrino mixing has been obtained from an estimation of the χ^2. Events are distributed in energy and zenith angle bins having variable widths as described above. In the analysis, Gaussian or Possionian definition of the χ^2 may be used depending upon the bin contents for putting the constraint on the active-sterile mixing parameters. If the bin content ≥ 5, then the Gaussian definition of the χ^2 can be used, which is as follows,

$$\chi^2 = \sum_{n_1=0}^{N_1} \sum_{n_2=0}^{N_2} \left(\frac{R'^{th}_{n_1,n_2} - R^{ex}_{n_1,n_2}}{\sigma(R^{ex}_{n_1,n_2})} \right)^2 , \tag{5.8}$$

where n_1 and n_2 are number of bins for energy and cosine of zenith angle for the muon, respectively, $R^{ex}_{n_1,n_2}$, $R'^{th}_{n_1,n_2}$ are the observed and theoretically predicted event rate. The definition given in Eq. 5.8 is based on the assumption that there is no uncertainty in the predicted data. On the other hand, there are several sources of systematic uncertainty *viz.* energy dependent flux, interaction cross-sections, direction of the incoming atmospheric neutrinos. Then including the systematic uncertainties, the modified theoretically predicted event rate is given as

$$R^{th}_{n_1,n_2} = R'^{th}_{n_1,n_2} \left(1 + \sum_{i=0}^{k} \pi^i_{n_1,n_2} \xi_i \right) + O(\xi^2), \tag{5.9}$$

where π^i_n is the strength of the coupling between the pull ξ_i and $R'^{th}_{n_1,n_2}$ which carries the information about systematic uncertainties and the summation over 'i' stands for the number of systematic uncertainties. Then rewriting Eq. 5.8 based on the pull method [129], the corresponding definition of χ^2 is given by

$$\chi^2 = min_{\xi_i} \sum_{n_1=0}^{N_1} \sum_{n_2=0}^{N_2} \left(\frac{R^{th}_{n_1,n_2} - R^{ex}_{n_1,n_2}}{\sigma(R^{ex}_{n_1,n_2})} \right)^2 . \tag{5.10}$$

Thereafter, Eq. 5.10 can be minimized with respect to the pull variables and the resulting set of k linear equations solved to obtain the unknown ξ_i. The χ^2 has been minimized by summing over all events with respect to energy and $\cos\theta_z$ bins. Further, if the bin content is < 5, then the Possionian definition of χ^2 can be used which is given as,

$$\begin{aligned}\chi^2_{\mu s} = min_{\xi_i} \sum_{n_1=0}^{N_1} \sum_{n_2=0}^{N_2} \Big[2 \left(R^{th}_{n_1,n_2} - R^{ex}_{n_1,n_2} \right) \\ +2R^{ex}_{n_1,n_2}\, ln \left(\frac{R^{ex}_{n_1,n_2}}{R^{th}_{n_1,n_2}} \right) \Big] + \sum_{i=0}^{k} \xi_i^2,\end{aligned} \tag{5.11}$$

where the subscript 'μs' in the χ^2 represents using only the muon information of the neutrino induced event. During the analysis it was seen, that in most cases, the bin contents are less than 5. Hence a Poissionian definition of χ^2 was used (see Eq. 5.11). Five systematic uncertainties are considered *viz.* an overall flux normalization error 20 %, overall normalization of cross-section 10 %, flux tilt factor which takes into account the deviation of atmospheric fluxes from a power law and zenith angle dependence of the flux 5 % and finally an overall 5 % systematic error. The energy dependent tilt factor has been implemented in the following way,

$$\Phi_\delta(E) = \Phi_0(E)\left(\frac{E}{E_0}\right)^\delta \simeq \Phi_0(E)\left(1 + \delta\, ln\frac{E}{E_0}\right). \tag{5.12}$$

For the zenith angle, the systematic uncertainty has been implemented as $0.5\times < cos\theta_z >$, where $< cos\theta_z >$ is the average value of the zenith angle bins. In an event, we have also added the hadron energy along with the detailed information of the muon, hence, the definition of χ^2 is given as,

$$\begin{aligned}\chi^2_{\mu s+hadrons} = min_{\xi_i} \sum_{n_1=0}^{N_1}\sum_{n_2=0}^{N_2}\sum_{n_3=0}^{N_3}\Big[2\Big(R^{ex}_{n_1,n_2,n_3} - \\ R^{th}_{n_1,n_2,n_3}\Big) \\ +2R^{ex}_{n_1,n_2,n_3}\, ln\left(\frac{R^{ex}_{n_1,n_2,n_3}}{R^{th}_{n_1,n_2,n_3}}\right)\Big] + \sum_{i=0}^{k}\xi_i^2\,,\end{aligned} \tag{5.13}$$

where n_3 is summed over the hadron energy. It may be noted that theoretically predicted and observed data correspond to without and with sterile neutrino oscillated events, respectively.

However, the χ^2 defined above is based on the oscillation parameters which are known to an infinite precision, which is not actually so. So to include uncertainties on the oscillation parameters, the χ^2 has been marginalized considering uncertainties on the active-sterile oscillation parameters *viz.* θ_{14}, θ_{24}, θ_{34} and Δm^2_{41}. The total χ^2, is estimated by adding the priors of Δm^2_{41} and θ_{14}, θ_{24} and θ_{34},

$$\begin{aligned}\chi^2_{total} = \chi^2 + \left(\frac{(\Delta m^2_{41})^{bf} - \Delta m^2_{41})}{\sigma(\Delta m^2_{41})}\right)^2 \\ + \left(\frac{(sin^2(2\theta_{\alpha\beta})^{bf} - sin^2(2\theta_{\alpha\beta})}{\sigma(sin^2(2\theta_{\alpha\beta})}\right)^2.\end{aligned} \tag{5.14}$$

The parameters $\sin^2 2\theta_{\alpha\beta}$ and Δm^2_{41} are varied within the range of 0.047 to 0.22 and 0.82 eV^2 to 2.19 eV^2, respectively. The errors on $\sin^2 2\theta_{\alpha\beta}$ and Δm^2_{41} are assumed to be 10 % of their best fit values. The results also depend weakly on the choice of the best fit values. It is to be noted here that in the analysis prior on $\sin^2 2\theta_{\alpha\beta}$ not on $\theta_{\alpha\beta}$ has been added as experimentally the earlier quantity will be measured.

4 Limits on Active-Sterile Neutrinos Oscillation Parameters

The exclusion curves are obtained considering events due to only downward-going and all direction neutrinos for an exposure of 1 Mton-yr. In order to find out the sensitivity of the ICAL to the active-sterile neutrino mixing parameters, the cut on χ^2 has been considered as 4.61 at 90 % CL. The exclusion limit for the Δm^2_{41} - $\sin^2 2\theta_{24}$, ($\sin^2 2\theta_{24}$= $U^2_{\mu 4}(1 - U_{\mu 4})^2$ and $U_{\mu 4} = cos\theta_{14} sin\theta_{24}$) plane is shown in Fig. 5.10 at $\theta_{14} = \theta_{34} = 0.0°$. Symbols 'D' and 'UD' correspond to only downward-going and all neutrinos, respec-

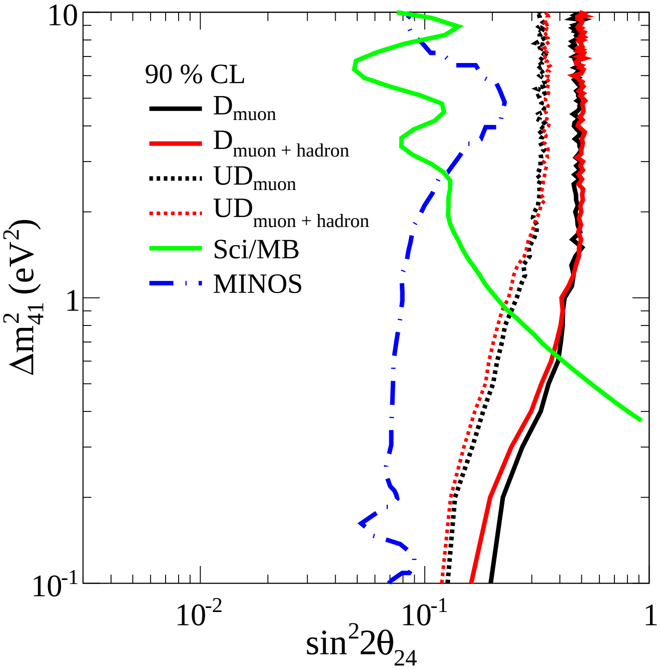

Figure 5.10: The 90 % exclusion limits in the $\Delta m^2_{41} - \sin^2 2\theta_{24}$ plane where $\sin^2 2\theta_{24}$= $U^2_{\mu 4}(1 - U_{\mu 4})^2$, expected from 1 Mton-yr of the ICAL data. The symbol 'D' and 'UD' corresponds to only downward-going neutrinos and neutrinos from all directions. All other sterile mixing angles (and phases) except for θ_{24} are set to zero for simplicity. Also SciBooNE/MiniBooNE and MINOS exclusion regions are shown for comparison.

tively reaching the detector. It may be noted that the regions to the right of the curves are excluded. The black line shows the active-sterile mixing sensitivity while considering only the downward-going neutrinos induced muon events. The red line shows the sensitivity to the sterile neutrino mixing, which is obtained from the analysis considering both the muon and the hadron information for the downward-going neutrino induced events. It has been found that for the magnetized ICAL detector at the INO, the exclusion limit for $\sin^2 2\theta_{24}$ can be ~ 0.19 at $\Delta m^2 = 0.1$ eV^2, using neutrino induced only muon information. This corresponds to an upper limit on θ_{24} of $\sim 13.2°$, while combining the muon and hadron information improves the sensitivity marginally to about 11.8° at 90 % C.L.. The

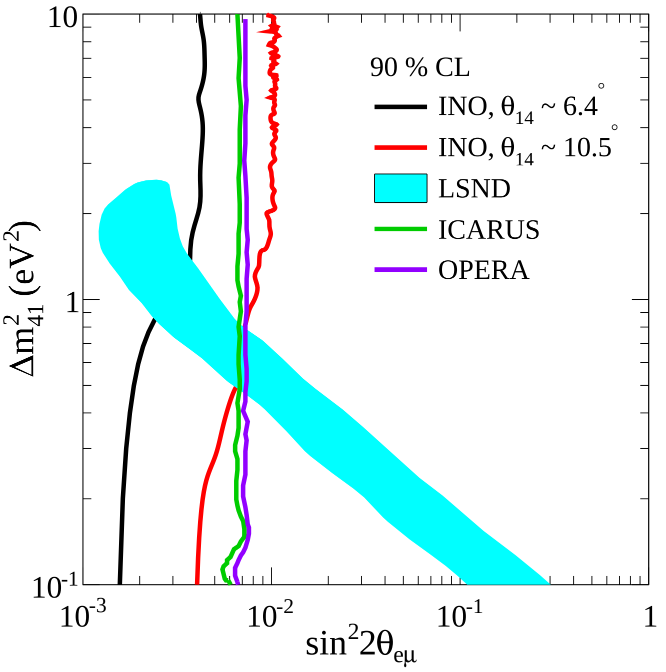

Figure 5.11: The 90 % exclusion limits in the $\Delta m^2_{41} - \sin^2 2\theta_{e\mu}$ plane where $\sin^2 2\theta_{e\mu} = 4\, U^2_{e4} U^2_{\mu 4}$, expected from an exposure 1 Mton-yr of the ICAL data. In case of the INO, the active-sterile mixing angles are considered as $\theta_{14} \sim 6.4°$ and 10.5° and $\theta_{34} = 0.0°$. Also the allowed region of the LSND and excluded region of the OPERA and the ICARUS results are shown for comparison.

mixing angle sensitivity further improves by considering that neutrinos coming from all directions and reaching the detector. It has been found that the upper limit of the mixing angle θ_{24} is $\sim 10°$ by considering the combined information of the neutrino (coming from all direction, UD) induced muon and hadron. It has been observed that only the mixing angle may be constrained but not Δm^2 because of the large path lengths. The green line in Fig. 5.10 shows the exclusion plot from the SciBooNE/MiniBooNE [130] experiment which corresponds to the ν_μ disappearance search. It has been found that at lower values of Δm^2, the ICAL detector has better sensitivity compared to results from the SciBooNE/

MiniBooNE (a short-baseline experiment, the path length and the energy chosen such that the detector has sensitivity about $\Delta m^2 = 1.0$ eV^2) due to the variable path length and energy of atmospheric neutrinos. From this study it has been concluded that there is a marginal improvement on sterile neutrino mixing sensitivity by adding hadron information to that of muons at lower values of Δm^2 (≤ 1.0 eV^2). The blue dashed-dot line shows results from the MINOS [131] experiment for comparison. This uses the ν_μ disappearance channel to yield upper bounds on $\sin^2 2\theta_{24}$ over a range of Δm^2_{43} = 0.01-100 eV^2.

The study on the active-sterile neutrino mixing sensitivity considering that the angle θ_{14} = 0.0° is not a good approximation. It has been already seen that there is an enhancement in the $P_{e\mu}$ oscillation channel due to the matter dependent resonances. Therefore, the sensitivity on the active-sterile mixing has been obtained considering Δm^2_{41} - $\sin^2 2\theta_{e\mu}$, ($\sin^2 2\theta_{e\mu}$= 4 $U^2_{e4} U^2_{\mu 4}$ and $U_{e4} = sin\theta_{14}$) plane as shown in Fig. 5.11 at $\theta_{14} \sim 6.4°$, 10.5° and θ_{34} = 0.0°. The black and red lines show the active-sterile mixing sensitivity considering the neutrino induced muon information where neutrinos reaching the ICAL from all directions are considered. The cyan shaded region shows the allowed parameter space from the LSND [75] experiment, obtained from the appearance search *i.e* $\bar{\nu}_\mu \rightarrow \bar{\nu}_e$, for comparison. The green line shows the results from the ICARUS [86] experiment which exclude most of the LSND allowed parameter space. The purple line shows the results from the OPERA [87] for the appearance of ν_e from the $\nu_\mu \rightarrow \nu_e$ oscillation channel, which limits the parameter space suggested by the LSND experiment observations.

In addition, the study has been also carried out by marginalizing the χ^2 over the active-sterile mixing parameters and including the corresponding priors. In this case, non-zero values of active-sterile mixing angles are considered for the various mixing angle planes. Here only energy and zenith angle information of muons are used for neutrinos reaching the ICAL detector from all directions. The best fit values for $\theta_{14} = \theta_{24} = \theta_{34} = 10°$ and at Δm^2_{41} = 1.0 eV^2 are used for estimating the χ^2 values from fits to the simulated data. In theory, while generating the exclusion limits for two mixing angles, the third mixing angle and Δm^2_{41} are marginalized and also the corresponding priors are added on it.

Figure 5.12 shows the exclusion plot for the θ_{14} - θ_{24} plane with and without marginalization and the corresponding prior values. The black filled circle represents the assumed best fit value. In the case of when there is no marginalization and priors on values of the Δm^2_{41} and θ_{34}, the constraint on the upper limit of the mixing angle θ_{24} for which the ICAL detector has sensitivity, is $\sim$ 13° and $\sim$ 16° at 68 % and 90 % CL, respectively. Similarly,

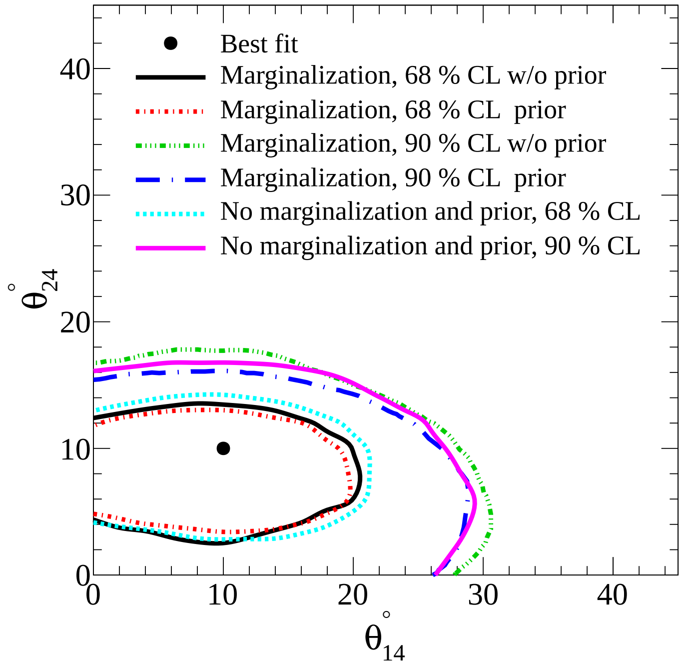

Figure 5.12: The exclusion limits for the θ_{14} - θ_{24} plane, expected at an exposure of 1 Mton-yr of the ICAL data.

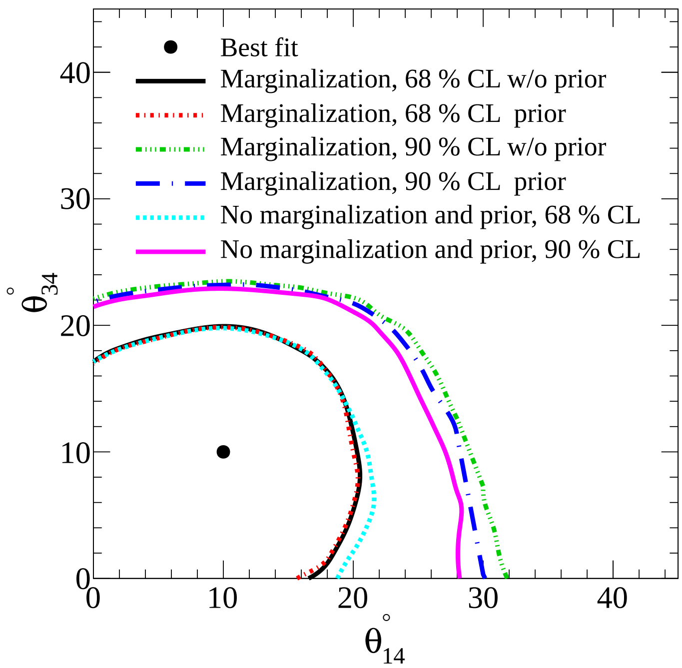

Figure 5.13: The exclusion limits in the $\theta_{14} - \theta_{34}$ plane, expected at an exposure of 1 Mton-yr of the ICAL data.

the upper limit on the mixing angle θ_{14} is $\sim 21^\circ$ and 26° at 68 % and 90 % CL, respectively. Further, the χ^2 is marginalized over the oscillation parameters Δm^2_{41} and θ_{34} and

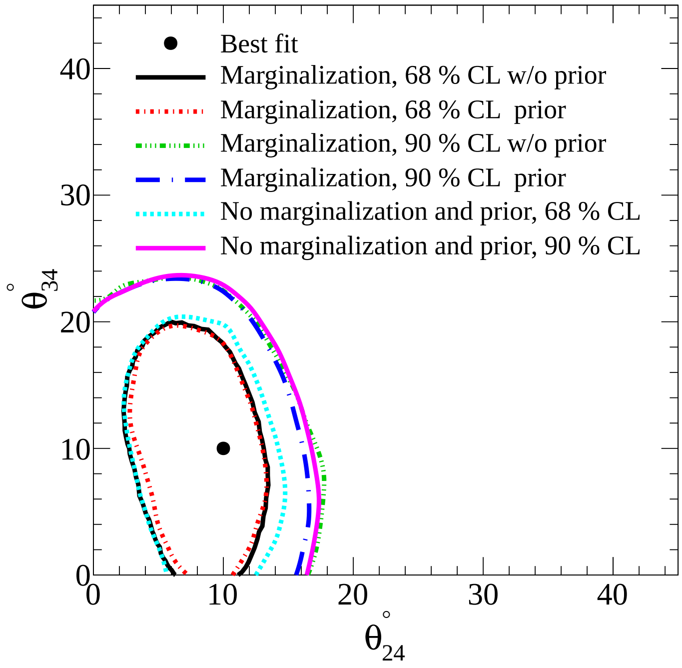

Figure 5.14: The exclusion limits in the θ_{24} - θ_{34} plane, expected at an exposure of 1 Mton-yr of the ICAL data.

leads to a limit on θ_{14} between 0.0° to 20° and ~ 30° at 68 % and 90 % CL, respectively. On the other hand, the estimated upper limit of the mixing angle θ_{24} for which the ICAL detector will be sensitive is about 4° - 12° and 16° at 68 % and 90 % CL, respectively. It has also been observed that the inclusion of a prior has a minimal effect on the sensitive limits.

Figure 5.13 shows the exclusion plot for the θ_{14} - θ_{34} plane, with and without consideration of marginalization and the corresponding prior values. The black filled circle represents the assumed best fit value. When marginalization and priors on values of the Δm^2_{41} and θ_{24} are not considered, the constraint on the upper limit of the mixing angle θ_{34} is ~ 17° and ~ 22° at 68 % and 90 % CL, respectively. Similarly, the upper limit on the mixing angle θ_{14} is ~ 19° and 28° at 68 % and 90 % CL, respectively. Further, the χ^2 is marginalized over the oscillation parameters Δm^2_{41} and θ_{24}. It is found that the limit on θ_{34} is about 17° and ~ 22° at 68 % and 90 % CL, respectively. On the other hand, the estimated upper limit of the mixing angle θ_{14} for which the ICAL detector will be sensitive is ~ 20° and 30° at 68 % and 90 % CL, respectively. It is also observed that the inclusion of a prior has a minimal effect on the sensitive limits.

Figure 5.14 shows the exclusion plot in the θ_{24} - θ_{34} plane, with and without marginalization of χ^2 over the values of Δm^2_{41} and θ_{14} and adding the corresponding prior on it.

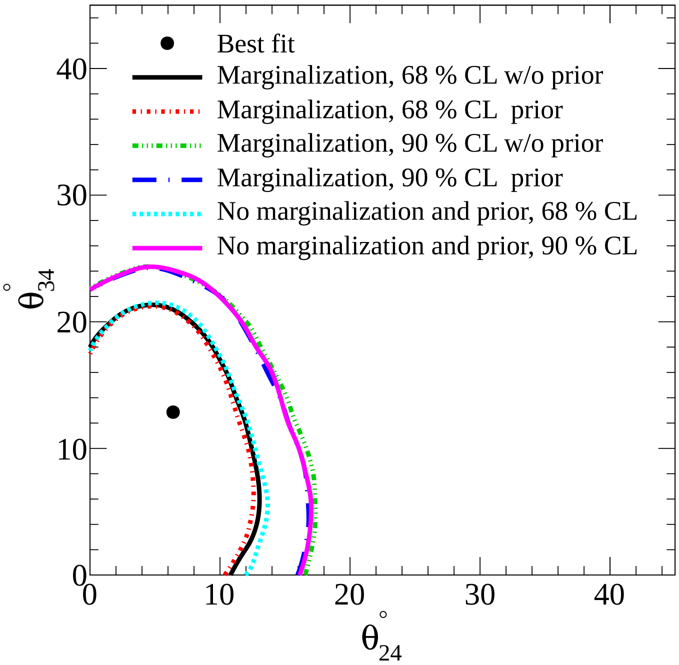

Figure 5.15: The exclusion limits in the θ_{24} - θ_{34} plane, expected from 1 Mton-yr of the ICAL data.

The black filled circle represents the assumed best fit value. In the case where marginalization and priors on values of the Δm^2_{41} and θ_{14} are not considered, the constraint on the upper limit of the mixing angle θ_{34} is ~ 20° and ~ 21° at 68 % and 90 % CL, respectively. Similarly, the mixing angle θ_{24} lies in the range of ~ 6° - 12° and its upper limit is ~ 16° at 68 % and 90 % CL, respectively. Further, the χ^2 is marginalized over the oscillation parameters Δm^2_{41} and θ_{14}. It is found that the limit on θ_{34} is about 18° and it lies between 0 to 20° at 68 % and 90 % CL, respectively. On the other hand, the estimated upper limit of the mixing angle θ_{24} for which the ICAL detector lies between ~ 7° - 11° and ~ 16° and 68 % and 90 % CL, respectively. It is also observed that the inclusion of a prior has a minimal effect on the corresponding sensitivity limits.

Further, sensitivity limits on the active-sterile mixing angles are obtained using the present best fit values [92] of θ_{24} and θ_{34} which are 6.393°, 12.862° and Δm^2_{41} = 1.6 eV^2. The range of parameters for over which the χ^2 has been marginalized and the corresponding priors added are for the mixing angle θ_{14} = 6.26° - 13.676°, θ_{24} = 3.96° - 10.986° and Δm^2_{41} = 0.82 eV^2 - 2.19 eV^2. Figure 5.15 shows the exclusion plot for the θ_{24} - θ_{34} plane without and with consideration of marginalization and the inclusion of corresponding priors on χ^2. The upper limits on the mixing angle θ_{24} is about 12° and about 16° at 68 % CL and 90 % CL, respectively without marginalizing the χ^2 and adding the priors on it. Similarly,

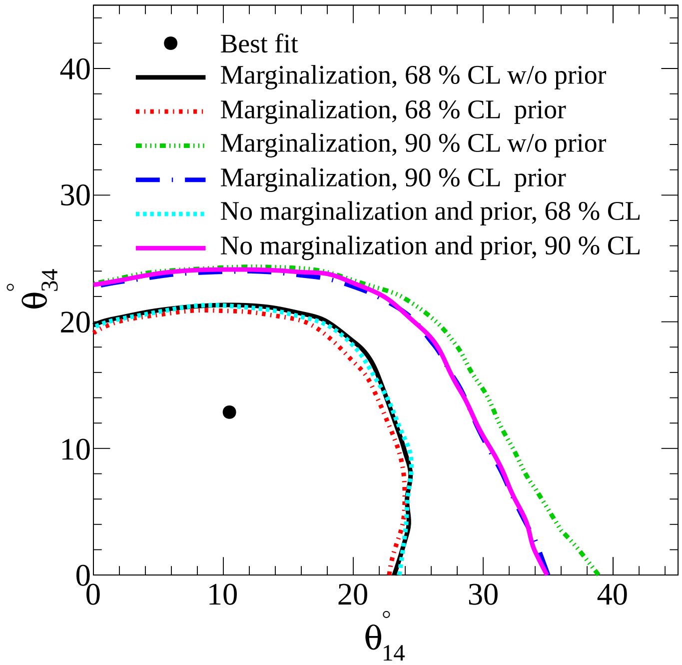

Figure 5.16: The exclusion limits in the θ_{24} - θ_{34} plane, expected from 1 Mton-yr of the ICAL data.

upper limits on the mixing angle θ_{34} are $\sim$ 18° and $\sim$ 23° at 68 % CL and 90 % CL, respectively without marginalizing the χ^2 and adding the priors on it However, after only marginalizing the χ^2, the estimated upper limit on θ_{24} is $\sim$ 10° at 68 % CL whereas both marginalization and prior has a minimal effect at 90 % CL. A similar behavior is observed for the mixing angle θ_{34} after performing the marginalization and adding prior on the χ^2 values. Figure 5.16 shows the exclusion plot for the θ_{14} - θ_{34} plane without and with consideration of marginalization and the corresponding prior values. At 68% CL and considering only marginalization, the upper limit on θ_{34} is about 20° whereas for θ_{14} it is about 23°. After including the marginalization and adding the prior values, the limit on θ_{34} and θ_{14} improves marginally. The upper limits on θ_{34} and θ_{14} are about 40° and 23°, respectively considering only the marginalization over Δm^2_{41} and θ_{24} at 90% CL, while the prior has a minimal effect on the θ_{34}.

Hence, from this study it is concluded that the ICAL detector at INO is capable of measuring eV^2 active-sterile neutrino mixing if θ_{24} >10° at an exposure of 1 Mton-yr. The detector has the capability of placing upper bounds on θ_{14} and θ_{34} of about 30° and 20°, respectively.

Chapter 6

Summary and Conclusions

After two decades, results from various experiments have established that neutrinos have non-zero mass and oscillate from one flavour to another. However, we still have only a limited knowledge of neutrinos *viz*. their absolute mass, whether they are Dirac or Majorana particles, their mass hierarchy, whether they exhibit CP violation, etc. Further, there are experimental indications of the existence of sterile neutrinos coming from various SBL experiments.

In the present thesis, a study has been carried out on the ICAL magnet at the INO, its response at various strengths of magnetic field to muons and also to the active-sterile neutrino mixing sensitivity. In Chapter 1, the discovery of the neutrino is briefly presented. The various kinds of neutrino sources and their characteristics vis a vis neutrino experiments is also described.

In Chapter 2, the quantum mechanical neutrino oscillation formalism is presented for the 2, 3 and 3 + 1 neutrinos models considering propagation in vacuum as well as in matter. The current status on the active as well as sterile neutrino oscillation parameters is also presented.

In Chapter 3, the ICAL magnet and its importance at the INO is presented. The electromagnetic simulation of the ICAL magnet has been carried out for various configurations to optimize the design of the ICAL detector. The DC current and number of turns in the coil has been optimized for getting a desired B-field at the lowest possible dissipation of power in the coils. From the simulation, considering the B-field distribution over a 16 m $\times$ 16 m area, it has been observed that the optimum length of continuous slots is about 10 m. Also, the plate thickness of the ICAL magnet has been optimized with respect to the B-field distribution and the estimated value is ≥ 4 cm, justifying the choice of plate thickness of 5.6 cm. It has been observed that configurations C2 and C3 with arrangement of tiles which fill the 16 m × 16 m area seem to provide a better B-field distribution with respect to minimum Ohmic loss in coils. The impact of air gaps on the B-field distribution has been also studied at various gap sizes using the C2 configuration. It has been found that the B-field, as well as its distribution for which $|B| \geq 1$ T, reduces when the size of gaps along tiles increases. However, in a practical situation a gap of 2 mm is sufficient for the arrangement of tiles. The over all B-field distribution was also simulated. The C2 configuration, where about 80 % of the volume has a field of $|B| \geq 1$ T, was considered optimum.

The response of the ICAL detector for muons at various strengths of magnetic field is presented in Chapter 4. It has been observed that at a given magnetic field strength and at given incident zenith angle, the detector energy resolution, at lower energies, is affected by the multiple Coulomb scattering whereas at higher energies the poorer resolution is due to the uncertainty in sagitta measurements. We found that the detector energy resolution as well as efficiencies improve with an increase in the magnetic field. It has been concluded that the magnetic field strength of 1.5 T will provide satisfactory results.

In Chapter 5, results are presented on the active-sterile neutrino mixing sensitivity of the ICAL detector at the INO for an exposure of 1 Mton-yr. To find out the sensitivity, we have generated 3 and 3 + 1 generation neutrino events using the MC method based reweighting algorithm. The detector response, in particular, the detector energy and angular resolution on true events, are implemented using the MC method considering various probability distributions. In the statistical analysis, a χ^2 for each energy and zenith angle bin is estimated considering bins of variable width. It was observed that the ICAL detector has an active-sterile neutrinos mixing sensitivity provided the mixing angle $\theta_{24} \geq 10^\circ$ with squared mass difference of $\Delta m^2_{41} \geq 0.1$ eV^2 at 90 % CL, for the case where neutrinos reach at the detector from all directions. We have also put the constraint on mixing angles θ_{14} and θ_{34} and upper limit are about 20° to 30°. It has been concluded that the ICAL detector at the INO has a sensitivity to an eV^2-scale active-sterile neutrino mixing.

Appendix A

Study of the B-field Using Single Layer Versus Three Layer

The electromagnetic simulation was carried out considering the baseline design which has single and three layers of iron plate as shown in Figs. A.1 (a) and (b), respectively. Each

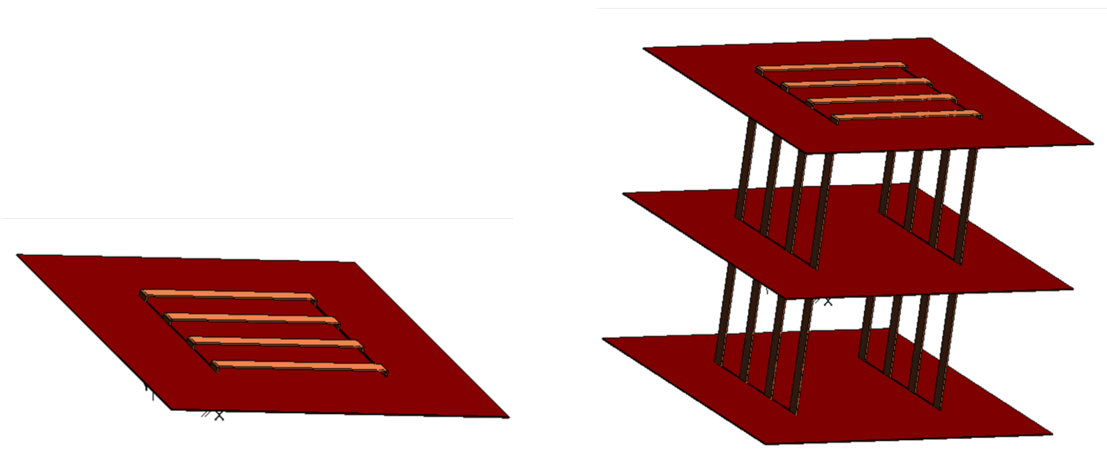

(a) (b)

Figure A.1: Schematic of ICAL magnet (a) single layer (b) 3 layers. Iron plates are on XY-plane and coils are on XZ-plane.

configuration contains 4 coils having dimensions of length 8 m and height 0.456 m and 15 m respectively. At a coil height of 0.456 m, a single iron layer was placed at mid-height of the coils. At 15 m coils height, we have chosen two configurations, one containing a single layer placed at the middle of coil height (Z = 0 m) and another one with three layers and placed at Z = − 7.272 m, Z = 0 m, and Z = 7.272 m, respectively. The B-field was estimated at 20 kA-turns for each configuration. At |B| ≥ 1 T, B-field values are extracted for 5 cm × 5 cm pixels for both configurations. Figure A.2 (a) shows the ratio of B-field between single layer (coil height 0.456 m) to only single layer (coil height 15 m) placed at mid-height of coils. At coil height of 15 m, the B-field ratio was plotted considering the single layer placed at the mid-height of coils and mid layer where the configuration contains three layers as shown in Fig. A.2 (b). Figures A.3 (a) and (b) show the ratio plot of B-field between mid to top layer and mid to bottom layer, respectively. It was found that the B-fields in both configurations match to within about 4 %.

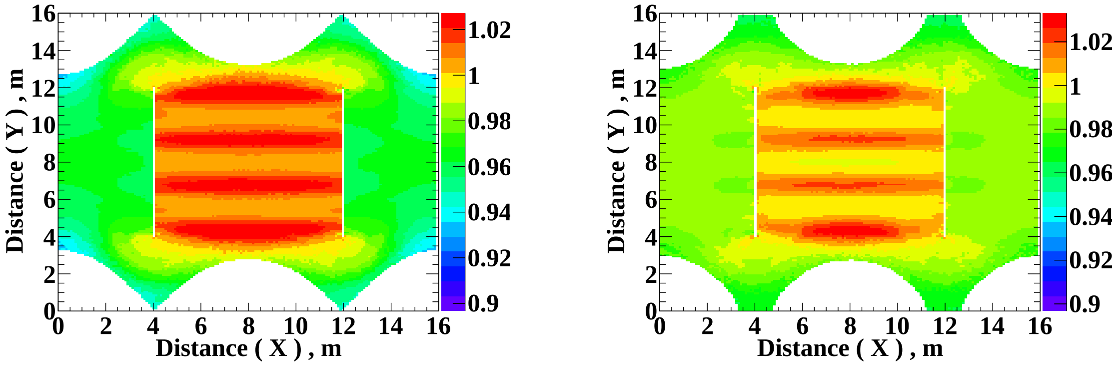

(a) (b)

Figure A.2: Ratio of |B|-field (|B| ≥ 1 T) at 20 kA-turns for (a) single layer (coil height 0.456 m) to single layer (coil height 15m) at centre (b) 15 m coil height and single to middle layer (containing 3 layers).

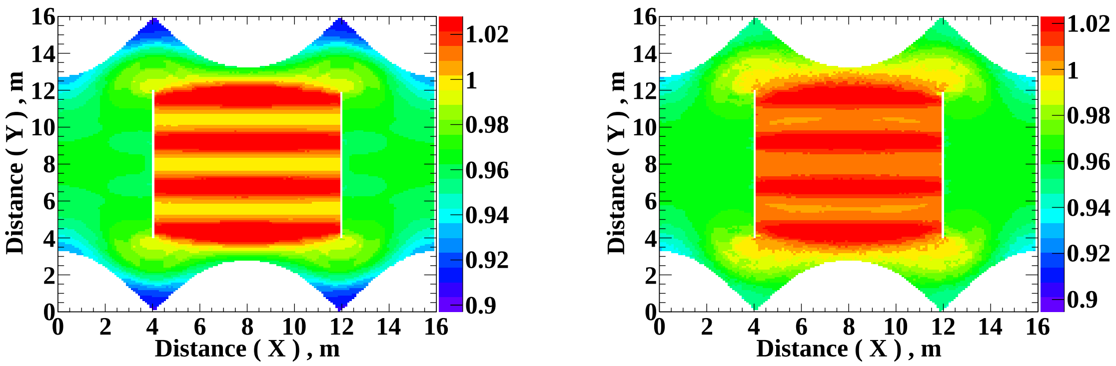

(a) (b)

Figure A.3: Ratio of |B|-field at 20 kA-turns (a) single layer (soil height 0.456 m) to top layer (model containing 3 layers, coil height 15 m) and (b) single layer (soil height 0.456 m) to bottom layer (model containing 3 layers coil height 15 m).

Appendix B

Magnetic Field Measurement of the Prototype ICAL Detector

A comparative study was carried out between simulated and measured B-field for the prototype magnet. The magnet consists of 13 layers of iron plate and each layer consists of a C and T section as shown in Fig. B.1, with ~ 35 ton weight, which is about 1/1000th the weight of the 51 kton ICAL detector. The dimensions of C and T are 2480 mm $\times$ 1560 mm, 2480 mm $\times$ 1560 mm respectively and each has a thickness of 5 cm. Iron layers alternate with gaps of 5 cm and in that RPC detectors having size of 1 m $\times$ 1 m are placed in the central region of the detector (where the magnetic field is almost uniform) to get the hit information of cosmic ray muons. The electromagnetic simulation of this prototype magnet is shown in Fig. B.2. The orientation of arrows shows the direction of B-field and their length represent the magnitude of B-field. It was found that, magnetic field is almost uniform in the central volume (~ 1 m $\times$ 1 m $\times$ 0.05 m) plate as shown in Fig. B.2(b). The magnet was excited by 4 coils each having 5 numbers of turns. The copper conductor used in the coils has a central bore through which chilled demineralized water (low conductivity water) is circulated to reduce the Joule heating. There are two current sources in the main power supply and each one is designed to provides a maximum DC current of 500 A for exciting the coil. It can provide an effective magnetic field of ~ 1.4 T in the central region of ~ 1 m^2 area.

To measure the B-field in each layer, copper coils designated as primary turns, are excited by a current up to about 500 A DC with increments of 50 A. Search coils are placed at the middle of the plate and are used to measure the induced emf. Due to changing current, there is change in magnetic flux in the secondary coils which is measured by a

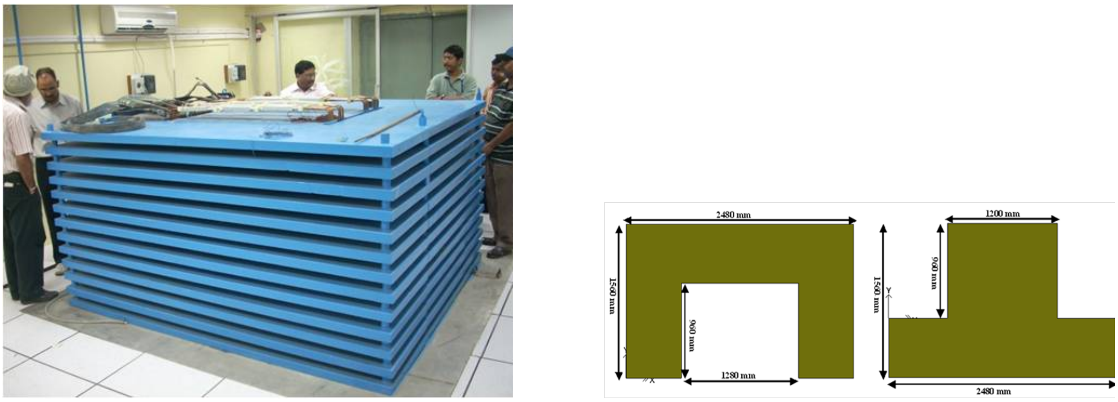

(a) (b)

Figure B.1: (a) Prototype ICAL magnet and (b) schematic of one layer with C and T-sections.

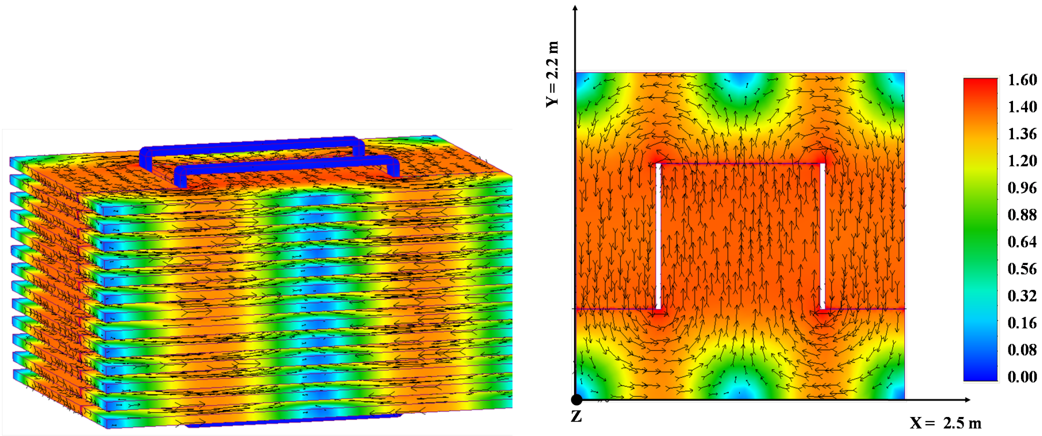

(a) (b)

Figure B.2: B-field profile of (a) 13 layers iron plate, (b) a single layer, top view C and T-sections.

flux meter (Digital Flux Meter 900, M/s. Ferrites India). The flux meter gives the output in terms of Maxwell turns. The measurements of magnetic flux Φ_1, Φ_2 have been taken in both positive and negative polarity of current respectively. Then B-field was estimated by taking the average of the flux $((|\Phi_1| + |\Phi_2|)/2)$ at both polarities and dividing by the cross-sectional area (1.2×0.05 m^2) of the plate. Figure B.3 shows the measured B-field values[1] at various Ampere-turns for some of layers. It was found that B-field values are not the same for all layers. The variation of B-field depends on the plate thickness, gap between C and T-section etc. In an ideal situation, the field over middle and side section of the plate should be same. On the other hand, it was observed that, the B-field values

[1]The measured data point has no error bar as only one measurement has been carried for estimating the B-field values.

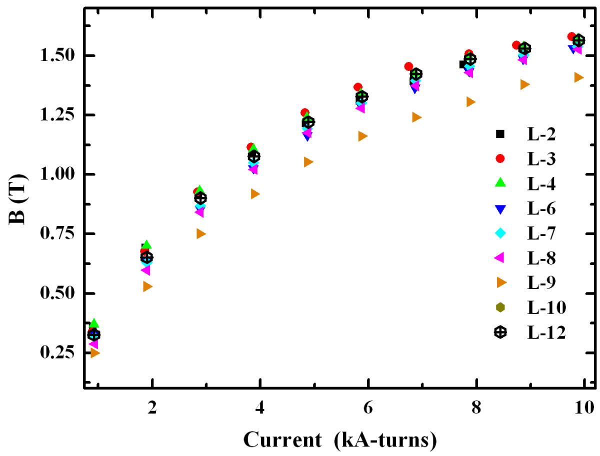

Figure B.3: Variation of measured B-field with current.

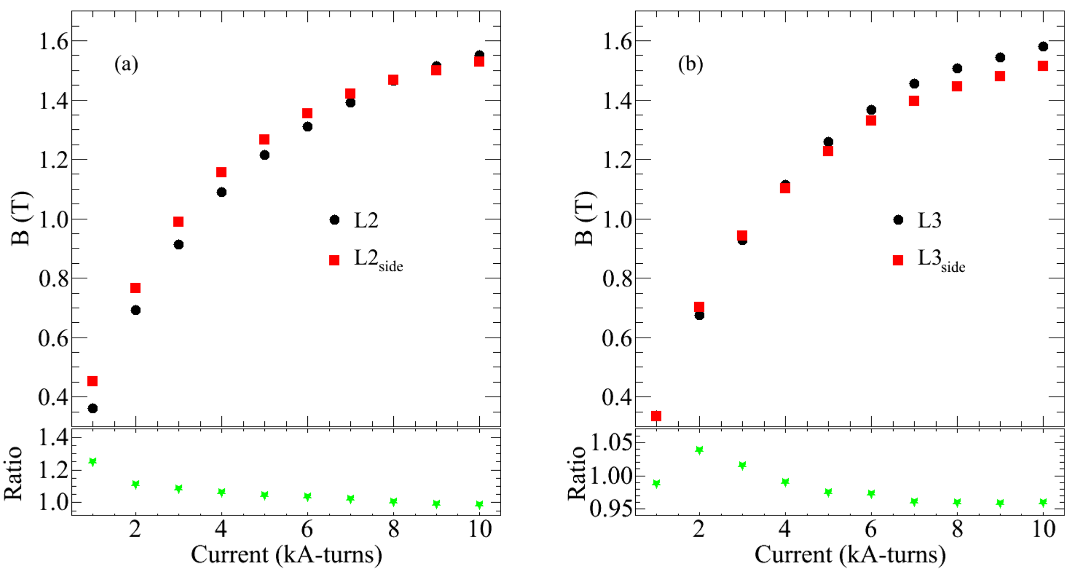

Figure B.4: B-field comparison between middle and sections of (a) second layer and (b) third layer.

in the middle part and side part of the plates have a maximum variation of about 20 % for layer L2 as shown in Fig. B.4 (a). Further, the comparison of the measured B-field values for layer, L3, between side and middle section matches within ± 5% as shown in Fig. B.4 (b).

A comparative study was carried out between simulated and measured B-field values for

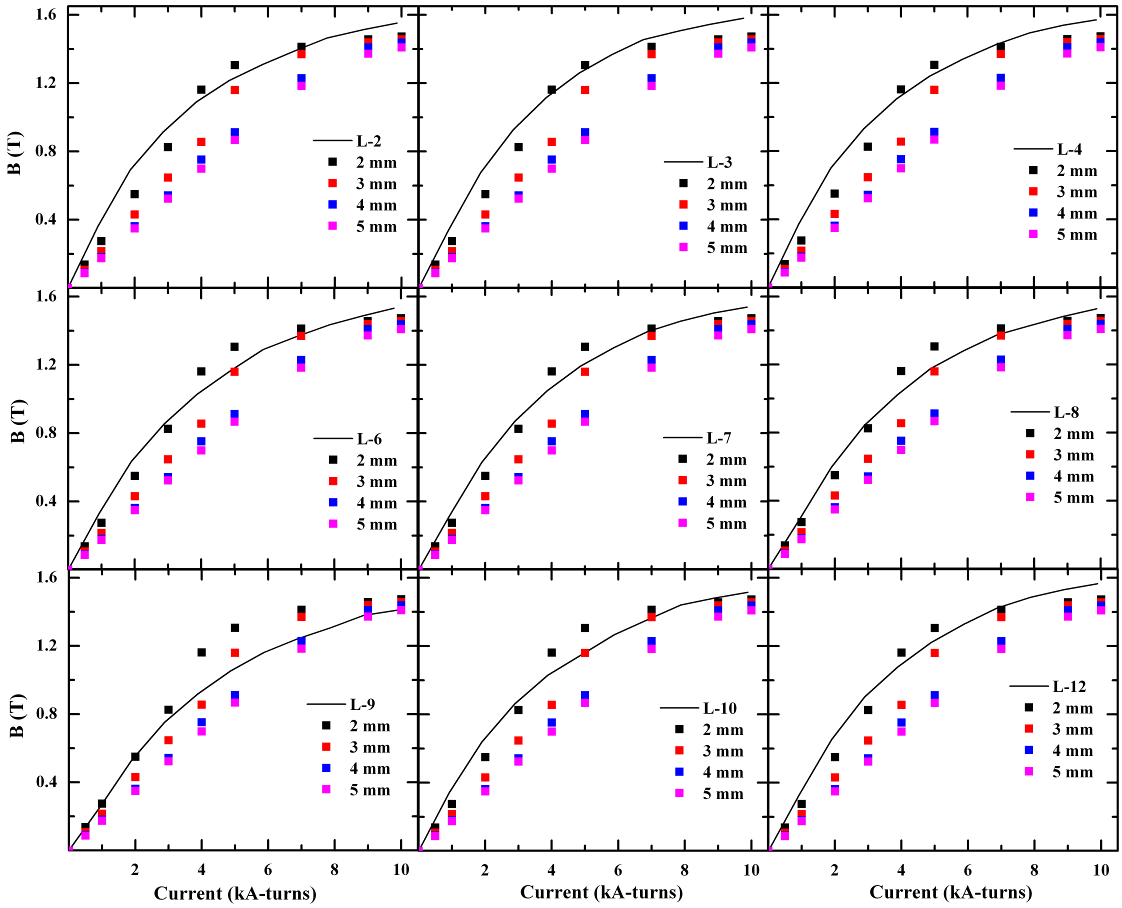

Figure B.5: Comparison of the B-field simulation and measured data for prototype magnet.

some of layers as shown in Fig. B.5. The black line shows the measured B-fields. The square symbols represent the simulated B-fields for gaps of 2 mm to 5 mm between C and T sections. It was found that the measured values match with simulated ones if one puts, by hand, a gap of 2 mm between the C and T-sections. At higher values of the gap, the mismatch between simulated and measured B-field is due to fringing of flux in the joint region of the C and T sections. It may be noted that the fringe field due to the magnetized iron is about 15 to 20 Gauss.

Bibliography

[1] H. Bethe and R. Peierls, Nature **133**, 532 (1934).

[2] C. L. Cowan, F. Reines, F. B. Harrison, H. W. Kruse and A. D. McGuire, Science **124**, 103 (1956).

[3] G. Danby, J. M. Gaillard, K. A. Goulianos, L. M. Lederman, N. B. Mistry, M. Schwartz and J. Steinberger, Phys. Rev. Lett. **9**, 36 (1962).

[4] K. Kodama *et al.* [DONUT Collaboration], Phys. Lett. B **504**, 218 (2001).

[5] M. Goldhaber, L. Grodzins and A. W. Sunyar, Phys. Rev. **109**, 1015 (1958).

[6] V. N. Aseev *et al.* [Troitsk Collaboration], Phys. Rev. D **84**, 112003 (2011).

[7] C. Kraus *et al.*, Eur. Phys. J. C **40**, 447 (2005).

[8] M. Auger *et al.* [EXO-200 Collaboration], Phys. Rev. Lett. **109**, 032505 (2012).

[9] K. Assamagan *et al.*, Phys. Rev. D **53**, 6065 (1996).

[10] R. Barate *et al.* [ALEPH Collaboration], Eur. Phys. J. C **2**, 395 (1998).

[11] G. Barbiellini and G. Cocconi, Nature **329**, 21 (1987).

[12] A. G. Beda, E. V. Demidova, A. S. Starostin, V. B. Brudanin, V. G. Egorov, D. V. Medvedev, M. V. Shirchenko and T. Vylov, Phys. Part. Nucl. Lett. **7**, 406 (2010).

[13] S. Schael *et al.* [ALEPH and DELPHI and L3 and OPAL and SLD and LEP Electroweak Working Group and SLD Electroweak Group and SLD Heavy Flavour Group Collaborations], Phys. Rept. **427**, 257 (2006).

[14] J. Beringer *et al.* [Particle Data Group Collaboration], Phys. Rev. D **86**, 010001 (2012).

[15] R. Davis, Rev. Mod. Phys. **75**, 985 (2003).

[16] J. N. Bahcall, A. M. Serenelli and S. Basu, Astrophys. J. **621**, L85 (2005).

[17] C. Amsler *et al.* [Particle Data Group Collaboration], Phys. Lett. B **667**, 1 (2008).

[18] R. Davis, Jr., D. S. Harmer and K. C. Hoffman, Phys. Rev. Lett. **20**, 1205 (1968).

[19] J. N. Abdurashitov *et al.* [SAGE Collaboration], Phys. Rev. C **60**, 055801 (1999).

[20] W. Hampel *et al.* [GALLEX Collaboration], Phys. Lett. B **447**, 127 (1999).

[21] M. Altmann *et al.* [GNO Collaboration], Phys. Lett. B **616**, 174 (2005).

[22] K. S. Hirata *et al.* [Kamiokande-II Collaboration], Phys. Rev. Lett. **63**, 16 (1989).

[23] J. Hosaka *et al.* [Super-Kamiokande Collaboration], Phys. Rev. D **73**, 112001 (2006).

[24] Q. R. Ahmad *et al.* [SNO Collaboration], Phys. Rev. Lett. **89**, 011301 (2002).

[25] B. Aharmim *et al.* [SNO Collaboration], Phys. Rev. Lett. **101**, 111301 (2008).

[26] B. Aharmim *et al.* [SNO Collaboration], Phys. Rev. C **81**, 055504 (2010).

[27] C. Arpesella *et al.* [Borexino Collaboration], Phys. Rev. Lett. **101**, 091302 (2008).

[28] B. Aharmim *et al.* [SNO Collaboration], Phys. Rev. C **72**, 055502 (2005).

[29] B. Aharmim *et al.* [SNO Collaboration], Phys. Rev. C **88**, 025501 (2013) and the refernces there in.

[30] M. Honda, T. Kajita, K. Kasahara and S. Midorikawa, Phys. Rev. D **70**, 043008 (2004).

[31] C. V. Achar *et al.*, Phys. Lett. **18**, 196 (1965).

[32] F. Reines, M. F. Crouch, T. L. Jenkins, W. R. Kropp, H. S. Gurr, G. R. Smith, J. P. F. Sellschop and B. Meyer, Phys. Rev. Lett. **15**, 429 (1965).

[33] Y. Fukuda *et al.* [Super-Kamiokande Collaboration], Phys. Rev. Lett. **81**, 1562 (1998).

[34] Y. Ashie *et al.* [Super-Kamiokande Collaboration], Phys. Rev. D **71**, 112005 (2005).

[35] R. Wendell *et al.* [Super-Kamiokande Collaboration], Phys. Rev. D **81**, 092004 (2010).

[36] G. Fiorentini, M. Lissia and F. Mantovani, Phys. Rept. **453**, 117 (2007), [arXiv:0707.3203 [physics.geo-ph]].

[37] T. Araki, S. Enomoto, K. Furuno, Y. Gando, K. Ichimura, H. Ikeda, K. Inoue and Y. Kishimoto *et al.*, Nature **436**, 499 (2005).

[38] G. Bellini *et al.* [Borexino Collaboration], Phys. Lett. B **687**, 299 (2010).

[39] K. Hirata *et al.* [Kamiokande-II Collaboration], Phys. Rev. Lett. **58**, 1490 (1987).

[40] R. M. Bionta, G. Blewitt, C. B. Bratton, D. Casper, A. Ciocio, R. Claus, B. Cortez and M. Crouch *et al.*, Phys. Rev. Lett. **58**, 1494 (1987).

[41] C. Bemporad, G. Gratta and P. Vogel, Rev. Mod. Phys. **74**, 297 (2002).

[42] M. Apollonio *et al.* [CHOOZ Collaboration], Phys. Lett. B **466**, 415 (1999).

[43] F. Boehm *et al.*, Phys. Rev. D **64**, 112001 (2001).

[44] T. Araki *et al.* [KamLAND Collaboration], Phys. Rev. Lett. **94**, 081801 (2005); S. Abe *et al.* [KamLAND Collaboration], Phys. Rev. Lett. **100**, 221803 (2008).

[45] Y. Abe *et al.* [Double Chooz Collaboration], Phys. Rev. Lett. **108**, 131801 (2012).

[46] F. P. An *et al.* [Daya Bay Collaboration], Phys. Rev. Lett. **108**, 171803 (2012).

[47] J. K. Ahn *et al.* [RENO Collaboration], Phys. Rev. Lett. **108**, 191802 (2012).

[48] M. H. Ahn *et al.* [K2K Collaboration], Phys. Rev. D **74**, 072003 (2006).

[49] P. Adamson *et al.* [MINOS Collaboration], Phys. Rev. Lett. **101**, 131802 (2008).

[50] P. Adamson *et al.* [MINOS Collaboration], Phys. Rev. Lett. **107**, 181802 (2011).

[51] P. Adamson *et al.* [MINOS Collaboration], Phys. Rev. Lett. **110**, 171801 (2013).

[52] K. Abe *et al.* [T2K Collaboration], Phys. Rev. Lett. **107**, 041801 (2011).

[53] K. Abe *et al.* [T2K Collaboration], Phys. Rev. D **88**, 032002 (2013).

[54] P. Zucchelli, Phys. Lett. B **532**, 166 (2002).

[55] B. Pontecorvo, Sov. Phys. JETP **6**, 429 (1957); Sov. Phys. JETP **7**, 172 (1958).

[56] Z. Maki, M. Nakagawa and S. Sakata, Prog. Theor. Phys. **28**, 870 (1962).

[57] B. Pontecorvo, Sov. Phys. JETP **26**, 984 (1968).

[58] V. N. Gribov and B. Pontecorvo, Phys. Lett. B **28**, 493 (1969).

[59] L. Wolfenstein, Phys. Rev. D **17**, 2369 (1978).

[60] S. P. Mikheev and A. Y. Smirnov, Sov. J. Nucl. Phys. **42**, 913 (1985); Nuovo Cim. C **9**, 17 (1986).

[61] B. T. Cleveland, T. Daily, R. Davis, Jr., J. R. Distel, K. Lande, C. K. Lee, P. S. Wildenhain and J. Ullman, Astrophys. J. **496**, 505 (1998).

[62] W. C. Haxton, R. G. Hamish Robertson and A. M. Serenelli, Ann. Rev. Astron. Astrophys. **51**, 21 (2013), [arXiv:1208.5723 [astro-ph.SR]].

[63] J. N. Bahcall, S. Basu and M. H. Pinsonneault, Phys. Lett. B **433**, 1 (1998).

[64] Y. Fukuda *et al.* [Kamiokande Collaboration], Phys. Rev. Lett. **77**, 1683 (1996).

[65] K. A. Olive *et al.* [Particle Data Group Collaboration], Chin. Phys. C **38**, 090001 (2014) and references therein.

[66] E. Kearns, Nucl. Phys. Proc. Suppl. **70**, 315 (1999).

[67] K. S. Hirata *et al.* [Kamiokande-II Collaboration], Phys. Lett. B **280**, 146 (1992).

[68] M. Mezzetto and T. Schwetz, J. Phys. G **37**, 103001 (2010).

[69] F. Capozzi, G. L. Fogli, E. Lisi, A. Marrone, D. Montanino and A. Palazzo, Phys. Rev. D **89**, 093018 (2014).

[70] G. L. Fogli, E. Lisi, A. Marrone, D. Montanino, A. Palazzo and A. M. Rotunno, Phys. Rev. D **86**, 013012 (2012).

[71] D. V. Forero, M. Tortola and J. W. F. Valle, Phys. Rev. D **86**, 073012 (2012).

[72] M. C. Gonzalez-Garcia, M. Maltoni, J. Salvado and T. Schwetz, JHEP **1212**, 123 (2012).

[73] G. C. Branco, R. G. Felipe and F. R. Joaquim, Rev. Mod. Phys. **84**, 515 (2012).

[74] M. C. Chen and K. T. Mahanthappa, Phys. Lett. B **681**, 444 (2009).

[75] A. Aguilar *et al.* [LSND Collaboration], Phys. Rev. D **64**, 112007 (2001).

[76] A. A. Aguilar-Arevalo *et al.* [MiniBooNE Collaboration], Phys. Rev. Lett. **105**, 181801 (2010).

[77] A. A. Aguilar-Arevalo *et al.* [MiniBooNE Collaboration], Phys. Rev. Lett. **110**, 161801 (2013).

[78] P. Huber, Phys. Rev. C **84**, 024617 (2011).

[79] T. A. Mueller *et al.*, Phys. Rev. C **83**, 054615 (2011).

[80] G. Mention *et al.*, Phys. Rev. D **83** , 073006 (2011).

[81] D. N. Abdurashitov *et al.*, Phys. Rev. Lett. **77**, 4708 (1996); J. N. Abdurashitov *et al.* [SAGE Collaboration], Phys. Rev. C **59**, 2246 (1999).

[82] P. Anselmann *et al.* [GALLEX Collaboration], Phys. Lett. B **342**, 440 (1995); W. Hampel *et al.* [GALLEX Collaboration], Phys. Lett. B **420**, 114 (1998).

[83] C. Giunti and M. Laveder, Phys. Rev. C **83**, 065504 (2011).

[84] B. Armbruster *et al.* [KARMEN Collaboration], Phys. Rev. D **65**, 112001 (2002).

[85] P. Astier *et al.* [NOMAD Collaboration], Phys. Lett. B **570**, 19 (2003).

[86] M. Antonello *et al.* [ICARUS Collaboration], Eur. Phys. J. C **73**, 2599 (2013).

[87] N. Agafonova *et al.* [OPERA Collaboration], JHEP **1307**, 004 (2013); JHEP **1307**, 085 (2013).

[88] K. Abe *et al.* [Super-Kamiokande Collaboration], Phys. Rev. D **91**, 052019 (2015).

[89] P. Adamson *et al.* [MINOS Collaboration], Phys. Rev. Lett. **107**, 011802 (2011).

[90] J. Kopp, P. A. N. Machado, M. Maltoni and T. Schwetz, JHEP **1305**, 050 (2013).

[91] M. Maltoni and T. Schwetz, Phys. Rev. D **76**, 093005 (2007).

[92] C. Giunti, M. Laveder, Y. F. Li and H. W. Long, Phys. Rev. D **88**, 073008 (2013).

[93] K. N. Abazajian *et al.*, arXiv:1204.5379 [hep-ph].

[94] P. A. R. Ade *et al.* [Planck Collaboration], Astron. Astrophys. **571**, A16 (2014).

[95] M. Sorel, J. M. Conrad and M. H. Shaevitz, Phys. Rev.D **70**, 073004 (2004).

[96] J. M. Conrad, C. M. Ignarra, G. Karagiorgi, M. H. Shaevitz, and J. Spitz, arXiv:1207.4765 [hep-ex] (2012).

[97] B. J. P. Jones, J. Phys. Conf. Ser. **408**, 012028 (2013), [arXiv:1110.1678 [physics.ins-det]].

[98] M. Danilov [DANSS Collaboration], PoS EPS **-HEP2013**, 493 (2013), [arXiv:1311.2777 [physics.ins-det]].

[99] J. Ashenfelter *et al.* [PROSPECT Collaboration], arXiv:1309.7647 [physics.ins-det].

[100] D. Lhuillier, PoS EPS **-HEP2013**, 522 (2013).

[101] S. Zsoldos, arXiv:1602.00568 [physics.ins-det].

[102] A. de Gouvea *et al.* [Intensity Frontier Neutrino Working Group Collaboration], arXiv:1310.4340 [hep-ex].

[103] T. Lasserre, Phys. Dark Univ. **4**, 81 (2014).

[104] S. Choubey, JHEP **0712**, 014 (2007).

[105] H. Nunokawa, O. L. G. Peres and R. Zukanovich Funchal, Phys. Lett. B **562**, 279 (2003).

[106] V. Barger, Y. Gao and D. Marfatia, Phys. Rev. D **85**, 011302 (2012).

[107] A. Esmaili, F. Halzen and O. L. G. Peres, JCAP **1211**, 041 (2012).

[108] M. Lindner, W. Rodejohann and X. J. Xu, JHEP **1601**, 124 (2016).

[109] R. Gandhi and P. Ghoshal, Phys. Rev. D **86**, 037301 (2012).

[110] N. Y. Agafonova et al., MONOLITH: A massive magnetized iron detector for neutrino oscillation studies, LNGS-P26-2000.

[111] G. Majumder, N. K. Mondal, S. Pal, D. Samuel, and B. Satyanarayana, Nucl. Instrum. Meth. **735**, 88 (2014).

[112] Thick Cylindrical Coil Systems for Strong Magnetic Fields with Field or Gradient Homogeneities of the 6th to 20th Order, M. W. Garrett, J. App. Phys. **38**, 2563 (1967).

[113] R. Merritt, C. Purcell, and G. Stroink, Rev. Sci. Instrum. **54**, 879 (1983).

[114] http://www.infolytica.com/en/products/magnet/.

[115] www.uddehlom.co.uk.

[116] Standard Test Method for dc Magnetic Properties of Materials Using Ring and Permeameter Procedures with dc Electronic Hysteresigraphs. (**A 773/A 773M – 01**).

[117] S. McFee et.al., IEEE Trans. Magnetics **24**, 439 (1988).

[118] V. L. Highland, Nucl. Instrum. Meth. **129**, 497 (1975).

[119] G. R. Lynch and O. I. Dahl, Nucl. Instrum. Meth. B **58**, 6 (1991).

[120] J. Allison *et al.*, IEEE Trans. Nucl. Sci. **53**, 270 (2006).

[121] R. Fruhwirth, Nucl. Instrum. Meth. A **262**, 444 (1987).

[122] R. L. Gluckstern, Nucl. Instrum. Meth. **24**, 381 (1963).

[123] N. Dash, V. M. Datar and G. Majumder, Astropart. Phys. **70**, 33 (2015).

[124] A. M. Dziewonski and D. L. Anderson, Phys. Earth Planet. Inter. **25**, 297 (1981).

[125] D. Casper, nuint.ps.uci.edu/nuance/default.htm.

[126] A. Chatterjee *et al.*, JINST **9**, P07001 (2014).

[127] M. M. Devi *et al.*, JINST **8**, P11003 (2013).

[128] T.K. Gaisser and T. Stanev, Phys. Rev. D **57**, 1977, (1998).

[129] M. C. Gonzalez-Garcia and M. Maltoni, Phys. Rev. D **70**, 033010 (2004).

[130] K. B. M. Mahn *et al.* [SciBooNE and MiniBooNE Collaborations], Phys. Rev. D **85**, 032007 (2012).

[131] A. B. Sousa [MINOS and MINOS+ Collaborations], AIP Conf. Proc. **1666**, 110004 (2015), arXiv:1502.07715 [hep-ex].